

MARTHERMO METRYFORGI DANCEOFTHER MALTHERAPY

SARA MARIA SPRINKHUIZEN

MR Thermometry for guidance of thermal therapy

Sara Maria Sprinkhuizen

MR Thermometry for guidance of thermal therapy

PhD thesis, Utrecht University, the Netherlands
Copyright © S. M. Sprinkhuizen, 2010

ISBN: 978-90-393-5405-6

Design: Lieke Bogaert & Sara Sprinkhuizen
Print: Wöhrmann Print Service, the Netherlands

MR Thermometry for guidance of thermal therapy

MR Thermometrie
voor het geleiden van thermische therapie
(met een samenvatting in het Nederlands)

Proefschrift

ter verkrijging van de graad van doctor aan de Universiteit Utrecht
op gezag van de rector magnificus, prof.dr. J.C. Stoof, ingevolge het
besluit van het college voor promoties in het openbaar te verdedigen op
donderdag 4 november 2010 des middags te 12.45 uur

door

Sara Maria Sprinkhuizen

geboren op 16 augustus 1980 te Goirle

Promotor: Prof. dr. ir. M.A. Viergever

Co-promotor: Dr. ir. L.W. Bartels

The research described in this thesis was carried out at the Image Sciences Institute, University Medical Center Utrecht (Utrecht, the Netherlands), under the auspices of ImagO, the Graduate Programme Medical Imaging. The project was financially supported by the Dutch Technology Foundation STW under grant UGT-6771.

Financial support for the publication of this thesis was generously provided by Philips Healthcare, LumaSense Technologies Benelux BV and the Röntgenstichting.

CONTENTS

CHAPTER 1	Introduction and outline of this thesis	1
CHAPTER 2	MR Thermometry	9
CHAPTER 3	Quantification of Respiration-induced Field Disturbances for Accurate PRFS-based MR Thermometry in the Human Breast	25
CHAPTER 4	Temperature-induced Tissue Susceptibility Changes lead to Significant Temperature Errors in PRFS-based MR Thermometry during Thermal Interventions	35
CHAPTER 5	Temperature Dependence of the Magnetic Volume Susceptibility of Human Breast Fat Tissue: an NMR Study	61
CHAPTER 6	Absolute MR Thermometry using Time Domain Analysis of Multi Gradient-echo Magnitude Images	75
CHAPTER 7	Static Field Inhomogeneity as a Source of Errors in PRFS-based and mGE-based MR Thermometry	97
CHAPTER 8	Polyethylene glycol Labeled Liposomal Drug Delivery Systems as a Source for Dynamic Absolute MR Thermometry	117
CHAPTER 9	General discussion	131
CHAPTER 10	Summary & Samenvatting	141
	Dankwoord	147
	List of publications	153
	Curriculum vitae	158



INTRODUCTION AND OUTLINE OF THIS THESIS

Thermal therapy by heating or cooling of tissue has a broad range of clinical applications. In oncology, thermal therapy can be used as an adjunct to or as a replacement of conventional cancer treatment. Moderate heating to induce local hyperthermia ($\sim 39\text{-}45^\circ\text{C}$) can be exploited to improve tumor response to radiation and chemotherapy (1), as well as for heating-assisted drug therapy and gene therapy (2,3). Thermal ablation therapy makes use of higher temperatures and is aimed at irreversible destruction of tumor tissue (4).

The interaction of heat with the body depends on multiple factors, like perfusion and heat absorption, which are highly variable from person to person and may alter during treatment (5). This makes it difficult to predict the therapeutic outcome of thermal therapy. To ensure that the target volume is adequately treated and to preserve surrounding tissue from thermal damage, continuous monitoring of the procedure is thus essential during thermal therapy.

Over the last decade, Magnetic Resonance Imaging (MRI) has become an important modality for guidance of minimally invasive and non-invasive thermal interventions. Besides pre-treatment planning and post-treatment assessment of the clinical outcome, MRI allows for non-invasive temperature measurements for monitoring and controlling thermal interventions.

MR thermometry (MRT) has clinically been applied for monitoring the ablation of uterine fibroids, which are benign tumors. The thermal dose information, derived from the MR temperature data, was shown to correlate well to the ablated area (5). When thermal ablation therapy is translated to the field of cancer treatment, for example in the breast and in the liver, bigger challenges are faced. Accurate and precise temperature measurements are required. However, the current method of choice in MR thermometry measures temperature changes only, and does not allow for absolute temperature mapping without knowledge on the starting temperature distribution. Furthermore, temperature mapping in organs such as breast and liver is challenging. One reason is that these organs are located close to the lungs, leading to respiration-induced suscep-

CHAPTER 1

tibility effects. Furthermore, the liver is subject to tissue motion and deformation. In addition, both organs contain fat, which is particularly problematic since its thermal and magnetic properties differ from those of water.

The research described in this thesis has aimed to further investigate MR thermometry techniques as to become a reliable guidance tool for thermal therapy. Potential sources of errors were studied and new temperature mapping strategies were developed.

OUTLINE OF THIS THESIS

In **chapter 2** a general introduction to MR thermometry is given. The various physical processes allowing for temperature measurements based upon the MR signal are described. It is demonstrated that proton resonance frequency shift (PRFS)-based MRT, which employs the temperature dependence of the proton electron screening constant of water, is the method of choice. Potential sources of error in PRFS-based MRT are identified, in particular time varying magnetic field inhomogeneities and heat-induced changes of the magnetic susceptibility of tissue.

Chapter 3 describes a study in which the influence of time varying magnetic field inhomogeneities on PRFS-based MRT was explored. Respiration-induced field inhomogeneities in the breast were quantified to show that respiration can induce significant temperature errors that should be corrected for to allow accurate MR thermometry in the human breast under free breathing circumstances.

Chapter 4 and **chapter 5** are concerned with the temperature dependence of the susceptibility of tissue, in particular with that of fat tissue. It is demonstrated that the influence of susceptibility changes may lead to significant temperature errors in PRFS-based MRT and are not to be neglected. Rather, a more thorough understanding of the relation between temperature and magnetic susceptibility was found to be required. Especially the temperature dependence of the susceptibility of fat tissue was of interest, since it is reported to be in the same order of magnitude as the temperature dependence of the proton electron screening constant of water (6,7). However, no values were reported in literature on the temperature dependence of the susceptibility of human fat tissue. Therefore, a study was conducted in which this was measured for human breast fat tissue, the results of which are described in chapter 5. The outcome of this study supported the findings described in chapter 4 that the impact of heat-induced susceptibility changes during thermal therapy in fatty tissues such as the human breast may not be neglected.

There is an additional problem in tissues containing fat. The electron screening constant of protons of fat is near independent of temperature which hampers PRFS-based temperature mapping in fatty tissues (6). However, the presence of fat may be used to our benefit by using it as a temperature independent reference signal which allows for absolute rather than relative MR temperature measurements. Multiple resonances can be separately detected in spectroscopic data, which can be acquired at high temporal and spatial resolution using a multi gradient-echo (mGE) sequence (8). Various acquisition and post-processing methods have been proposed for this mGE-based MRT technique (9-13). We have aimed to further explore the possibilities of mGE-based

INTRODUCTION

MR thermometry in **chapter 6**. The main focus was on the introduction of a new post-processing technique.

The post-processing of the MR signal to obtain temperature maps is based on certain assumptions with regard to the acquired signal. **Chapter 7** is concerned with a specific situation in which the assumed properties of the acquired signal are incorrect. It is shown that static background field gradients alter the effective echo time in gradient-echo acquisitions, which induces temperature errors in PRFS-based and mGE-based MR thermometry.

In **chapter 8**, a new application of the work described in chapter 6 is explored. It is hypothesized that polyethylene glycol signals from pegylated liposomes may provide a temperature insensitive proton resonance frequency component than can serve as a reference for absolute MR temperature measurements. The feasibility of performing dynamic absolute MR thermometry in combination with pegylated liposomes is evaluated.

Finally, a general discussion of this thesis is presented in **chapter 9**.

REFERENCES

1. Hall EJ, Roizin-Towle L. Biological effects of heat. *Cancer Res* 1984;44(10 Suppl):4708s-4713s.
2. Madio DP, van Gelderen P, DesPres D, Olson AW, de Zwart JA, Fawcett TW, Holbrook NJ, Mandel M, Moonen CT. On the feasibility of MRI-guided focused ultrasound for local induction of gene expression. *J Magn Reson Imaging* 1998;8(1):101-104.
3. Yatvin MB, Weinstein JN, Dennis WH, Blumenthal R. Design of liposomes for enhanced local release of drugs by hyperthermia. *Science* 1978;202(4374):1290-1293.
4. Sapareto SA, Dewey WC. Thermal dose determination in cancer therapy. *Int J Radiat Oncol Biol Phys* 1984;10(6):787-800.
5. McDannold N, Tempany CM, Fennessy FM, So MJ, Rybicki FJ, Stewart EA, Jolesz FA, Hynynen K. Uterine leiomyomas: MR imaging-based thermometry and thermal dosimetry during focused ultrasound thermal ablation. *Radiology* 2006;240(1):263-272.
6. De Poorter J. Noninvasive MRI thermometry with the proton resonance frequency method: study of susceptibility effects. *Magn Reson Med* 1995;34(3):359-367.
7. Stollberger R, Ascher PW, Huber D, Renhart W, Radner H, Ebner F. Temperature monitoring of interstitial thermal tissue coagulation using MR phase images 2. *J Magn Reson Imaging* 1998;8(1):188-196.
8. Mansfield P. Spatial mapping of the chemical shift in NMR. *Magn Reson Med* 1984;1(3):370-386.
9. Kuroda K, Mulkern RV, Oshio K, Panych LP, Nakai T, Moriya T, Okuda S, Hynynen K, Jolesz FA. Temperature mapping using the water proton chemical shift: self-referenced method with echo-planar spectroscopic imaging. *Magn Reson Med* 2000;43(2):220-225.
10. McDannold N, Barnes AS, Rybicki FJ, Oshio K, Chen NK, Hynynen K, Mulkern RV. Temperature mapping considerations in the breast with line scan echo planar spectroscopic imaging. *Magn Reson Med* 2007;58(6):1117-1123.
11. McDannold N, Hynynen K, Oshio K, Mulkern RV. Temperature monitoring with line scan echo planar spectroscopic imaging 39. *MedPhys* 2001;28(3):346-355.
12. Mulkern RV, Panych LP, McDannold NJ, Jolesz FA, Hynynen K. Tissue temperature monitoring with multiple gradient-echo imaging sequences. *J Magn Reson Imaging* 1998;8(2):493-502.
13. Taylor BA, Hwang KP, Elliott AM, Shetty A, Hazle JD, Stafford RJ. Dynamic chemical shift imaging for image-guided thermal therapy: analysis of feasibility and potential. *Med Phys* 2008;35(2):793-803.

INTRODUCTION

2

MR THERMOMETRY

MR thermometry (MRT) techniques can be employed for guidance of thermal procedures. The specific requirements for the temperature monitoring depend on the type of thermal therapy. The optimal MR sequence results from a compromise between temperature precision, spatial resolution, and temporal resolution (1-3). For example, during hyperthermia procedures, thermal monitoring is aimed at verifying that all tumor tissue has been exposed to 43-45 °C for 60-90 minutes while checking that temperature has not exceeded 42 °C in the healthy surrounding tissue. High temperature accuracy and precision is therefore required, while the requirements for spatial and temporal resolution are less stringent; voxel volumes of 1 cm³ and acquisition times of 1 minute are acceptable (4). In contrast, during thermal ablation therapy, temperature gradients of 4 °C per millimeter have been observed (5), as well as temperature elevations of 55 °C in less than 30 seconds (6). For these reasons, temperature monitoring techniques for use during thermal ablation procedures ideally have short acquisition times and high spatial resolution, to minimize information loss due to temporal and/or spatial temperature averaging.

Assessment of tissue damage is important during thermal therapy, not only to verify that the targeted tissue is fully necrosed in case of ablation therapy, but also to ensure that tissue remains unaffected, which is important for hyperthermia applications and in the surroundings of the targeted tissue during thermal ablation procedures. For this purpose, the thermal dose concept was introduced (7). Thermal dose calculations can be used as prediction of the size of the thermal lesion (1,8,9). The thermal dose depends on the temperature elevation and on the duration of the temperature elevation. In MRT guided thermal therapy the thermal dose is derived from the MR temperature measurements over time.

Many physical quantities that influence the signals measured in magnetic resonance imaging exhibit temperature dependence. For this reason, several MR parameters show temperature dependency. Whether a parameter is suitable for MR temperature measurements depends on multiple factors. The parameters' sensitivity to temperature changes plays a role, as does the linearity of the parameter changes with temperature. Furthermore, it is of importance whether the parameter can be measured independently from other temperature-induced changes in the signal. Also, the dependence on tissue type and coagulation is of influence.

CHAPTER 2

In the development of reliable MR thermometry techniques, the thermal properties of various parameters have been studied by many research groups. An overview is given in this chapter. A specific MRT technique, based on the temperature dependence of the proton electron screening constant, is discussed in more detail, since it is currently the MRT method of choice for most clinical applications where MRT plays a role.

T₁-BASED MR THERMOMETRY

It has for long been known that the longitudinal (or: spin-lattice) relaxation time T_1 is temperature dependent (10). In the work of Bloembergen et al. (10) the mechanism behind spin-lattice relaxation is explained by perturbing fields which originate in the thermal motion of magnetic dipoles in the atomic neighborhood. The first report on T_1 -based MR thermometry appeared in 1983 (11). In this work, the temperature dependence of water and *ex vivo* blood samples is studied, and the use of this mechanism for guidance of hyperthermia applications is discussed. A simple model for the T_1 temperature dependence is presented:

$$T_1 \propto e^{-\frac{E_a(T_1)}{kT}} \quad [1]$$

where E_a is the activation energy of the relaxation process, k the Boltzmann constant and T is the absolute temperature. Generally stated, T_1 values increase with increasing temperature (11-13). However, the behaviour of T_1 as a function of temperature can turn nonlinear when tissue coagulation occurs. For example, after heating above 60 °C, a decrease of T_1 was observed in rabbit muscle (14). T_1 changes due to the onset of protein denaturation limit the useful range of temperature measurement to <50 °C, and, once the temperature exceeds 40 °C, hysteresis is a significant problem (15). It has been concluded that temperature and coagulation have opposite effects on T_1 (15-17).

The temperature dependence of T_1 differs between tissues (15). Changes in the perfusion during thermal therapy may lead to problems, since blood has a substantially higher T_1 value than tissue (18,19). A lack of correlation between T_1 -weighted signal intensity and temperature has been observed during laser ablation *in vivo* (17). Furthermore, fat inside tissues leads to problems in T_1 -based MRT because temperature dependence of T_1 of fat differs from that of water containing tissues (13,20,21). Fat suppression techniques should thus be employed. On the other hand, relaxation based MR thermometry may be beneficial for temperature measurements in fatty tissues (21,22). In fat, the T_1 is linearly dependent on temperature (20,21) and does not have the hysteresis effects with temperature (15).

The most accurate T_1 measurements, e.g. using inversion recovery techniques, are time consuming and therefore unsuitable for guidance of thermal procedures. In the development for T_1 mapping techniques that are suitable for thermal therapy, a trade-off between temporal resolution, temperature sensitivity and the temperature precision must be taken into account (13).

T₂-BASED MR THERMOMETRY

The transverse (or: spin-spin) relaxation time T_2 is also temperature dependent, and was observed to decrease with increasing temperature (23). However, it is less sensitive for temperature changes than T_1 (24). Measurements do not always show the temperature dependence of T_2 , as it may be masked by non-thermal changes in relaxation mechanisms (11). No temperature dependence of T_2 was found for porcine liver *in vitro* (13). Furthermore, hysteresis occurs, and a pronounced irreversible change was observed in the T_2 -weighted signal in rabbit muscle when temperature was cycled from 25 °C up to 70 °C (14).

MR thermometry based on T_2 is thus not ideal for accurate temperature measurements during thermal therapy. However, T_2 -weighted imaging allows for accurate visualization of thermally induced tissue changes. It was shown that T_2 -weighted images of the thermal lesion correlated best with histopathologic findings (25).

EQUILIBRIUM MAGNETIZATION

When temperature increases, the two populations of spins, one with the magnetic moments parallel to B_0 and one with alignment in the opposite direction, tend to equilibrate inducing a decrease of the equilibrium magnetization (2). This phenomenon is described by Curie's law (26):

$$\frac{\Delta M_0}{\Delta T} = -\frac{1}{T} \cdot M_{0,\text{ref}} \quad [2]$$

where ΔM_0 represents the difference between magnetization measured before heating, $M_{0,\text{ref}}$, and the magnetization measured at temperature T . ΔT is the temperature change in °C and T is the absolute temperature. The MR signal is proportional to M_0 and heated tissue will thus appear as hypointense areas. As both T_1 and M_0 are contributing to the MR signal loss when temperature increases, they are generally used together to add their temperature sensitivities.

DIFFUSION-BASED MR THERMOMETRY

Thermal Brownian motion of an ensemble of molecules is described by the diffusion coefficient D , which is intrinsically temperature dependent (27):

$$D \propto e^{-\frac{E_a(D)}{kT}} \quad [3]$$

where $E_a(D)$ is the activation energy of molecular diffusion of water, which is assumed to be independent of temperature. Diffusion measurements with MR are based on sig-

CHAPTER 2

nal attenuation observed in the presence of two mutually counteracting gradients. The signal attenuation in diffusion weighted images arises from the dispersion from signal phases proportional to the distribution of displacements, caused by the random Brownian motion of molecules in the direction of the diffusion-weighting gradients.

MR temperature mapping based on D was first done by le Bihan in 1989 (4). It has a high sensitivity to temperature, of approximately $2\%/\text{ }^{\circ}\text{C}$ *in vivo* (28). The mobility of water may be limited by barriers of cellular structures. The permeability of such barriers is temperature dependent, leading to a nonlinear temperature dependence of D . Also, the temperature dependence of D varies per tissue type and coagulation of tissue leads to large changes in the diffusion constant. The diffusion constant of lipids is much smaller than water and lipids should therefore be suppressed. Measuring D is a time consuming technique, which is very sensitive to macroscopic motion. D -weighted MR thermometry has thus not been widely used for temperature mapping *in vivo*.

For all the abovementioned parameters, the temperature changes are derived from signal intensity changes. This may be a problematic approach since the MR signal intensity is influenced by multiple temperature dependent factors. For example, for both T_1 and D -based MRT, corrections may be required for the temperature dependent equilibrium magnetization.

A temperature dependent parameter which is not expressed through changes in the intensity of the signal but rather through changes in the observed proton resonance frequency (PRF) of the MR signal is the proton electron screening constant.

MR THERMOMETRY BASED ON THE PROTON RESONANCE FREQUENCY

The proton resonance frequency (or Larmor frequency) is the frequency f at which the magnetic moments of proton spins precess when placed in a static magnetic field B_0 , where it is assumed that the magnetic field B_0 is constant in time and space and independent of the object of interest:

$$f = \gamma B_0 \quad [4]$$

with γ the gyromagnetic ratio for water protons divided by 2π . Temperature dependent shifts of the water proton resonance frequency were observed in the 1950's and 1960's (29,30). It was explained by the rupture, stretching, or a small amount of bending of the hydrogen bonds. Weakening of hydrogen bonding induces more current in the electron cloud, which results in an increased electron shielding constant of the protons. As a result, the resonance frequency of the water proton becomes lower at higher temperatures, and vice versa. Taking the electron screening effect into account, equation 4 is rewritten as follows:

$$f = \gamma(1 - \sigma(T))B_0 \quad [5]$$

where σ is the temperature dependent proton electron screening constant.

MR temperature mapping based on proton resonance frequency shifts (PRFS) was first done by Ishihara and Calderon in 1995 (31). The electron screening constant, or rather the associated proton resonance frequency, has become the temperature mapping parameter of choice for several reasons. The temperature dependence of the water proton electron screening constant scales linear with temperature (32). No hysteresis occurs when tissue is cooled after heating (14) and *ex vivo*, it has been confirmed that the temperature dependence of the PRF is insensitive to coagulation (32). An important advantage of the electron screening constant thermal coefficient, $d\sigma/dT$, is its near independence of tissue composition (32), although some variations have been observed (33). The reported values for $d\sigma/dT$ are given in Table I. The proportionality constant of the PRF with temperature seems rather low, but in general, phase changes can be measured with high precision, which was confirmed *in vitro* (34) and in *ex vivo* pig's liver (35).

TABLE I Reported values of the temperature dependence of the proton electron screening constant, $d\sigma/dT$, for various substances.

Substance	$d\sigma/dT$ ($\cdot 10^{-3}/^{\circ}\text{C}$)	Reference
H_2O	1.03	(29)
	0.986 ± 0.0219	(47)
Gel	0.891 ± 0.0116	(47)
	0.97 ± 0.003	(41)
Brain	0.920 ± 0.0434	(47)
Fat (porcine)	0.0185 ± 0.035	(47)
	0	(41)
Muscle	0.97	(41)

The temperature dependence of the electron screening constant of protons in fat is some order of magnitude smaller than that of water (Table I). For this reason, PRFS-based MRT inside fat is difficult. Furthermore, fat should be suppressed in tissues containing both water and fat. Temperature mapping using the PRF was reported to be superior compared to T_1 , T_2 , and D -based temperature measurements by several authors (2,15,36-38).

In order to be able to measure temperature, temperature-induced changes of the PRF can be extracted from the phase difference $\Delta\varphi$ between successive gradient echo MR images, acquired at temperatures T and T_{ref} , respectively:

$$\begin{aligned}\Delta\varphi &= \varphi - \varphi_{\text{ref}} \\ &= -2\pi(f(T) - f(T_{\text{ref}}))TE \\ &= \Delta\sigma\gamma TE B_0\end{aligned}\quad [6]$$

with TE the echo time and $\Delta\sigma$ being the temperature-induced changes in the proton electron screening constant ($\Delta\sigma = \sigma(T) - \sigma(T_{\text{ref}})$). Note the minus sign that indicates clockwise rotation in a right-handed Cartesian coordinate system. Besides the possibility of subtracting the image of interest from a certain reference image, referenceless PRFS-based MRT has been proposed, which employs the field pattern in the surroundings of the thermally treated region for subtraction (39). Either procedure yields a phase difference $\Delta\varphi$. Subsequently, the temperature change can be found using:

$$\Delta T = \frac{\Delta\varphi}{\alpha\gamma B_0 TE} \quad [7]$$

Here, α is a proportionality constant which relates phase changes to temperature changes. It is commonly assumed that the only temperature dependency that needs to be taken into account in α is that of the proton electron screening constant of water, σ_{water} , with $\alpha = d\sigma_{\text{water}}/dT = 0.01 \text{ ppm}/^\circ\text{C}$ (40). In literature on PRFS-based MR thermometry, this definition for α is not strictly employed and negative values for α occur. In some papers, the σ in Eq. 7 is erroneously referred to as the chemical shift, and α is thus referred to as the temperature dependence of the chemical shift. This is regardless of the fact that the chemical shift, δ , is defined as $\delta[\text{ppm}] = (\sigma_{\text{ref}} - \sigma) \cdot 10^6$, with σ_{ref} the screening constant of a reference molecule. To put it accurately: with increasing temperature, the electron screening of water increases, and the chemical shift decreases (thus $d\delta_{\text{water}}/dT = -0.01 \text{ ppm}/^\circ\text{C}$). Here, the strict derivation for α based on the electron screening constant is used. In the ideal situation, in which the assumption regarding σ_{water} as the only temperature dependent parameter holds, the temperature change is given by:

$$\Delta T_{\text{ideal}} = \frac{\Delta\sigma}{\alpha} \quad [8]$$

However, reality differs from the ideal situation. In fact, multiple factors which influence the PRF may be incorporated in the final temperature measurement. The next paragraphs will address the main two sources of errors in PRFS-based MRT: time varying field disturbances and magnetic volume susceptibility changes.

Time varying field disturbances

The main magnetic field strength B_0 is rarely constant over time. Time varying changes in the magnetic field may be caused by e.g. patient movement, respiration and field drift. Equation 5 is therefore rewritten into:

$$f = \gamma(1 - \sigma(T))(B_0 + \delta B(t)) \quad [9]$$

where $\delta B(t)$ describes the magnetic field which changes over time. In absence of any temperature changes, the phase difference $\Delta\varphi$ between successive gradient echo MR images, acquired at timepoints t and t_{ref} , is then given by:

$$\Delta\varphi = -\gamma TE \Delta B \quad [10]$$

with $\Delta B = \delta B(t) - \delta B(t_{ref})$. This phase change term can lead to time-varying errors in PRFS-based MR temperature measurements. This problem is addressed in chapter 3, where time varying magnetic fields in the human breast are quantified, to assess their influence on PRFS-based MRT.

Magnetic volume susceptibility

We go back to equation 4, where the resonance frequency of the proton was related to the applied magnetic field. It is now rewritten, using B_{nuc} to indicate the magnetic field which is experienced by the proton:

$$f = \gamma B_{nuc} \quad [11]$$

As was shown in equation 5, this local magnetic field B_{nuc} is a result of screening of the nuclei from a macroscopic magnetic field in the object by the proton electron screening constant $\sigma(T)$. We now call that macroscopic magnetic field in the object B_{mac} . In addition to the electron screening constant, the magnetic volume susceptibility χ of the objects plays a role in the screening of B_{mac} (41), leading to:

$$f = \gamma \left(1 - \sigma(T) - \frac{2}{3} \chi\right) B_{mac}(\chi) \quad [12]$$

where the factor 2/3 is introduced based on the concept of the sphere of Lorentz (42). The macroscopic magnetic field may be approximated by $B_{mac} = B_0 + \mathcal{O}(\chi B_0)$ in case of nonmagnetic or weakly magnetic materials like human tissues ($|\chi| \ll 1$), which leads to:

$$f \cong \gamma B_{mac}(\chi) - \gamma \left(\sigma(T) + \frac{2}{3} \chi\right) B_0 \quad [13]$$

This equation shows that the PRF is subject to changes in B_{mac} and local χ . The macroscopic field in itself depends on the susceptibility distribution, so the same is true for the PRF. Most implementations of the PRFS-based MR thermometry method assume only temperature dependent effects of the screening constant, and neglect the influence of the susceptibility.

CHAPTER 2

There are, however, a number of factors which could alter the susceptibility distribution of tissue in ways that might result in errors in temperature measurements. It may change due to changes in shape and size of the tissue during thermal therapy (43). Also, changes in tissue perfusion during thermal therapy may alter the susceptibility, since increased blood flow alters the concentration of deoxyhemoglobin in tissue which is significantly more paramagnetic than water (43,44). Moreover, the susceptibility of tissue may change as a function of temperature. Reported values for the temperature dependence of χ are given in Table II.

Most soft tissues have magnetic properties that are similar to those of pure water. Pure water is diamagnetic at room temperature, having a volume magnetic susceptibility of $-9.05 \cdot 10^{-6}$ (45), which increases (becomes less diamagnetic) with temperature by approximately $+2 \cdot 10^{-9}/^{\circ}\text{C}$ at $37\ ^{\circ}\text{C}$, a behaviour that is largely due to a decrease in the density of water with temperature (46). For hydrogen nuclei in fat molecules, the temperature dependence of the susceptibility was found to be larger than for such nuclei in water (41,47). As a result, changes in the resonance frequency in fat tissue are determined by changes in the susceptibility distribution (48).

TABLE II Reported values of the temperature dependence of the magnetic volume susceptibility, $d\chi/dT$, for various substances.

Substance	$d\chi/dT$ ($\cdot 10^{-8}/^{\circ}\text{C}$)	Reference
H_2O	$0.199 \pm .087$	(47)
Gel	$0.277 \pm .039$	(47) (41)
	0.26	
Brain	$0.191 \pm .169$	(47)
Fat (porcine)	$0.804 \pm .145$	(47) (41)
	0.94	
Muscle	0.16	(41)

In composite tissues, containing both water and fat, the resonance frequency of water protons is also affected by heating-induced changes of the susceptibility of fat. This effect cannot be eliminated, even when fat suppression techniques are employed.

The influence of the temperature dependence of the susceptibility of tissue on PRFS-based MRT was studied, results of which are described in chapter 4. Chapter 5 reports on a study in which the temperature dependence of the susceptibility of human breast fat was measured.

The abovementioned MR thermometry techniques are based on measuring the change of a temperature dependent parameter relative to a certain baseline situation. Without

knowledge of the baseline temperature distribution at the start of the measurement, no information on absolute temperatures can thus be given. Several techniques for absolute MR temperature measurements have been developed.

TEMPERATURE SENSITIVE CONTRAST AGENTS

Absolute temperature measurements can be performed using exogenous agents which introduce temperature-related contrast in MR images. Two approaches have been explored. Conventional paramagnetic contrast agents have been introduced in temperature sensitive liposomes (49). The contrast agent is released from the liposomes when a certain temperature has been reached and signal enhancement on T_1 -weighted MR magnitude images is observed when the absolute temperature rises above this temperature. Although it is a less motion-sensitive technique, it only allows to check whether a certain temperature has been reached, making it less useful for dynamic absolute MRT measurements over a large range of temperatures. The other approach employs paramagnetic lanthanides, which exploits the temperature dependence of the chemical shifts of nuclear spins in paramagnetic complexes (50). Drawbacks of this technique are the low temporal resolution and possible instability of the paramagnetic complexes at higher temperatures, making it unsuitable for thermal ablation therapies.

INTERNAL REFERENCE RESONANCE

The shift of the water proton resonance frequency could ideally be translated to absolute temperature if it was measured with respect to a temperature independent resonance. Temperature insensitive references that have been proposed are, for example, the fat resonance and the NAA peak in brain tissue (51,52). Spectroscopic MR techniques can differentiate water resonances from other resonances. They thus allow for measurement of an internal reference resonance. Several absolute thermometry methods utilizing magnetic resonance spectroscopy (MRS) techniques, such as single voxel spectroscopy, and magnetic resonance spectroscopic imaging (MRSI), have been explored (52-55). Single voxel MRS and particularly MR Spectroscopic Imaging (MRSI) typically have very low spatial and temporal resolution, making these techniques unsuitable for the real-time guidance of thermal therapy.

However, at the expense of a lower spectral resolution and the introduction of imaging-related artefacts like geometrical distortions, it is possible to acquire spectroscopic data at high temporal and spatial resolution by using a multi gradient-echo (mGE) sequence (56). Various mGE acquisition schemes and post-processing techniques have been introduced for absolute temperature mapping (57-61). The application of the mGE sequence for absolute temperature measurements is further developed, which is described in chapter 6 and chapter 8 of this thesis.

REFERENCES

1. Chung AH, Jolesz FA, Hynynen K. Thermal dosimetry of a focused ultrasound beam in vivo by magnetic resonance imaging. *Med Phys* 1999;26(9):2017-2026.
2. Germain D, Chevallier P, Laurent A, Saint-Jalmes H. MR monitoring of tumour thermal therapy. *MAGMA* 2001;13(1):47-59.
3. Pisani LJ, Ross AB, Diederich CJ, Nau WH, Sommer FG, Glover GH, Butts K. Effects of spatial and temporal resolution for MR image-guided thermal ablation of prostate with transurethral ultrasound. *J Magn Reson Imaging* 2005;22(1):109-118.
4. Le Bihan D, Delannoy J, Levin RL. Temperature mapping with MR imaging of molecular diffusion: application to hyperthermia. *Radiology* 1989;171(3):853-857.
5. Germain D, Chevallier P, Laurent A, Savart M, Wassef M, Saint-Jalmes H. MR monitoring of laser-induced lesions of the liver in vivo in a low-field open magnet: temperature mapping and lesion size prediction. *J Magn Reson Imaging* 2001;13(1):42-49.
6. Hindley J, Gedroyc WM, Regan L, Stewart E, Tempany C, Hynynen K, McDannold N, Inbar Y, Itzhak Y, Rabinovici J, Kim HS, Geschwind JF, Hesley G, Gostout B, Ehrenstein T, Hengst S, Sklair-Levy M, Shushan A, Jolesz F. MRI guidance of focused ultrasound therapy of uterine fibroids: early results. *AJR Am J Roentgenol* 2004;183(6):1713-1719.
7. Sapareto SA, Dewey WC. Thermal dose determination in cancer therapy. *Int J Radiat Oncol Biol Phys* 1984;10(6):787-800.
8. Damianou C, Hynynen K. The effect of various physical parameters on the size and shape of necrosed tissue volume during ultrasound surgery. *J Acoust Soc Am* 1994;95(3):1641-1649.
9. McDannold NJ, King RL, Jolesz FA, Hynynen KH. Usefulness of MR imaging-derived thermometry and dosimetry in determining the threshold for tissue damage induced by thermal surgery in rabbits. *Radiology* 2000;216(2):517-523.
10. Bloembergen N, Purcell EM, Pound RV. Relaxation Effects in Nuclear Magnetic Resonance Absorption. *Physical Review* 1948;73(7):679-712.
11. Parker DL, Smith V, Sheldon P, Crooks LE, Fussell L. Temperature distribution measurements in two-dimensional NMR imaging. *MedPhys* 1983;10(3):321-325.
12. Salomir R, Palussiere J, Vimeux FC, de Zwart JA, Quesson B, Gauchet M, Le-long P, Pergrale J, Grenier N, Moonen CT. Local hyperthermia with MR-guided focused ultrasound: spiral trajectory of the focal point optimized for temperature uniformity in the target region. *J Magn Reson Imaging* 2000;12(4):571-583.
13. Matsumoto R, Mulkerin RV, Hushek SG, Jolesz FA. Tissue temperature monitoring for thermal interventional therapy: comparison of T_1 -weighted MR sequences. *J Magn Reson Imaging* 1994;4(1):65-70.
14. Graham SJ, Bronskill MJ, Henkelman RM. Time and temperature dependence of MR parameters during thermal coagulation of ex vivo rabbit muscle. *Magn Reson Med* 1998;39(2):198-203.
15. Graham SJ, Stanisz GJ, Kekojevic A, Bronskill MJ, Henkelman RM. Analysis

- of changes in MR properties of tissues after heat treatment. *Magn Reson Med* 1999;42(6):1061-1071.
16. Carasso D, Eliav U, Navon G. Nuclear magnetic resonance parameters for monitoring coagulation of liver tissue 1. *Magn Reson Med* 2005;54(5):1082-1086.
 17. Fried MP, Morrison PR, Hushek SG, Kernahan GA, Jolesz FA. Dynamic T_1 -weighted magnetic resonance imaging of interstitial laser photocoagulation in the liver: observations on in vivo temperature sensitivity 13. *Lasers SurgMed* 1996;18(4):410-419.
 18. Mietzsch E, Koch M, Schaldach M, Werner J, Bellenberg B, Wentz KU. Non-invasive temperature imaging of muscles with magnetic resonance imaging using spin-echo sequences. *Med Biol Eng Comput* 1998;36(6):673-678.
 19. Young IR, Hand JW, Oatridge A, Prior MV, Forse GR. Further observations on the measurement of tissue T_1 to monitor temperature in vivo by MRI. *Magn Reson Med* 1994;31(3):342-345.
 20. Bohris C, Schreiber WG, Jenne J, Simiantonakis I, Rastert R, Zabel HJ, Huber P, Bader R, Brix G. Quantitative MR temperature monitoring of high-intensity focused ultrasound therapy. *Magn Reson Imaging* 1999;17(4):603-610.
 21. Hynynen K, McDannold N, Mulkern RV, Jolesz FA. Temperature monitoring in fat with MRI. *Magn Reson Med* 2000;43(6):901-904.
 22. Bohris C, Jenne JW, Rastert R, Simiantonakis I, Brix G, Spoo J, Hlavac M, Nemeth R, Huber PE, Debus J. MR monitoring of focused ultrasound surgery in a breast tissue model in vivo. *Magn Reson Imaging* 2001;19(2):167-175.
 23. Belton PS, Jackson RR, Packer KJ. Pulsed NMR studies of water in striated muscle. I. Transverse nuclear spin relaxation times and freezing effects. *Biochim Biophys Acta* 1972;286(1):16-25.
 24. Parker DL. Applications of NMR imaging in hyperthermia: an evaluation of the potential for localized tissue heating and noninvasive temperature monitoring. *IEEE Trans Biomed Eng* 1984;31(1):161-167.
 25. Anzai Y, Lufkin RB, Castro DJ, Farahani K, Jabour BA, Layfield LJ, Udkoff R, Hanafee WN. MR imaging-guided interstitial Nd:YAG laser phototherapy: dosimetry study of acute tissue damage in an in vivo model. *J Magn Reson Imaging* 1991;1(5):553-559.
 26. Gultekin DH, Gore JC. Temperature dependence of nuclear magnetization and relaxation. *J Magn Reson* 2005;172(1):133-141.
 27. Simpson JH, Carr HY. Diffusion and Nuclear Spin Relaxation in Water. *Physical Review* 1958;111(5):1201-1202.
 28. MacFall J, Prescott DM, Fullar E, Samulski TV. Temperature dependence of canine brain tissue diffusion coefficient measured in vivo with magnetic resonance echo-planar imaging. *Int J Hyperthermia* 1995;11(1):73-86.
 29. Hindman JC. Proton Resonance Shift of Water in the Gas and Liquid States. *Journal of Chemical Physics* 1966;44(12):4582-4592.
 30. Schneider WG, Bernstein HJ, Pople JA. Proton magnetic resonance chemical shift of free (gaseous) and associated (liquid) hydride molecules. *Journal of Chemical Physics* 1958;284:601-607.
 31. Ishihara Y, Calderon A, Watanabe H, Okamoto K, Suzuki Y, Kuroda K. A precise

CHAPTER 2

- and fast temperature mapping using water proton chemical shift. *Magn Reson Med* 1995;34(6):814-823.
- 32. Peters RD, Hinks RS, Henkelman RM. Ex vivo Tissue-Type Independence in Proton-Resonance Frequency Shift MR Thermometry. *Magn Reson Med* 1998;40(3):454-459.
 - 33. McDannold N. Quantitative MRI-based temperature mapping based on the proton resonant frequency shift: review of validation studies. *Int J Hyperthermia* 2005;21(6):533-546.
 - 34. de Zwart JA, van Gelderen P, Kelly DJ, Moonen CT. Fast magnetic-resonance temperature imaging. *J Magn Reson B* 1996;112(1):86-90.
 - 35. Melodelima D, Salomir R, Mougenot C, Prat F, Theillere Y, Moonen C, Cathignol D. Intraluminal ultrasound applicator compatible with magnetic resonance imaging "real-time" temperature mapping for the treatment of oesophageal tumours: an ex vivo study. *Med Phys* 2004;31(2):236-244.
 - 36. Lewa CJ, Majewska Z. Temperature relationships of proton spin-lattice relaxation time T_1 in biological tissues. *Bull Cancer* 1980;67(5):525-530.
 - 37. Steiner P, Botnar R, Dubno B, Zimmermann GG, Gazelle GS, Debatin JF. Radio-frequency-induced thermoablation: monitoring with T_1 -weighted and proton-frequency-shift MR imaging in an interventional 0.5-T environment. *Radiology* 1998;206(3):803-810.
 - 38. Wlodarczyk W, Hentschel M, Wust P, Noeske R, Hosten N, Rinneberg H, Felix R. Comparison of four magnetic resonance methods for mapping small temperature changes. *Phys Med Biol* 1999;44(2):607-624.
 - 39. Rieke V, Vigen KK, Sommer G, Daniel BL, Pauly JM, Butts K. Referenceless PRF shift thermometry. *Magn Reson Med* 2004;51(6):1223-1231.
 - 40. Hindman JC. Proton Resonance Shift of Water in the Gas and Liquid States. *Journal of Chemical Physics* 1966;44:4582-4592.
 - 41. De Poorter J. Noninvasive MRI thermometry with the proton resonance frequency method: study of susceptibility effects. *Magn Reson Med* 1995;34(3):359-367.
 - 42. Dickinson WC. The time average magnetic field at the nucleus in nuclear magnetic resonance experiments. *Phys Rev* 1951;81(5):717-731.
 - 43. Young IR, Hajnal JV, Roberts IG, Ling JX, Hill-Cottingham RJ, Oatridge A, Wilson JA. An evaluation of the effects of susceptibility changes on the water chemical shift method of temperature measurement in human peripheral muscle. *Magn Reson Med* 1996;36(3):366-374.
 - 44. Weisskoff RM, Kiihne S. MRI susceptometry: image-based measurement of absolute susceptibility of MR contrast agents and human blood. *Magn Reson Med* 1992;24(2):375-383.
 - 45. Schenck JF. The role of magnetic susceptibility in magnetic resonance imaging: MRI magnetic compatibility of the first and second kinds. *Med Phys* 1996;23(6):815-850.
 - 46. Philo JS, Fairbank WM. Temperature dependence of the diamagnetism of water. *Journal of Chemical Physics* 1980;72:4429
 - 47. Stollberger R, Ascher PW, Huber D, Renhart W, Radner H, Ebner F. Temperature monitoring of interstitial thermal tissue coagulation using MR phase images 2.

- J Magn Reson Imaging 1998;8(1):188-196.
- 48. Peters RD, Hinks RS, Henkelman RM. Heat-source orientation and geometry dependence in proton-resonance frequency shift magnetic resonance thermometry. Magn Reson Med 1999;41(5):909-918.
 - 49. McDannold N, Fosheim SL, Rasmussen H, Martin H, Vykhodtseva N, Hynynen K. Heat-activated liposomal MR contrast agent: initial in vivo results in rabbit liver and kidney. Radiology 2004;230(3):743-752.
 - 50. Hekmatyar SK, Kerkhoff RM, Pakin SK, Hopewell P, Bansal N. Noninvasive thermometry using hyperfine-shifted MR signals from paramagnetic lanthanide complexes. Int J Hyperthermia 2005;21(6):561-574.
 - 51. Kuroda K, Takei N, Mulkern RV, Oshio K, Nakai T, Okada T, Matsumura A, Yanaka K, Hynynen K, Jolesz FA. Feasibility of internally referenced brain temperature imaging with a metabolite signal. Magn Reson Med Sci 2003;2(1):17-22.
 - 52. Cady EB, D'Souza PC, Penrice J, Lorek A. The estimation of local brain temperature by in vivo ^1H magnetic resonance spectroscopy. Magn Reson Med 1995;33(6):862-867.
 - 53. Corbett RJ, Laptook AR, Tollesbol G, Kim B. Validation of a noninvasive method to measure brain temperature in vivo using ^1H NMR spectroscopy. J Neurochem 1995;64(3):1224-1230.
 - 54. Farrant RD, Lindon JC, Nicholson JK. Internal temperature calibration for ^1H NMR spectroscopy studies of blood plasma and other biofluids. NMR Biomed 1994;7(5):243-247.
 - 55. Kuroda K, Suzuki Y, Ishihara Y, Okamoto K. Temperature mapping using water proton chemical shift obtained with 3D-MRSI: feasibility in vivo. Magn Reson Med 1996;35(1):20-29.
 - 56. Mansfield P. Spatial mapping of the chemical shift in NMR. Magn Reson Med 1984;1(3):370-386.
 - 57. Kuroda K, Mulkern RV, Oshio K, Panych LP, Nakai T, Moriya T, Okuda S, Hynynen K, Jolesz FA. Temperature mapping using the water proton chemical shift: self-referenced method with echo-planar spectroscopic imaging. Magn Reson Med 2000;43(2):220-225.
 - 58. McDannold N, Barnes AS, Rybicki FJ, Oshio K, Chen NK, Hynynen K, Mulkern RV. Temperature mapping considerations in the breast with line scan echo planar spectroscopic imaging. Magn Reson Med 2007;58(6):1117-1123.
 - 59. McDannold N, Hynynen K, Oshio K, Mulkern RV. Temperature monitoring with line scan echo planar spectroscopic imaging 39. MedPhys 2001;28(3):346-355.
 - 60. Mulkern RV, Panych LP, McDannold NJ, Jolesz FA, Hynynen K. Tissue temperature monitoring with multiple gradient-echo imaging sequences. J Magn Reson Imaging 1998;8(2):493-502.
 - 61. Taylor BA, Hwang KP, Elliott AM, Shetty A, Hazle JD, Stafford RJ. Dynamic chemical shift imaging for image-guided thermal therapy: analysis of feasibility and potential. Med Phys 2008;35(2):793-803.



THE PREVIOUS CHAPTER

EXPLORED THE FIELD OF MR THERMOMETRY. VARIOUS PHYSICAL AND PHYSIOLOGICAL PROCESSES ALLOWING FOR MR TEMPERATURE MEASUREMENTS WERE DESCRIBED. IT WAS POINTED OUT THAT PRFS-BASED MRT, WHICH EMPLOYS THE TEMPERATURE DEPENDENCE OF THE PROTON ELECTRON SCREENING CONSTANT OF WATER, IS THE METHOD OF CHOICE. FURTHERMORE, IT WAS SHOWN THAT THIS TECHNIQUE IS HAMPERED BY MAGNETIC FIELD INHOMOGENEITIES.

A POTENTIAL SOURCE
OF SUCH INHOMOGENEITIES IN VIVO IS
RESPIRATION. THE NEXT CHAPTER IS THUS
CONCERNED WITH THE QUANTIFICATION
OF RESPIRATION-INDUCED FIELD
INHOMOGENEITIES, TO ASSESS ITS IMPACT
ON PRFS-BASED MRT



3

QUANTIFICATION OF RESPIRATION-INDUCED FIELD DISTURBANCES FOR ACCURATE PRFS-BASED MR THERMOMETRY IN THE HUMAN BREAST

INTRODUCTION

In recent years, the treatment of breast cancer has become less invasive: from radical mastectomy to breast-conserving surgery, to minimally invasive thermal therapies such as radiofrequency ablation, laser ablation and focused ultrasound (1-3). Accurate thermometry is a prerequisite for the safe and reliable application of minimally invasive thermal therapy in a clinical setting. Proton resonance frequency shift-based (PRFS) MR thermometry is currently considered the best method for achieving this goal since it is independent of tissue type, easy to perform, has a high temporal resolution and because the PRF shift changes linearly with temperature (4-7). Temperature dependent proton resonance frequency shifts lead to phase changes in the MR signal in gradient echo scans. These phase changes can be interpreted as temperature changes, allowing MR thermometry (4-7).

Accurate phase measurements are thus a prerequisite for reliable temperature measurements using proton resonance frequency shift (PRFS) based MR thermometry in the breast. A common method to generate temperature maps is by subtracting a gradient-echo phase image acquired during treatment from a baseline phase image which is acquired prior to the thermal therapy. The temperature change ΔT is calculated from the phase change $\Delta\varphi$ using:

$$\Delta T = \frac{\Delta\varphi}{\alpha \gamma B_0 TE} \quad [1]$$

with α the temperature dependence of the electron screening constant of water ($d\sigma_{\text{water}}/dT = 0.01 \text{ ppm}/^\circ\text{C}$), B_0 the main magnetic field and TE the echo time. Using this

CHAPTER 3

subtraction-based method, all temporal phase variations other than those imposed by the thermal treatment will affect the accuracy of the MR thermometry measurement. Furthermore, even in the immobilized breast, MR thermometry can be complicated. The PRFS method in organs close to the lungs can be affected by respiration-induced local magnetic field disturbances (8). During respiration, the lung volume and the oxygen concentration in the lungs change. This causes a change in the distribution of magnetic susceptibility that leads to magnetic field fluctuations in organs surrounding the lungs such as the breast and even the brain (8,9). The associated MR frequency and phase changes adversely affect PRFS-based MR thermometry.

In preparation of the application of MR-guided focused ultrasound for the treatment of breast tumors we thought it relevant to study the distribution of respiration-induced magnetic field fluctuations in the breast in more detail.

MATERIALS & METHODS

Subjects

Four healthy female volunteers participated in this study. Exclusion criteria were a history of breast disease, presence of non-MR compatible implants, severe obesity and claustrophobia. Written informed consent was obtained from all volunteers. The mean age of the participants was 26 years (range 25-28 years).

Data acquisition

Imaging was performed on a 3-T whole body MR system (Achieva, Philips, Best, the Netherlands). Signals were acquired using a bilateral open double breast array coil (MRI devices, Würzburg, Germany). Subjects were placed in prone position, which minimized gross motion of the breasts. No heating was applied, so the temperature in the breasts was unaffected. Prior to data acquisition, first order shimming was applied to the volume of interest. To study the respiration-induced magnetic field fluctuations (ΔB) in the breast, each subject underwent the following transverse spoiled gradient-echo field mapping examinations:

- i. a fast dynamic single slice 2D scan through the center of the breasts to study the influence of regular respiration.
- ii. two single slice breath hold 2D scans through the center of the breasts, one in maximum inspiration and one in maximum expiration state, to study the effects of maximum capacity respiration.
- iii. a 3D scan covering both the breasts to study the 3D spatial characteristics of the field fluctuation. Two dynamics were acquired in breath hold, one in regular inspiration and one in regular expiration state.

The main scan parameters are listed in Table I. The echo time (TE) was set to a multiple of 2.3 msec to yield in-phase water and fat signals and the field-of-view (FOV) covered both breasts in all sequences. For each series, magnitude and phase images were reconstructed.

QUANTIFICATION OF FIELD DISTURBANCES FOR ACCURATE PRFS-BASED MRT IN THE BREAST

TABLE I Main scan parameters.

	Respiration (regular)	Respiration (max capacity)	Respiration (regular insp - exp)
	Single slice Dynamic	Single slice Breath hold	3D Dynamic
TE / TR (msec)	2.3 / 5.9	4.6 / 8.5	2.3 / 8.4
Flip angle	10	15	15
FOV (mm ²)	450 x 316	380 x 300	420 x 333
Acquired matrix	256 x 154	192 x 154	192 x 192
Reconstructed matrix	256 x 256	256 x 256	256 x 256
Scan percentage	60%	80%	80%
Slice thickness (mm)	10	10	5
Number of averages	1	10	1
(Dynamic) scan duration	0.64 sec/dynamic; 100 dynamics	10.4 sec/dynamic; 2 dynamics	32.7 sec/dynamic; 2 dynamics

Post-processing and data analysis

Prior to image analysis, phase wraps were removed using an algorithm proposed by Jenkinson (10). The resulting phase maps were converted into field maps reflecting the position-dependent fluctuation of B using:

$$\Delta B(t) = -\varphi(t) / \gamma TE \quad [2]$$

where $\Delta B(t)$ is the field offset in Tesla as a function of time and $\varphi(t)$ represents the phase at time t . Subsequently, ΔB was expressed in parts-per-million (ppm) of B_0 . The breasts were manually segmented on the modulus images. The spatial and temporal characteristics of ΔB in each volunteer were evaluated. To determine the range of the fluctuations, a maximum and a minimum intensity projection of the field maps were made along the time axis for the regular respiration series. The minimum intensity projection was subtracted from the maximum intensity projection in order to obtain a map representing the maximum field changes over time. For the maximum capacity respiration and the 3D series, the field map from the expiration state was subtracted from the field map from the inspiration state. For display purposes, a color-map was superimposed on the subtracted images. The temperature dependence of the proton resonance frequency of protons in water is -0.01 ppm/°C. Therefore, when the temperature in the breast is

CHAPTER 3

unaffected, a field fluctuation of 0.01 ppm could be misinterpreted as a temperature change of 1 °C.

RESULTS

Figure 1a shows the spatial distribution of the range of ΔB fluctuations induced by regular respiration. The figure shows that the fluctuation is largest near the thoracic wall and is larger in the right than in the left breast.



FIGURE 1 Field disturbance (in ppm) in the breast due to a) regular respiration and b) maximum capacity respiration.

Corresponding findings were obtained in all volunteers. The maximum field fluctuation over time due to regular respiration spatially averaged over both breasts were 0.13, 0.14, 0.12 and 0.13 ppm for the four volunteers (Table II). Figure 1b shows a worst case scenario: the spatial distribution of the maximum fluctuation of ΔB during maximum capacity respiration. The maximum field fluctuation due to maximum capacity respiration spatially averaged over both breasts were 0.14, 0.11, 0.17 and 0.23 ppm for the four volunteers (Table II). The spatial distribution of the field fluctuation corresponded to those found in the regular respiration series.

TABLE II Respiration induced field disturbances averaged over an ROI covering both breasts in a single slice and the standard deviation (sd) due to regular respiration and maximum capacity respiration expressed in ppm for each volunteer.

	Volunteer I	Volunteer II	Volunteer III	Volunteer IV
Regular respiration				
ΔB	0.13	0.14	0.12	0.13
<i>sd of ΔB</i>	0.03	0.03	0.04	0.02
Maximum capacity respiration				
ΔB	0.14	0.11	0.17	0.23
<i>sd of ΔB</i>	0.10	0.07	0.12	0.16

QUANTIFICATION OF FIELD DISTURBANCES FOR ACCURATE PRFS-BASED MRT IN THE BREAST

Measurements of ΔB over time in a region of interest close to the chest wall show that ΔB fluctuates with the same periodicity as the respiratory cycle (figure 2a), as is also shown in the Fourier spectrum (figure 2b). The peak of the Fourier amplitude spectrum lies around 0.38 Hertz, which is in the frequency range of respiratory motion.

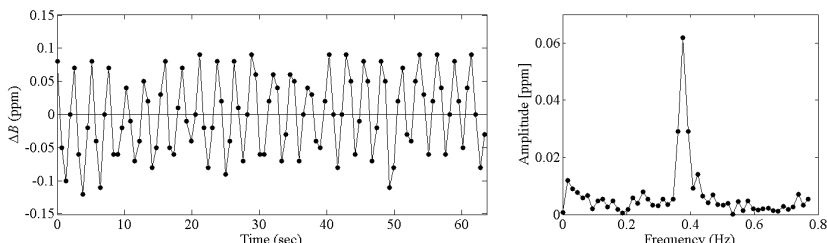


FIGURE 2 Typical example of the respiration induced field disturbances measured in a region of interest in the latero-dorsal part of the left breast over time (left) and the Fourier amplitude spectrum of $\Delta B(t)$ (right).

Coronal, sagittal and transverse images reconstructed at different levels in a 3D volume covering the breast show larger fluctuations in the right breast than in the left breast and the largest fluctuation near the thoracic wall as was seen in the single slice experiments (figure 3).

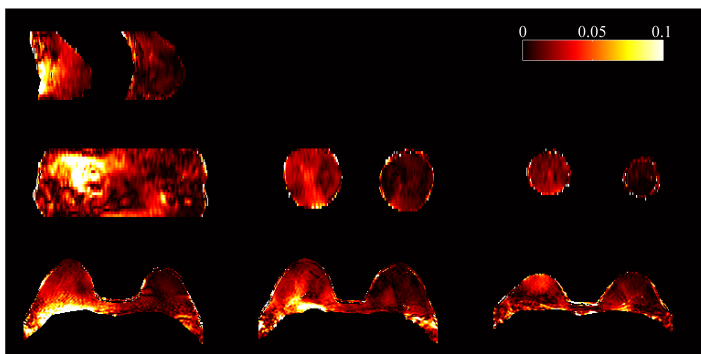


FIGURE 3 3D visualization of the distribution of the field disturbances (in ppm) in the breast. Sagittal view through the center of the right and left breast (top row); coronal view through the most dorsal part, the center and the peripheral part of the breast (center) and a transverse view through the lower part, the center and the upper part of the breast (bottom row).

DISCUSSION AND CONCLUSION

The results of our study show that the average respiration induced field fluctuations in the breast amount to approximately 0.13 ppm due to regular respiration and around 0.16 ppm due to maximum capacity respiration. Close to the chest wall, the field fluctuations were even higher, around 0.20 ppm.

In the brain, the magnitude of respiration induced field fluctuations was found to amount to about 0.01 ppm (9). Bolan et al. studied respiration induced field fluctuations in the breast and assessed the implications for MR Spectroscopy (8). They reported field fluctuations in the breast to be 10 times larger than in the brain with a magnitude of 24 Herz at 4T, which corresponds to 0.10 ppm. These numbers correspond well to our findings. The 0.13 ppm and 0.16 ppm that we report are field fluctuations averaged over both breasts. Bolan et al. demonstrated their findings in sagittal images. The results of our 3D data showed that field fluctuations are highest near the thoracic wall and are higher in the right than in the left breast. In these areas, the field fluctuations are even higher than 0.13 and 0.16 ppm, around 0.20 ppm. These field fluctuations can be misinterpreted as temperature changes of 13 °C, 16 °C and 20 °C. We hypothesize that the localization of the heart, anterior in the left part of the thoracic cavity can explain the higher field fluctuations in the right breast.

PRFS-based temperature mapping in fatty tissue, like the breast, can be challenging due to the presence of both water and fat tissue. Problems are caused by the fact that water has a temperature-dependent electron screening constant, whereas the electron screening constant of fat is near temperature independent. When PRFS-based MR thermometry is performed in fatty tissues, fat suppression is therefore required to avoid temperature errors. In this study, it was not our intention to actually perform PRFS-based thermometry, but to investigate the magnitude of field fluctuations due to respiration. To do so we acquired phase maps. Both water and fat proton signals were used to obtain optimal signal-to-noise ratio (SNR) at the shortest possible in-phase echo time. To evaluate the impact of our results on the accuracy of PRFS-based temperature mapping, we calculated the apparent temperature change in degrees Celsius for each voxel in the breast by using the temperature dependence of the proton resonance frequency of water protons ($-0.01 \text{ ppm}/^{\circ}\text{C}$). The results of our study show that to allow accurate MR thermometry in the breast during free breathing, a correction method should be applied. Proposed correction methods include adaptive subtraction techniques which automatically select the best matching baseline image per acquired phase image, either by minimizing the least square error between (a part of) the images (11) or by using navigator echoes (12). Also, referenceless PRFS-based MRT, employing the field pattern in the surroundings of the thermally treated region for subtraction, has been proposed as a solution to time varying field changes (13). Furthermore, internally-referenced temperature measurements employing the temperature independent fat resonance may reduce the influence of periodic field disturbances in the breast (14,15).

REFERENCES

1. Dowlatshahi K, Francescatti DS, Bloom KJ. Laser therapy for small breast cancers. *Am J Surg* 2002;184(4):359-363.
2. Gianfelice D, Khiat A, Amara M, Belblidia A, Boulanger Y. MR imaging-guided focused ultrasound surgery of breast cancer: correlation of dynamic contrast-enhanced MRI with histopathologic findings. *Breast Cancer Res Treat* 2003;82(2):93-101.
3. Singletary SE. Radiofrequency ablation of breast cancer. *Am Surg* 2003;69(1):37-40.
4. De Poorter J, De Wagter C, De Deene Y, Thomsen C, Stahlberg F, Achtern E. Non-invasive MRI thermometry with the proton resonance frequency (PRF) method: in vivo results in human muscle. *Magn Reson Med* 1995;33(1):74-81.
5. Denis de Senneville B, Quesson B, Moonen CT. Magnetic resonance temperature imaging. *Int J Hyperthermia* 2005;21(6):515-531.
6. Ishihara Y, Calderon A, Watanabe H, Okamoto K, Suzuki Y, Kuroda K. A precise and fast temperature mapping using water proton chemical shift. *Magn Reson Med* 1995;34(6):814-823.
7. Peters RD, Hinks RS, Henkelman RM. Ex vivo Tissue-Type Independence in Proton-Resonance Frequency Shift MR Thermometry. *Magn Reson Med* 1998;40(3):454-459.
8. Bolan PJ, Henry PG, Baker EH, Meisamy S, Garwood M. Measurement and correction of respiration-induced B_0 variations in breast 1H MRS at 4 Tesla. *Magn Reson Med* 2004;52(6):1239-1245.
9. Van de Moortele PF, Pfeuffer J, Glover GH, Ugurbil K, Hu X. Respiration-induced B_0 fluctuations and their spatial distribution in the human brain at 7 Tesla. *Magn Reson Med* 2002;47(5):888-895.
10. Jenkinson M. Fast, automated, N-dimensional phase-unwrapping algorithm. *Magn Reson Med* 2003;49(1):193-197.
11. Bakker CJ, Seppenwoolde JH, Bartels LW, van der Weide R. Adaptive subtraction as an aid in MR-guided placement of catheters and guidewires. *J Magn Reson Imaging* 2004;20(3):470-474.
12. Vigen KK, Daniel BL, Pauly JM, Butts K. Triggered, navigated, multi-baseline method for proton resonance frequency temperature mapping with respiratory motion. *Magn Reson Med* 2003;50(5):1003-1010.
13. Rieke V, Kinsey AM, Ross AB, Nau WH, Diederich CJ, Sommer G, Pauly KB. Referenceless MR thermometry for monitoring thermal ablation in the prostate. *IEEE Trans Med Imaging* 2007;26(6):813-821.
14. Kuroda K. Non-invasive MR thermography using the water proton chemical shift 1. *Int J Hyperthermia* 2005;21(6):547-560.
15. McDannold N, Hynynen K, Oshio K, Mulkern RV. Temperature monitoring with line scan echo planar spectroscopic imaging 39. *MedPhys* 2001;28(3):346-355.

← IN CHAPTER 3 IT IS SHOWN THAT RESPIRATION CAN INDUCE SIGNIFICANT TEMPERATURE ERRORS IN PRFS-BASED MRT AND SHOULD BE CORRECTED FOR TO ALLOW ACCURATE MR THERMOMETRY IN THE HUMAN BREAST DURING FREE BREATHING.

← IN CHAPTER 2, ANOTHER POTENTIAL SOURCE OF ERRORS IN MR TEMPERATURE MEASUREMENTS WAS IDENTIFIED: THE TEMPERATURE DEPENDENCE OF THE MAGNETIC SUSCEPTIBILITY OF TISSUE.

THE IMPACT OF HEATING-INDUCED SUSCEPTIBILITY CHANGES ON MRT IS COMMONLY NEGLECTED IN THE LITERATURE ON MRT. THE GOAL OF THE NEXT CHAPTER THEREFORE WAS TO INVESTIGATE THE INFLUENCE OF THE TEMPERATURE DEPENDENCE OF THE SUSCEPTIBILITY OF TISSUE ON PRFS-BASED MRT DURING THERMAL THERAPY →

4

TEMPERATURE-INDUCED TISSUE SUSCEPTIBILITY CHANGES LEAD TO SIGNIFICANT TEMPERATURE ERRORS IN PRFS-BASED MR THERMOMETRY DURING THERMAL INTERVENTIONS

INTRODUCTION

Next to excellent soft-tissue contrast, MRI also offers methods to acquire temperature maps, which allow for monitoring and guiding of thermal interventions. Proton resonance frequency shift (PRFS)-based MR thermometry (MRT) is the most commonly used temperature monitoring technique. It is based on the temperature dependence of the proton resonance frequency (PRF) of protons in water molecules and is thus applicable in water-containing tissues. The technique does not work for protons in fat molecules and for this reason adequate fat suppression is essential for accurate thermometry in tissues containing both water and fat.

PRFS-based MRT is hampered by time varying magnetic field changes. In the application of this technique, the contribution of field changes, which originate from temperature-induced magnetic volume susceptibility changes, is commonly ignored. This disregards the fact that the magnetic volume susceptibility χ (which will hereinafter be referred to as ‘susceptibility’) of water and water-containing tissue is temperature dependent (1,2). Several studies have suggested that this may lead to PRFS-based temperature errors in water and water-containing tissues (1-4). This has been shown for water (3) and brain tissue (2), which both have a temperature dependent susceptibility in the order of $d\chi/dT = 0.002 \text{ ppm}/^\circ\text{C}$.

CHAPTER 4

In tissues containing both water and fat, more considerable susceptibility-related problems may occur. For fat tissue, the temperature dependence of the susceptibility has been reported to be $d\chi_{\text{fat}}/dT = 0.0094 \text{ ppm}/^{\circ}\text{C}$ (1) and $d\chi_{\text{fat}}/dT = 0.00804 \text{ ppm}/^{\circ}\text{C}$ (2). Changes in the susceptibility distribution lead to magnetic field changes, which occur not only locally at the site of the susceptibility change, but also arise non-locally in the surroundings of the susceptibility change. Consequently, in tissues containing both water and fat, e.g. the human breast, the PRF in the water-containing glandular tissue is also affected by temperature-induced susceptibility changes in the surrounding fat tissue. This may hamper PRFS-based temperature measurements in composite tissues. To date, no attention has been paid to the quantification of this effect, in spite of the fact that it may be significant and that its influence on PRFS-based MRT is not eliminated by fat-suppression techniques.

In this study, we aimed to quantify the influence of the temperature dependence of the susceptibility of water and fat on PRFS-based MR temperature maps, both experimentally and theoretically. First, controlled water-fat phantom heating experiments were conducted to demonstrate the occurrence of temperature-induced susceptibility-related temperature errors in actual PRFS-based MR temperature maps. To study the implications for a clinical case, simulations were performed to predict the errors in PRFS-based measurements during a thermal therapy procedure in human tissue. For this we used a model of the female breast, since thermal ablation of breast tumors is an emerging minimally invasive therapeutic intervention. Breast tumors originate in glandular tissue, and are mostly surrounded by fat. Susceptibility-related temperature errors are therefore expected to occur when PRFS-based MRT is used to monitor a thermal procedure in the breast. Temperature errors in the glandular tissue were quantified by computation of the magnetic field changes, resulting from temperature-induced susceptibility changes in a thermally heated region. Since the magnitude of the temperature errors is determined by the susceptibility distribution, which is related to the shape of the anatomy of interest as well as the shape of the heating pattern, various orientations and sizes of the heated region were analyzed, to study the impact on the temperature errors.

THEORY

The susceptibility distribution inside and outside an arbitrarily shaped object depends on the temperature distribution $T(\mathbf{r})$. From a certain susceptibility distribution $\chi(\mathbf{r}, T(\mathbf{r}))$ that is placed in a uniform external magnetic field B_0 , the macroscopic magnetic field B_{mac} can be derived from Maxwell's equations in matter. The PRF at a certain location inside an object is proportional to the magnetic field experienced by the hydrogen nuclei at that location, B_{nuc} . This local magnetic field B_{nuc} is a result of screening of the nuclei from the macroscopic magnetic field in the object, B_{mac} , by microscopic current distributions, described by the proton electron screening constant $\sigma(\mathbf{r}, T(\mathbf{r}))$ and the susceptibility of the object $\chi(\mathbf{r}, T(\mathbf{r}))$, which are both temperature dependent (1):

$$B_{\text{nuc}}(\mathbf{r}, T(\mathbf{r})) = \left(1 - \sigma(\mathbf{r}, T(\mathbf{r})) - \frac{2}{3} \chi(\mathbf{r}, T(\mathbf{r}))\right) B_{\text{mac}}(\chi(\mathbf{r}, T(\mathbf{r})) \quad [1]$$

The macroscopic magnetic field may be approximated by $B_{\text{mac}} = B_0 + \mathcal{O}(\chi B_0)$ in case of nonmagnetic or weakly magnetic materials like human tissues ($|\chi| \ll 1$), which leads to:

$$B_{\text{nuc}}(\mathbf{r}, T(\mathbf{r})) \approx B_{\text{mac}}(\chi(\mathbf{r}, T(\mathbf{r}))) - \left(\sigma(\mathbf{r}, T(\mathbf{r})) + \frac{2}{3} \chi(\mathbf{r}, T(\mathbf{r})) \right) B_0 \quad [2]$$

In PRFS-based MR thermometry, temperature-induced field changes in B_{nuc} are extracted from the phase difference $\Delta\varphi$ between successive gradient echo MR images, acquired at temperatures T and T_{ref} , respectively:

$$\begin{aligned} \Delta\varphi &= \varphi - \varphi_{\text{ref}} \\ &= -\gamma TE(B_{\text{nuc}}(\mathbf{r}, T(\mathbf{r})) - B_{\text{nuc}}(\mathbf{r}, T_{\text{ref}}(\mathbf{r}))) \\ &= -\gamma TE \left(\Delta B_{\text{mac}} - \left(\Delta\sigma + \frac{2}{3} \Delta\chi \right) B_0 \right) \end{aligned} \quad [3]$$

with γ the gyromagnetic ratio, TE the echo time, $\Delta B_{\text{mac}} = B_{\text{mac}}(\chi(\mathbf{r}, T(\mathbf{r}))) - B_{\text{mac}}(\chi_{\text{ref}}(\mathbf{r}, T_{\text{ref}}(\mathbf{r})))$ and $\Delta\sigma$ and $\Delta\chi$ being the temperature-induced changes in the proton electron screening constant and susceptibility, respectively. Note the minus sign that indicates clockwise rotation in a right-handed Cartesian coordinate system. The temperature change, which is measured with PRFS-based MRT, ΔT_{PRFS} , is computed from the phase difference, using:

$$\Delta T_{\text{PRFS}} = \frac{\Delta\varphi}{\alpha \gamma B_0 TE} \quad [4]$$

Here it is commonly assumed that the only temperature dependency that needs to be taken into account in the proportionality constant α is that of the proton electron screening constant of water, σ_{water} , with $\alpha = d\sigma_{\text{water}}/dT = 0.01 \text{ ppm}/^\circ\text{C}$ (5). In literature on PRFS-based MR thermometry, this definition for α is not strictly employed and negative values for α occur. In some papers, the σ in Eq. 1 is erroneously referred to as the chemical shift, and α is thus referred to as the temperature dependence of the chemical shift. This is regardless of the fact that the chemical shift, δ , is defined as $\delta[\text{ppm}] = (\sigma_{\text{ref}} - \sigma) \cdot 10^6$, with σ_{ref} the screening constant of a reference molecule. To put it accurately: with increasing temperature, the electron screening of water increases, and the chemical shift decreases (thus $d\delta_{\text{water}}/dT = -0.01 \text{ ppm}/^\circ\text{C}$). Here, the strict derivation for α based on the electron screening constant is used. In the ideal situation, in which the assumption regarding σ_{water} as the only temperature dependent parameter holds, the temperature change is given by:

$$\Delta T_{\text{ideal}} = \frac{\Delta\sigma}{\alpha} \quad [5]$$

CHAPTER 4

However, as shown in Eq. 3, reality differs from the ideal situation in the sense that the temperature dependence of the susceptibility distribution also plays a role. When the actually measured phase change (Eq. 3) is substituted in Eq. 4, this yields:

$$\Delta T_{\text{PRFS}} = -\frac{1}{\alpha} \left(\frac{\Delta B_{\text{mac}}}{B_0} - \Delta \sigma - \frac{2}{3} \Delta \chi \right) \quad [6]$$

The difference between the measured temperature change ΔT_{PRFS} and the ideal temperature change ΔT_{ideal} gives the temperature error ε_T :

$$\varepsilon_T = -\frac{1}{\alpha} \left(\frac{\Delta B_{\text{mac}}}{B_0 \Delta T} - \frac{2}{3} \frac{\Delta \chi}{\Delta T} \right) \quad [7]$$

Eq. 7 shows that the temperature error ε_T is subject to changes in B_{mac} and χ . The macroscopic field in itself also depends on changes in the susceptibility distribution, which means that temperature errors are induced by local (χ) and non-local (B_{mac}) susceptibility changes.

The contributions of temperature-induced susceptibility changes to the PRF are usually ignored in PRFS-based MRT. This is a problematic approach, for two reasons. First, by neglecting the local susceptibility changes of the water-containing tissue, temperature errors occur (3), even though the temperature dependence of the susceptibility of water is small: $d\chi_{\text{water}}/dT = 0.00199 \text{ ppm}/^{\circ}\text{C}$ (2). Second, changes in $\chi(\mathbf{r}, T(\mathbf{r}))$ alter the macroscopic field B_{mac} , which affects the PRF, and hence the measured temperature, of all water protons that experience this field change. Temperature measurements in water-containing tissue may therefore be corrupted by non-local field effects due to susceptibility changes in the surroundings of the tissue. This raises a realistic problem in tissues where fat is present, e.g. breast tissue, because the temperature dependence of the susceptibility of fat, χ_{fat} , is reported to be in the same order of magnitude as the temperature dependence of the proton electron screening constant of water ($d\chi_{\text{fat}}/dT = 0.0094 \text{ ppm}/^{\circ}\text{C}$ (1) and $d\chi_{\text{fat}}/dT = 0.00804 \text{ ppm}/^{\circ}\text{C}$ (2)). Consequently, temperature-induced susceptibility changes of fat in the surroundings of a tumor may affect the magnetic field experienced by the water protons within the tumor.

METHODS

Heating experiments

To demonstrate the impact of temperature-induced susceptibility changes on actual PRFS-based MR temperature maps, controlled phantom heating experiments were conducted. The phantom consisted of a large circular container ($\varnothing = 28 \text{ cm}$, height = 8 cm), filled with deionized water, in which a Perspex cylinder (outer radius = 22 mm; inner radius = 20 mm; length = 77 mm) was placed, such that the long axis of the cylinder was aligned perpendicular to the main magnetic field. This cylinder contained the

fluid of interest, of which the temperature, and, hence, susceptibility was altered during the experiment. Two different fluids were examined: in the first experiment, the cylinder was filled with the same deionized water as was used in the outer container. In the second experiment, the cylinder was filled with sunflower oil. Sunflower oil was chosen because it conveniently allowed for fast exchange between scans, as will be described below. At the start of both experiments, the temperature of the water in the outer container was equal to the temperature of the fluid within the cylinder ($\approx 21^\circ\text{C}$). For both set-ups, 70 dynamic coronal single slice PRFS-based MRT scans were acquired through the center of the cylinder. The first 10 PRFS-based MRT scans were acquired with the whole phantom at constant temperature. The fluid inside the fixed cylinder was quickly replaced in between scans 10 and 11 with identical, but heated, fluid (accomplished by placing the fluid in a warm water bath with a constant temperature of 75°C for 1 hour prior to scanning) using a large syringe.

The magnitude of the temperature errors is determined by the susceptibility and temperature distribution. The phantom set-up was designed such that the temperature errors in the PRFS-based temperature maps were expected to appear as a dipole field pattern surrounding the cylinder. This is shown by the following equation, which gives the microscopic field change (ΔB_{nuc}) caused by susceptibility changes, outside an infinite cylinder (perpendicular to B_0), in a plane perpendicular to the long axis:

$$\Delta B_{\text{nuc}} = \frac{\Delta\chi_e}{3} B_0 + \frac{\Delta\chi_e - \Delta\chi_i}{2} R^2 \frac{(x^2 - z^2)}{(x^2 + z^2)^2} B_0 \quad [8]$$

with R the radius of the cylinder and $\Delta\chi_e$ and $\Delta\chi_i$ the susceptibility changes outside and inside the cylinder, respectively. This equation shows that, for a coronal PRFS-based temperature map and $\Delta\chi_e = 0$, a positive $\Delta\chi_i$ leads to positive field offsets in the direction of z (B_0), and to negative field offsets over the x -axis. This corresponds to a temperature underestimation over the z -axis and a temperature overestimation over the x -axis. To validate the true temperature during all scans at these two locations, two optical temperature fibers were positioned at ~ 1.5 mm from the edge of the cylinder. The PRFS-based temperature was averaged within a region of interest (2x2 voxels) at these two locations for all scans. The temporal behaviour of the PRFS-based temperature changes in the water surrounding the cylinder was then compared to the temperature as measured with the optical fibers. A third optical fiber was placed inside the cylinder to monitor the temperature of the heated fluid over the whole duration of the experiment.

All scans were performed on a 1.5-T whole body MRI scanner (Achieva, Philips Healthcare, Best, The Netherlands), and the following scan parameters were used for a single slice spoiled gradient echo scan: FOV 300x300 mm²; acquired voxel size: 1.875x1.875x4 mm³; flip angle $\alpha = 30^\circ$; number of signal averages = 1; read-out gradient $G_R = 11$ mT/m; $TE = 15$ msec and $TR = 50$ msec. Dynamic scan time = 8 seconds. Total scan time (70 dynamics) = 9 minutes and 21 seconds.

Simulation technique

In PRFS-based MRT, the susceptibility-related field changes are erroneously interpreted as a temperature-change. Discrimination between susceptibility-related field changes and other (e.g. proton electron screening related) effects is not feasible during a thermal procedure *in vivo*. Therefore, simulations were performed to calculate the susceptibility related field changes. To quantify the influence of susceptibility changes on PRFS-based MRT, the corresponding, χ -related, magnetic field changes in B_{nuc} need to be determined:

$$\Delta B_{\text{nuc}}(\chi) = \left(\frac{\Delta B_{\text{mac}}}{B_0 \Delta T} - \frac{2}{3} \frac{\Delta \chi}{\Delta T} \right) \quad [9]$$

It has been indicated by several authors that the use of the Fourier transform to calculate magnetic field changes from a given susceptibility distribution is advantageous (6,7). It is possible to derive a relation between the magnetizing field H and the susceptibility distribution χ using the Fourier-based approach (6). However, since the B field is a direct observable related to the Larmor frequency, whereas the H -field is not a direct observable, we have chosen to use the relation between the susceptibility distribution $\chi(\mathbf{r}, T(\mathbf{r}))$ and the observable B field itself. The derivation is shown in Appendix I.

The input for each simulation consisted of two susceptibility distributions, $\chi(\mathbf{r}, T_{\text{ref}}(\mathbf{r}))$ and $\chi(\mathbf{r}, T_{\text{incr}}(\mathbf{r}))$, where $T_{\text{ref}}(\mathbf{r})$ is the pre-heating, starting temperature distribution and $T_{\text{incr}}(\mathbf{r})$ is the post-heating, increased temperature distribution. Using the Fourier-based technique, the microscopic field B_{nuc} was then computed for both the pre-heating and post-heating susceptibility distribution. The corresponding field change ΔB_{nuc} was found by subtraction of the pre-heating from the post-heating outcome, and expressed in ppm using:

$$\Delta B_{\text{nuc}}[\text{ppm}] = \frac{\Delta B_{\text{nuc}}[\text{Tesla}]}{B_0[\text{Tesla}]} \cdot 10^6$$

Subsequently, the temperature error was computed, using Eq. 7. The negative proportionality of $\Delta B_{\text{nuc}}(\chi)$ and ε_T is apparent: negative $\Delta B_{\text{nuc}}(\chi)$ values lead to a temperature overestimation, and positive $\Delta B_{\text{nuc}}(\chi)$ values lead to a temperature underestimation. We aim to quantify the errors in temperature measurements that are related to susceptibility changes and it is therefore that in our simulations, ΔB_{nuc} exclusively incorporates temperature-related susceptibility effects, and no proton electron screening effects.

For numerical accuracy, the computational volume was taken at least a factor of two larger than the object of interest for all simulations. The matrix size was 256x256x256 for all computations.

Simulation of phantom experiments

The results from the phantom heating experiment were compared to the outcome of the Fourier-based simulation technique. The expected temperature errors around the cylinder were calculated based on a 3D model of the cylindrical phantom, in which the following susceptibility values were used for the fluid inside the cylinder:

$$\chi_{\text{water}}(T) = -9.05 \cdot 10^{-6} + 0.002 \cdot 10^{-6} \cdot \Delta T \quad [10]$$

$$\chi_{\text{oil}}(T) = -8.53 \cdot 10^{-6} + 0.0055 \cdot 10^{-6} \cdot \Delta T \quad [11]$$

based on χ_{water} as reported in (8), $d\chi_{\text{water}}/dT$ from (9), and with ΔT the temperature change of the fluid. The volume susceptibility of sunflower oil was calculated based on the density (0.919 g/cm³ (10)) and the molar susceptibility and molar mass of the constituent fatty acids (10,11) [mole% fatty acid (molar susceptibility (10⁻³ cm³/mol), molar mass (g/mol)): 7% palmitic (-2.50, 256.42); 63% linoleic (-2.51, 280.45); 25% oleic (-2.62, 282.46); 5% stearic (-2.77, 284.48)]. The temperature dependence of the susceptibility of the oil was computed using a volume thermal expansion coefficient of 0.654·10³ (12): $d\chi_{\text{oil}}/dT = 0.0055 \text{ ppm}/^{\circ}\text{C}$. The susceptibility of Perspex is reported to be: $\chi_{\text{Perspex}} = -9 \cdot 10^{-6}$ (13). The temperature dependence of χ_{Perspex} was computed from the linear thermal expansion coefficient (0.7 mm/m/10 °C) and the density of the Perspex (1.2 g/cm³), yielding: $d\chi_{\text{Perspex}}/dT = -0.0019 \text{ ppm}/^{\circ}\text{C}$, which is the same as water. For this reason, the Perspex layer was not separately modeled, but instead was assigned the same susceptibility properties as the surrounding water.

The temperature error around the cylinder was computed for a range of temperatures of the fluid inside the cylinder. The optically measured temperature of the fluid during the experiment was used to correlate the PRFS-based temperature to the simulated temperature error. The susceptibility of the water surrounding the cylinder was kept constant in the simulations.

Susceptibility-related temperature error quantification in the female breast

To study the implications of the temperature dependence of the susceptibility on MR thermometry measurements in a realistic setting, simulations were performed. MR-guided High Intensity Focused Ultrasound (MRgHIFU) in the breast was chosen as a model for the quantification of susceptibility-induced MR temperature errors. MRgHIFU ablation is a therapeutic modality of which the potential for the non-invasive treatment of benign and malignant breast tumors has been shown (14-22). A 3D breast model was employed, based on an anatomical data set of a breast tumor patient. A high resolution $T_1\text{w}$ 3D breast MRI scan of a 63-year-old female breast cancer (invasive ductal carcinoma) patient was used, to obtain spatial distributions of water and fat in a realistic geometry. Written informed consent was obtained from the patient. The tumor (0.7x0.7x0.7 cm³) was located at 4.8 cm from the mamilla in the upper outer quadrant of the left breast. The glandular tissue and tumor tissue of the left breast were semi-automatically segmented using a region growing procedure. Smoothing was applied using a Gaussian kernel ($\sigma = 1$, kernel size = 7). Outside the segmented glandular and tumor tissues, it was assumed that only fat was present.

To simulate the effect of a thermal intervention using HIFU, a thermal spot was placed in the breast model at the location of the tumor. A typical shape of the thermal focus of a focused ultrasound transducer is an ellipsoid. Multiple thermal spot sizes were modeled. The thermal spot diameter was varied from 1 mm to 8 mm, in steps of 1 mm. The length/diameter ratio was kept 2.5 for all simulated thermal spots. The largest

CHAPTER 4

thermal spot had a diameter of 8 mm and a length of 20 mm. During thermal ablation procedures in the breast, a maximum temperature increase of $\Delta T = 49.9 \text{ }^{\circ}\text{C}$ has been reported (20). For our simulations, we used a more conservative value of $\Delta T = 30 \text{ }^{\circ}\text{C}$. In all ellipsoidal thermal spots, a stationary Gaussian temperature distribution was modeled (sigma = 4, kernel size = $1/2 \cdot$ thermal spot diameter) with a maximum temperature of $67 \text{ }^{\circ}\text{C}$ ($T_{\text{ref}} = 37 \text{ }^{\circ}\text{C}$, $\Delta T = 30 \text{ }^{\circ}\text{C}$).

Not only the size of the thermal spot, but also the position of the HIFU transducer with regard to the patient affects the shape of the heating pattern, and thus the distribution of ΔB_{nuc} , within the patient. In most reports on MR-guided HIFU of the breast, the transducer was sonicating parallel to the anteroposterior axis. In one report, the transducer was sonicating parallel to the coronal plane (19). Therefore, all simulations were performed at three different orthogonal orientations of the thermal spot with respect to the main magnetic field.

The following volume susceptibility values were retrieved from the literature, and used for the simulations in the breast model:

$$\chi_{\text{glandular}}(T) = -9.05 \cdot 10^{-6} + 0.002 \cdot 10^{-6} \cdot \Delta T \quad [12]$$

$$\chi_{\text{fat}}(T) = -7.79 \cdot 10^{-6} + 0.0094 \cdot 10^{-6} \cdot \Delta T \quad [13]$$

using χ_{fat} as reported in (11) and $d\chi_{\text{fat}}/dT$ from (1). The susceptibility of the tumor tissue was taken to be equal to that of the glandular tissue. For both the pre-heating breast model (without a thermal spot) and all thermal therapy models, the 3D susceptibility distribution was calculated per voxel, using a weighted average of the local glandular tissue/fat tissue-fraction (Wiedemann's law) and the local temperature. Subsequently, the ΔB_{nuc} field was calculated and converted to a 3D temperature error map. The temperature errors at the location of the tumor are of particular interest, since they will affect the thermal dose calculations at the tumor site. To quantify the range of temperature errors within the tumor, the following steps were taken: first, the tumor was manually segmented. Then, all voxels from the 3D temperature error map that were located within this tumor region were visualized in a histogram (one per thermal spot orientation) for all thermal spot sizes.

RESULTS

Heating experiments

Figure 1 and figure 2 display the results of the heating experiments of water and oil, respectively. To visually emphasize the non-local influence of changes in χ , the temperature values inside the cylinder were not shown. In figure 1, the results of the experiment with temperature changes in water are displayed. The PRFS-based temperature map of scan number 12 is shown (bottom left). This is the second scan after administration of the heated water, since scan 11 suffered from minor flow-artifacts in the outer container due to the movement of the MR table after administration of the heated fluid. In this temperature map, a dipole-field pattern can be appreciated around the cylinder: the PRFS-based temperature is decreased over the z-axis of the cylinder, and increased over the x-axis. At the top left and bottom right, the PRFS-based temperature profiles over time at two locations around the cylinder are plotted (dashed lines) together with the optical fiber data (bold lines). Note that the starting temperature (as measured with the optical fibers) was added to the PRFS temperature profiles (which measure only temperature changes). The dipole-behaviour is clearly apparent: after administration of the heated water, the measured PRFS-based temperature change at location 1 decreased ($\Delta T = -2.9 \text{ }^{\circ}\text{C}$), whereas at location 2, it increased ($\Delta T = +2.3 \text{ }^{\circ}\text{C}$). The true temperature, measured with the optical fiber, showed only a slight temperature increase at both locations, of $+0.4 \text{ }^{\circ}\text{C}$ maximum.

For the heating experiment in sunflower oil, shown in figure 2, this behaviour was also observed. The PRFS-based temperature map of scan number 12 (bottom left) shows a more pronounced dipole field pattern around the cylinder, as was expected based on the stronger temperature dependence of χ_{fat} compared to χ_{water} . The PRFS-based temperature profiles over time (dashed lines) were compared with the true optical measured temperature (bold lines) at two locations (top left and bottom right). At location 1, the measured PRFS-based temperature decreased between scan 10 and 11 ($\Delta T = -4.3 \text{ }^{\circ}\text{C}$), whereas at location 2, the PRFS-based temperature increased ($\Delta T = +5.6 \text{ }^{\circ}\text{C}$). Again, the true temperature only moderately increased at both locations ($+0.7 \text{ }^{\circ}\text{C}$ maximum).

CHAPTER 4

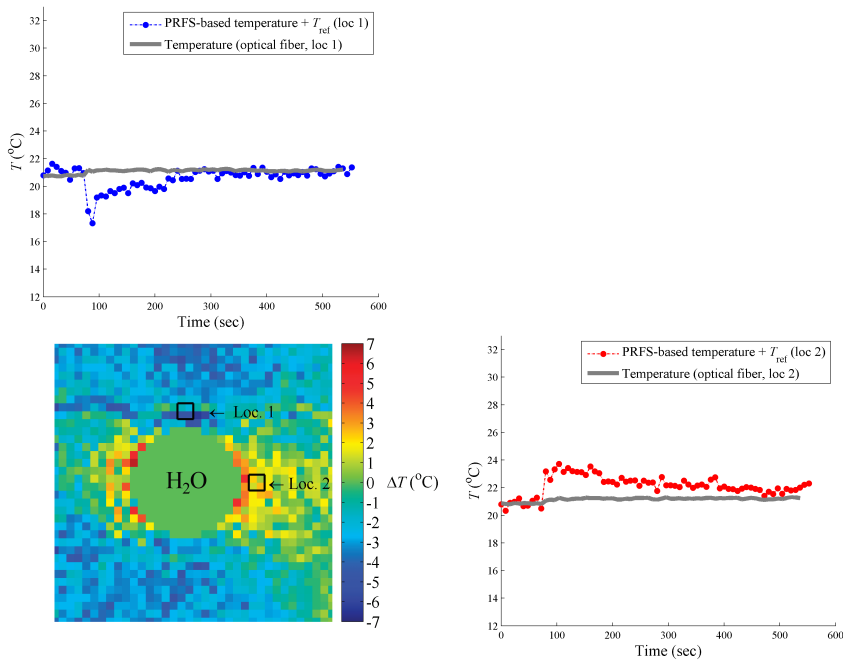


FIGURE 1 The PRFS-based temperature map of scan number 12 of the water heating experiment is (partially) shown at the bottom left. In the temperature map, the two regions from which the average temperature over time was taken are indicated by black boxes. At these two locations, optical fiber temperature measurements were acquired. Per location, the optical temperature is compared to the PRFS-based temperature in the graphs above and to the right of the temperature map.

TEMPERATURE-INDUCED SUSCEPTIBILITY CHANGES LEAD TO ERRORS IN PRFS-BASED MRT

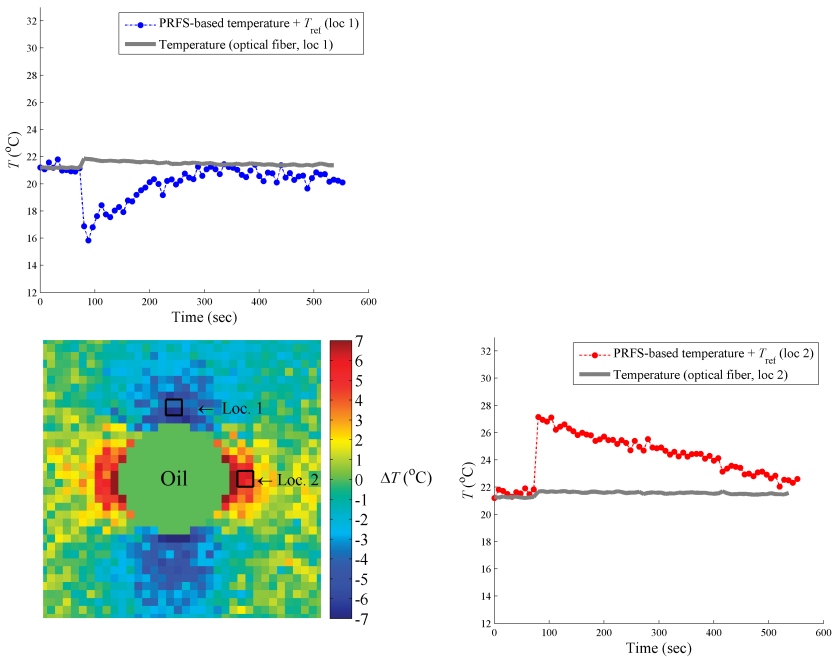


FIGURE 2 The PRFS-based temperature map of scan number 12 of the oil heating experiment is (partially) shown at the bottom left. In the temperature map, the two regions from which the average temperature over time was taken are indicated by black boxes. At these two locations, optical fiber temperature measurements were acquired. Per location, the optical temperature is compared to the PRFS-based temperature in the graphs above and to the right of the temperature map.

Simulation of phantom experiments

In figure 3, the outcome of the simulations is compared to the results for the water (left) and oil (right) heating experiment. The top row shows the PRFS-based MR temperature maps of scan number 12. The middle row shows the two corresponding simulated temperature error maps. The simulations are based on the susceptibility changes within the cylinder, which were calculated using Eq. 10, Eq. 11 and the true temperature of the fluid inside the cylinder, which was measured with the optical fiber ($\Delta T = 40.9^\circ\text{C}$ for the water experiment, and $\Delta T = 47.5^\circ\text{C}$ for the oil experiment).

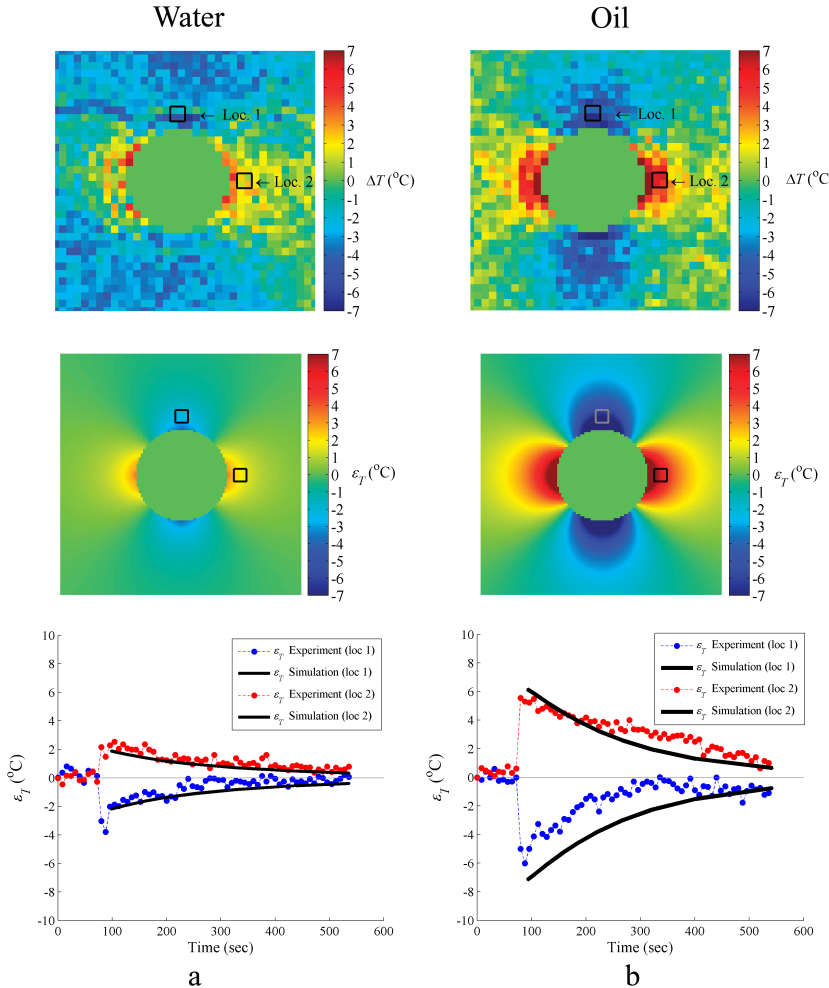


FIGURE 3 Experimentally measured temperature change (top row) and simulated temperature error (middle row) are shown for the heating experiment with water (a) and oil (b). The bottom row shows the experimental and simulated temperature error over time. The experimental temperature error is determined by subtracting the optical temperature from the PRFS-based temperature which was averaged within a region (black boxes). The simulated temperature error is computed by averaging the simulated values in a region at the same two locations as were used experimentally (black/gray boxes).

The bottom row compares the experimental temperature error with the simulated error over time. The experimental temperature error was calculated by subtraction of the PRFS-based temperature from the optical fiber temperature, per location. The simulated temperature error was found by averaging the calculated ε_T values within a region of interest that corresponds to the region that was used in the experimental analysis (depicted as the black/gray boxes in the simulated error map). The simulated results correlate well with the experimental findings for water. In case of the heated oil experiment, the simulated temperature error is overall larger at location 1, and slightly smaller at location 2. Generally, the temporal behaviour of the measured temperature error corresponds to the simulated error.

Susceptibility-related temperature error quantification in the female breast

Figure 4a shows a single slice of the anatomical T_1w 3D breast MRI scan, in which fat tissue is bright and glandular tissue is dark. Figure 4b shows sections of three orthogonal slices taken from the 3D breast model that was computed from the anatomical dataset. In these segmented images, the glandular tissue is depicted bright, and fat tissue is shown in black. The tumor tissue was manually segmented in 3D for the quantification of ε_T within the tumor, and is visualized in this figure by a red overlay.

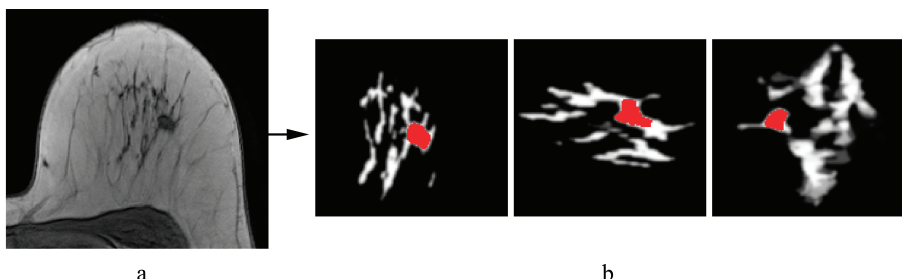


FIGURE 4a shows a single slice of the anatomical T_1w 3D breast MRI scan, in which fat tissue (bright) and glandular tissue (dark) is discernible. From the anatomical dataset, a 3D breast model is computed, containing the distribution of glandular and fat tissue in 3D. **FIGURE 4b** shows (parts of) three orthogonal slices through this breast model, the glandular tissue is depicted bright and fat tissue is shown in black. The tumor tissue is segmented for quantification purposes and shown in red.

The top rows of figures 5, 6 and 7 show the temperature distribution (color-scaled) as induced by a thermal spot with a diameter of 8 mm (length = 20 mm), with relation to the glandular tissue (in white), for all three orientations of the thermal spot (z-axis, x-axis and y-axis, respectively). Per figure, sections of three orthogonal slices through the breast model are displayed. The bottom rows of figures 5, 6 and 7 show the corresponding temperature error maps. These maps show the distribution of ε_T in and around the tumor. The figures show that the ε_T pattern is related to the orientation of the thermal spot. The maximum temperature error found in glandular tissue in the whole breast model ranged between: -8.6 °C and +2.6 °C (thermal spot along z-axis); -4.9 °C and +6.0 °C (thermal spot along x-axis); -4.0 °C and +6.2 °C (thermal spot along y-axis).

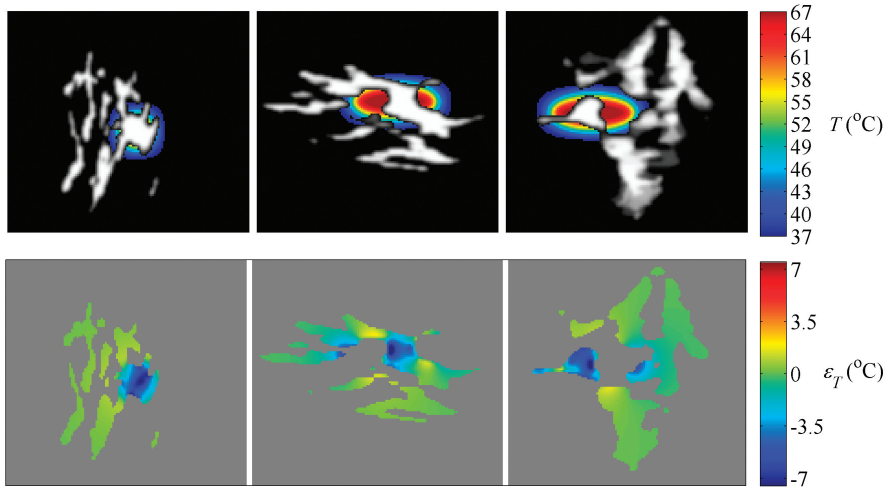


FIGURE 5 This figure shows three orthogonal (sections of) slices through the temperature distribution as induced by a thermal spot which is oriented along the z-axis (diameter = 8 mm; length = 20 mm) with relation to the glandular tissue (top row). The corresponding temperature error ε_T maps are also given (bottom row). The maximum temperature errors found in the glandular tissue ranged between -8.6 °C and +2.6 °C.

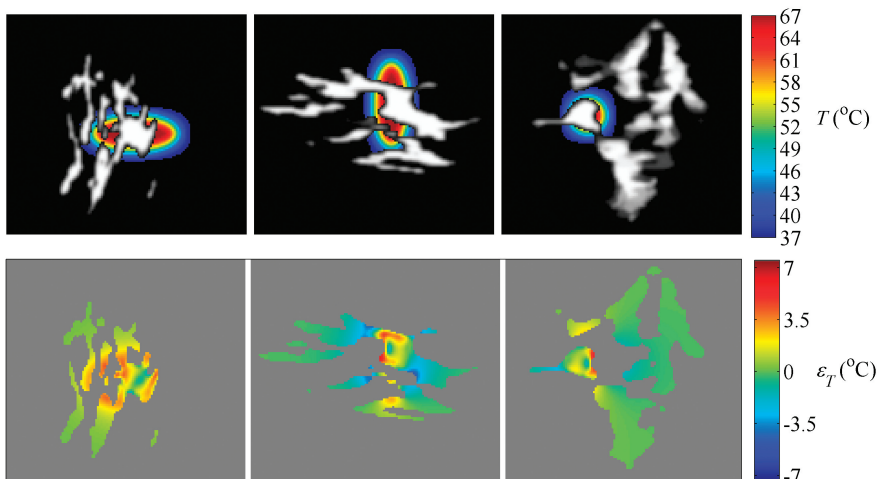


FIGURE 6 This figure shows three orthogonal (sections of) slices through the temperature distribution as induced by a thermal spot which is oriented along the x-axis (diameter = 8 mm; length = 20 mm) with relation to the glandular tissue (top row). The corresponding temperature error ε_T maps are also given (bottom row). The maximum temperature errors found in the glandular tissue ranged between -4.9 °C and +6.0 °C.

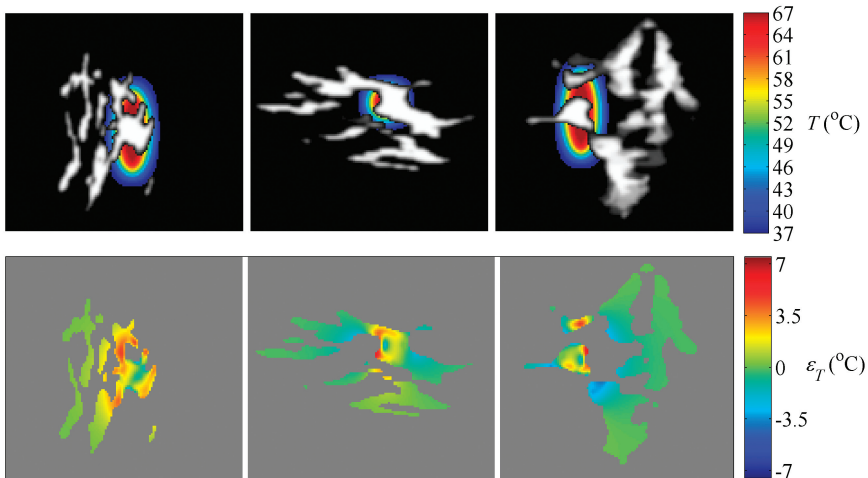


FIGURE 7 This figure shows three orthogonal (sections of) slices through the temperature distribution as induced by a thermal spot which is oriented along the y-axis (diameter = 8 mm; length = 20 mm) with relation to the glandular tissue (top row). The corresponding temperature error ε_T maps are also given (bottom row). The maximum temperature errors found in the glandular tissue ranged between $-4.0\text{ }^{\circ}\text{C}$ and $+6.2\text{ }^{\circ}\text{C}$.

Figure 8 shows the histograms of the ε_T distribution within the tumor, for all sizes of the thermal spot (indicated by the thermal spot diameter). From the histograms, an evident relation between the orientation of the thermal spot and the temperature error ε_T inside the tumor can be observed. The orientation of thermal spot in the z direction led to a temperature underestimation of about $4 - 6\text{ }^{\circ}\text{C}$, whereas the orientation of the thermal spot in the x or y direction led to an overestimation of $2 - 3\text{ }^{\circ}\text{C}$. Furthermore, all three histograms show that the spread in temperature errors increased with the size of the thermal spot, i.e. susceptibility-related temperature errors increased when more fat was heated.

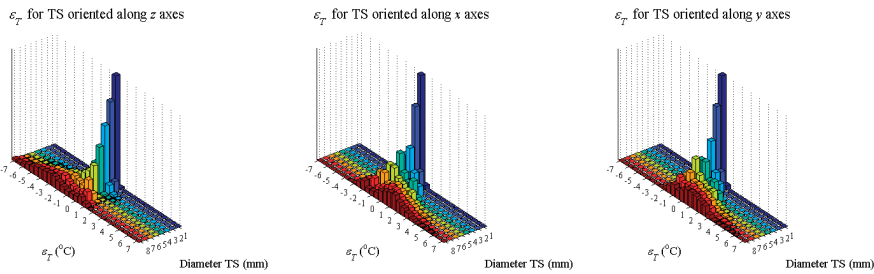


FIGURE 8 Three histograms of the temperature error ε_T within the tumor, each corresponding to an orientation of the thermal spot. Per histogram, ε_T is given for all sizes of the thermal spot applied (expressed in diameter). The histograms clearly show an increase of temperature error in the tumor with increasing thermal spot size. Also, a remarkable correlation with the thermal spot orientation and ε_T is shown. For a thermal spot oriented along the z-axis (left histogram), an underestimation of the temperature is seen, whereas a thermal spot which is oriented along the x- or y-axis (middle and right histograms) leads to a temperature overestimation.

DISCUSSION AND CONCLUSIONS

We have shown both experimentally and theoretically that temperature-induced susceptibility changes can lead to changes in the magnetic field, which can introduce significant temperature errors in PRFS-based MR thermometry. The experimental results provided proof for the fact that susceptibility changes affect the PRFS-based MRT method non-locally. This was shown in a phantom set-up where water and oil were locally heated. The PRFS-based temperature around the heated region showed large deviations when compared to optical fiber measurements. The PRFS-based measured temperature changes around the cylinder containing the heated fluid ranged between $-2.9\text{ }^{\circ}\text{C}$ and $+2.3\text{ }^{\circ}\text{C}$ for water, and between $-4.3\text{ }^{\circ}\text{C}$ and $+5.6\text{ }^{\circ}\text{C}$ for oil, where the optical temperature showed only a slight temperature increase of $+0.7\text{ }^{\circ}\text{C}$ maximum. The employed simulation technique supported the experimental findings.

Simulations were performed to quantify the susceptibility-related temperature errors in a breast tumor during thermal ablation using HIFU. Breast tumors are situated in the glandular tissue, and are surrounded by fat. During HIFU ablation in the breast, a margin of at least 10 mm around the tumor is necessary to ensure thermal coagulation of the whole lesion (17), which inevitably leads to heating of fat in the surroundings of the tumor. Real-time thermometry can be used to automatically steer the HIFU energy deposition during MRgHIFU therapy using a closed feedback control loop and a volumetric heating strategy (23). To warrant the safety of this approach, the acquisition of reliable MR temperature maps is a prerequisite (15,17). The thermal dose, which can be computed from the temperature evolution over time (24), is also an important characteristic for the guidance of thermal therapy, since it is a non-invasive measure for tissue necrosis, and can thus determine the thermal treatment effectiveness and duration. Over a certain period, for temperatures above $43\text{ }^{\circ}\text{C}$, a temperature increase of $1\text{ }^{\circ}\text{C}$ doubles the thermal dose. As a consequence, temperature errors of that order may

have a major impact on the treatment guidance. Our simulations showed that for the chosen anatomy, an ellipsoidal HIFU thermal spot of diameter 8 mm and length 20 mm and a maximum temperature increase of $\Delta T = 30\text{ }^{\circ}\text{C}$ led to temperature errors in the glandular tissue ranging between $-8.6\text{ }^{\circ}\text{C}$ and $+6.2\text{ }^{\circ}\text{C}$, depending orientation of the focal spot. The errors within the tumor were of particular interest and ranged between $-6\text{ }^{\circ}\text{C}$ and $+3\text{ }^{\circ}\text{C}$. Errors of this order of magnitude may significantly influence the accuracy of thermal dose calculations during thermal therapy.

The largest diameter of the tumor in this study was about 0.7 cm in all three dimensions. For larger tumors, under certain heating conditions, there may be less susceptibility-related temperature errors in the center of the tumor than for smaller tumors. However, total coagulation is important also at the tumor boundaries, where susceptibility-related errors will occur if the tumor is adjacent to heated fat tissue, regardless of the tumor size.

The shape and size of the heated area were shown to be of influence. An ellipsoidal thermal spot that was aligned with the z-axis led to temperature underestimations within the tumor, whereas when it was aligned with the x- or y-axis, it mainly led to a temperature overestimation at that location. This is due to the fact that changing the orientation and shape of the heating pattern (covering a heterogeneous mixture of aqueous and fatty tissue) influences the susceptibility distribution and thereby the temperature errors in the local temperature inside and outside the thermal spot measured with PRFS-based MRT. The most frequently used breast HIFU systems currently employ a transducer that sonicates parallel to the y-axis, so that temperatures at the tumor location are overestimated. Nevertheless, transducers that sonicate parallel to the coronal (the x-z) plane are also utilized. In that case, the temperature error is very much dependent on the angle of sonication within that plane.

We investigated temperature-induced changes in the susceptibility. However, temperature is not the only mechanism leading to a change in tissue susceptibility. For example, the susceptibility may change due to alterations in the balance of oxygenated and de-oxygenated hemoglobin and myoglobin (2,4). Also, changes in tissue shape and size (e.g. caused by edema) are of possible influence. The incorporation of susceptibility related effects in the computation of PRFS-based temperature maps is not straightforward, due to the unconfined characteristic of the phenomenon.

The influence of susceptibility on PRFS-based MRT is currently mostly ignored. We have shown that temperature errors do occur. This may induce erroneous thermal dose calculations which may have an important influence on the outcome of the thermal treatment. This effect is not eliminated when fat suppression techniques are employed. Susceptibility-related temperature errors are not only related to the shape and orientation of the heating pattern but also depend on the distribution of water and fat inside the heated area. The compensation of susceptibility-related temperature errors is therefore not straightforward and requires in-depth analysis of each specific case.

APPENDIX

The following section describes the Fourier-based simulation technique as is used in this article. The magnetic field distribution, which arises from a known susceptibility distribution $\chi(\mathbf{r})$ placed in a homogeneous external magnetic field, is computed, starting with the general equation:

$$\nabla \times \mathbf{B} = \mu_0 (\mathbf{J}_{\text{free}} + \nabla \times \mathbf{M}) \quad [\text{A1}]$$

in which \mathbf{M} is the magnetization vector of the tissue. Inside the bore of the MRI scanner, there are no primary current sources, and hence $\mathbf{J}_{\text{free}} = 0$ inside the bore. As a result, we have:

$$\nabla \times \mathbf{B} = \mu_0 \nabla \times \mathbf{M} \quad [\text{A2}]$$

Furthermore, the rotation of \mathbf{M} may be replaced by an equivalent current density distribution $\mathbf{J}_{\text{equiv}}$:

$$\nabla \times \mathbf{M} = \mathbf{J}_{\text{equiv}} \quad [\text{A3}]$$

Therefore, in order to calculate \mathbf{B} , the equivalent current density field $\mathbf{J}_{\text{equiv}}$ is required. By definition, we have

$$\mathbf{M} = \chi \mathbf{H} \quad [\text{A4}]$$

Combining Eq. A4 with the general vector equality $\nabla \times (p\mathbf{Q}) = -\mathbf{Q} \times (\nabla p) + p(\nabla \times \mathbf{Q})$ for any scalar p and vector \mathbf{Q} , yields:

$$\nabla \times \mathbf{M} = \nabla \times (\chi \mathbf{H}) = -\mathbf{H} \times (\nabla \chi) + \chi(\nabla \times \mathbf{H}) \quad [\text{A5}]$$

Since $\nabla \times \mathbf{H} = \mathbf{J}_{\text{free}} = 0$ inside the bore, this reduces to

$$\nabla \times \mathbf{M} = \nabla \times (\chi \mathbf{H}) = -\mathbf{H} \times (\nabla \chi) \quad [\text{A6}]$$

and hence, using Eq. A3 we have

$$\mathbf{J}_{\text{equiv}} = -\mathbf{H} \times (\nabla \chi) \quad [\text{A7}]$$

In MRI, it is customary to work with the magnetic field \mathbf{B} rather than the auxiliary vector \mathbf{H} . Since by definition $\mathbf{H} = 1/\mu_0 \mathbf{B}$, Eq. 8 becomes:

$$\mathbf{J}_{\text{equiv}} = -\frac{1}{\mu} \mathbf{B} \times (\nabla \chi) \quad [\text{A8}]$$

in which the recursive nature becomes apparent: the presence of a non-zero $\mathbf{J}_{\text{equiv}}$ at one point in space affects the \mathbf{B} field (and hence $\mathbf{J}_{\text{equiv}}$) at another point in space. In the application at hand however, the values of χ are small (for biological tissues, χ values are typically of the order of magnitude of 10^{-6}), and hence replacing $1/\mu \mathbf{B}$ by $1/\mu_0 \mathbf{B}$ in Eq. A8 results in only a small relative error of order $\mathcal{O}(\chi)$ in the calculation of $\mathbf{J}_{\text{equiv}}$:

$$\mathbf{J}_{\text{equiv}} = -\frac{1}{\mu_0} \mathbf{B}_0 \times (\nabla \chi) (1 + \mathcal{O}(\chi)) \quad [\text{A9}]$$

At this point, we neglect the error of order $\mathcal{O}(\chi)$, and calculate $\mathbf{J}_{\text{equiv}}$ directly from the known \mathbf{B}_0 and the given susceptibility distribution χ using:

$$\mathbf{J}_{\text{equiv}} = -\frac{1}{\mu_0} \mathbf{B}_0 \times (\nabla \chi) \quad [\text{A10}]$$

Using these equivalent currents as a substitute for materials with magnetic susceptibility, the \mathbf{B} -field is now completely determined by only free currents and equivalent currents in a vacuum ($\mu = \mu_0$ everywhere):

$$\nabla \times \mathbf{B} = \mu_0 (\mathbf{J}_{\text{free}} + \mathbf{J}_{\text{equiv}}) \quad [\text{A11}]$$

For any superposition of current density distributions, the resulting \mathbf{B} -field is the sum of the \mathbf{B} -fields from each separate current density distribution. In the case of Eq. A11, $\mathbf{J}_{\text{free}} = 0$ inside the bore; we are only interested in the \mathbf{B} -field arising from $\mathbf{J}_{\text{equiv}}$. Let the \mathbf{B} -field arising from $\mathbf{J}_{\text{equiv}}$ be denoted as $\delta\mathbf{B}$. Once the $\mathbf{J}_{\text{equiv}}$ distribution has been calculated using Eq. A10, the $\delta\mathbf{B}$ field can be calculated using a vector potential, as is explained below. In analogy to the general equation $\nabla^2 \mathbf{A} = -\mu_0 \mathbf{J}$, we define $\mathbf{A}_{\text{equiv}}$ as the vector potential that arises from the $\mathbf{J}_{\text{equiv}}$ distribution:

$$\nabla^2 \mathbf{A}_{\text{equiv}} = -\mu_0 \mathbf{J}_{\text{equiv}} \quad [\text{A12}]$$

In order to calculate the $\mathbf{A}_{\text{equiv}}$ from Eq. A12, we use a Fourier technique, as will be explained in more detail further below. First, however, in order to indicate how the $\delta\mathbf{B}$ field follows from the $\mathbf{A}_{\text{equiv}}$ field once the $\mathbf{A}_{\text{equiv}}$ field is calculated, we combine the general vector equality $\nabla^2 \mathbf{Q} = -\nabla(\nabla \cdot \mathbf{Q}) - \nabla \times (\nabla \times \mathbf{Q})$ (for any vector \mathbf{Q}) with $\nabla \cdot \mathbf{A}_{\text{equiv}} = 0$ (because the magnetic field is stationary) to obtain:

$$\nabla^2 \mathbf{A}_{\text{equiv}} = -\nabla \times (\nabla \times \mathbf{A}_{\text{equiv}}) \quad [\text{A13}]$$

CHAPTER 4

In combination with Eq. A12 and $\nabla \times \delta\mathbf{B} = \mu_0 \mathbf{J}_{\text{equiv}}$ (Eq. A11) this leads to

$$\delta\mathbf{B} = \nabla \times \mathbf{A}_{\text{equiv}} \quad [\text{A14}]$$

We now focus on calculating $\mathbf{A}_{\text{equiv}}$ from the $\mathbf{J}_{\text{equiv}}$ distribution. Solving Eq. A12 yields:

$$\mathbf{A}_{\text{equiv}}(\mathbf{r}) = \frac{\mu_0}{4\pi} \int d^3\xi \frac{\mathbf{J}_{\text{equiv}}(\xi)}{|\mathbf{r} - \xi|} \quad [\text{A15}]$$

In Eq. A15, the advantages of performing the calculations in the Fourier-domain are apparent because of the convolution operator inside the equation. The equation can be written symbolically as

$$\begin{aligned} A_x &= \frac{\mu_0}{4\pi} J_x * G \\ A_y &= \frac{\mu_0}{4\pi} J_y * G \\ A_z &= \frac{\mu_0}{4\pi} J_z * G \end{aligned} \quad [\text{A16}]$$

In which

$$\mathbf{J}_{\text{equiv}} = (J_x, J_y, J_z) \quad [\text{A17}]$$

$$\mathbf{A}_{\text{equiv}} = (A_x, A_y, A_z) \quad [\text{A18}]$$

$$G(\mathbf{r} - \xi) = \frac{1}{|\mathbf{r} - \xi|} \quad [\text{A19}]$$

Let the following lowercase symbols $\mathbf{a}_{\text{equiv}}(\mathbf{k})$, $\delta\mathbf{b}(\mathbf{k})$, $\mathbf{j}_{\text{equiv}}(\mathbf{k})$, $\theta(\mathbf{k})$ denote the Fourier transforms of $\mathbf{A}_{\text{equiv}}(\mathbf{r})$, $\delta\mathbf{B}(\mathbf{r})$, $\mathbf{J}_{\text{equiv}}(\mathbf{r})$, and $\chi(\mathbf{r})$, respectively. Using the integral:

$$\frac{1}{|\mathbf{r} - \xi|} = \frac{1}{\pi} \int d^3k \frac{e^{-i2\pi\mathbf{k}\cdot(\mathbf{r}-\xi)}}{k^2} \quad [\text{A20}]$$

We have

$$g(\mathbf{k}) = \frac{1}{\pi k^2} \quad [\text{A21}]$$

Furthermore, since the Fourier transform of $\nabla\chi(\mathbf{r})$ equals $-i2\pi\mathbf{k}\theta(\mathbf{k})$, and since $\mathbf{J}_{\text{equiv}}(\mathbf{r}) = -(1/\mu_0) \mathbf{B}_0 \times \nabla\chi(\mathbf{r})$, and \mathbf{B}_0 is a constant vector field pointing along the z-axis ($\mathbf{B}_0 = B_0 \mathbf{z}$), we have

$$\mathbf{j}_{\text{equiv}}(\mathbf{k}) = \frac{2\pi B_0}{\mu_0} \begin{pmatrix} ik_y \theta(\mathbf{k}) \\ -ik_x \theta(\mathbf{k}) \\ 0 \end{pmatrix} \quad [\text{A22}]$$

and

$$\mathbf{a}_{\text{equiv}}(\mathbf{k}) = \frac{1}{2\pi} B_0 \begin{pmatrix} ik_y \theta(\mathbf{k}) / k^2 \\ -ik_x \theta(\mathbf{k}) / k^2 \\ 0 \end{pmatrix} \quad [\text{A23}]$$

Furthermore, the Fourier transform of $\delta\mathbf{B} = \nabla \times \mathbf{A}_{\text{equiv}}$ (see above) yields $\delta\mathbf{b} = -2\pi i \mathbf{k} \times \mathbf{a}_{\text{equiv}}$. Therefore, we now have:

$$\delta\mathbf{b}(\mathbf{k}) = B_0 \begin{pmatrix} k_x k_z \theta(\mathbf{k}) / k^2 \\ k_y k_x \theta(\mathbf{k}) / k^2 \\ -(k_x^2 + k_y^2) \theta(\mathbf{k}) / k^2 \end{pmatrix} \quad [\text{A24}]$$

As a result, the desired $\delta\mathbf{B}(\mathbf{r})$ field can now be found by calculating the inverse Fourier transform of $\delta\mathbf{b}(\mathbf{k})$, which on its turn is calculated from the given $\theta(\mathbf{k})$ using Eq. A24:

$$\chi(\mathbf{r}) \xrightarrow{F} \theta(\mathbf{k}) \xrightarrow{\text{Eq.A24}} \delta\mathbf{b}(\mathbf{k}) \xrightarrow{F^{-1}} \delta\mathbf{B}(\mathbf{r}) \quad [\text{A25}]$$

Note that this calculated $\delta\mathbf{B}(\mathbf{r})$ field is the deviation from the \mathbf{B}_0 field and is given in Tesla. The component of $\delta\mathbf{B}(\mathbf{r})$ along the z-direction is taken. The macroscopic magnetic field is then given by: $B_{\text{mac}} = B_0 + \delta B$. The last step is the computation of the total microscopic field B_{nuc} . For our purpose, the changes in the B_{nuc} field that are related to temperature-induced susceptibility changes in the object are of importance. Therefore, in this case, the electron screening constant term can be excluded from Eq. 1:

$$B_{\text{nuc}}(\mathbf{r}, T(\mathbf{r})) = \left(1 - \frac{2}{3} \chi(\mathbf{r}, T(\mathbf{r}))\right) B_{\text{mac}}(\chi(\mathbf{r}, T(\mathbf{r}))) \quad [\text{A26}]$$

REFERENCES

1. De Poorter J. Noninvasive MRI thermometry with the proton resonance frequency method: study of susceptibility effects. *Magn Reson Med* 1995;34(3):359-367.
2. Stollberger R, Ascher PW, Huber D, Renhart W, Radner H, Ebner F. Temperature monitoring of interstitial thermal tissue coagulation using MR phase images 2. *J Magn Reson Imaging* 1998;8(1):188-196.
3. Peters RD, Hinks RS, Henkelman RM. Heat-source orientation and geometry dependence in proton-resonance frequency shift magnetic resonance thermometry. *Magn Reson Med* 1999;41(5):909-918.
4. Young IR, Hajnal JV, Roberts IG, Ling JX, Hill-Cottingham RJ, Oatridge A, Wilson JA. An evaluation of the effects of susceptibility changes on the water chemical shift method of temperature measurement in human peripheral muscle. *Magn Reson Med* 1996;36(3):366-374.
5. Hindman JC. Proton Resonance Shift of Water in the Gas and Liquid States. *Journal of Chemical Physics* 1966;44:4582-4592.
6. Salomir R, Denis de Senneville B, Moonen CT. A fast calculation method for magnetic field inhomogeneity due to an arbitrary distribution of bulk susceptibility. *Concepts in Magnetic Resonance Part B: Magnetic Resonance Engineering* 2003;19B(1):26 - 34.
7. Marques JP, Bowtell R. Application of a Fourier-Based Method for Rapid Calculation of Field Inhomogeneity Due to Spatial Variation of Magnetic Susceptibility. *Concepts in Magnetic Resonance Part B* 2005;25B(1):65–78.
8. Schenck JF. The role of magnetic susceptibility in magnetic resonance imaging: MRI magnetic compatibility of the first and second kinds. *Med Phys* 1996;23(6):815-850.
9. Philo JS, Fairbank WM. Temperature dependence of the diamagnetism of water. *Journal of Chemical Physics* 1980;72:4429
10. Lide DR, editor. CRC Handbook of Chemistry and Physics, 90th Edition (Internet Version 2010). 90th ed: CRC Press/Taylor and Francis, Boca Raton, FL
11. Hopkins JA, Wehrli FW. Magnetic susceptibility measurement of insoluble solids by NMR: magnetic susceptibility of bone. *Magn Reson Med* 1997;37(4):494-500.
12. Coupland JN, McClements JD. Physical properties of liquid edible oils Journal of the American Oil Chemists' Society 1997;74(12):1559-1564.
13. Moerland MA, Beersma R, Bhagwandien R, Wijrdeman HK, Bakker CJ. Analysis and correction of geometric distortions in 1.5 T magnetic resonance images for use in radiotherapy treatment planning. *Phys Med Biol* 1995;40(10):1651-1654.
14. Furusawa H, Namba K, Nakahara H, Tanaka C, Yasuda Y, Hirabara E, Imahariyama M, Komaki K. The evolving non-surgical ablation of breast cancer: MR guided focused ultrasound (MRgFUS). *Breast Cancer* 2007;14(1):55-58.
15. Furusawa H, Namba K, Thomsen S, Akiyama F, Bendet A, Tanaka C, Yasuda Y, Nakahara H. Magnetic resonance-guided focused ultrasound surgery of breast cancer: reliability and effectiveness. *J Am Coll Surg* 2006;203(1):54-63.
16. Gianfelice D, Khiat A, Amara M, Belblidia A, Boulanger Y. MR imaging-guided

- focused ultrasound surgery of breast cancer: correlation of dynamic contrast-enhanced MRI with histopathologic findings. *Breast Cancer Res Treat* 2003;82(2):93-101.
- 17. Gianfelice D, Khiat A, Amara M, Belblidia A, Boulanger Y. MR imaging-guided focused US ablation of breast cancer: histopathologic assessment of effectiveness - initial experience. *Radiology* 2003;227(3):849-855.
 - 18. Gianfelice D, Khiat A, Boulanger Y, Amara M, Belblidia A. Feasibility of magnetic resonance imaging-guided focused ultrasound surgery as an adjunct to tamoxifen therapy in high-risk surgical patients with breast carcinoma. *J Vasc Interv Radiol* 2003;14(10):1275-1282.
 - 19. Huber PE, Jenne JW, Rastert R, Simiantonakis I, Sinn HP, Strittmatter HJ, von Fournier D, Wannenmacher MF, Debus J. A new noninvasive approach in breast cancer therapy using magnetic resonance imaging-guided focused ultrasound surgery. *Cancer Res* 2001;61(23):8441-8447.
 - 20. Hyynnen K, Pomeroy O, Smith DN, Huber PE, McDannold NJ, Kettenbach J, Baum J, Singer S, Jolesz FA. MR imaging-guided focused ultrasound surgery of fibroadenomas in the breast: a feasibility study. *Radiology* 2001;219(1):176-185.
 - 21. Khiat A, Gianfelice D, Amara M, Boulanger Y. Influence of post-treatment delay on the evaluation of the response to focused ultrasound surgery of breast cancer by dynamic contrast enhanced MRI. *Br J Radiol* 2006;79(940):308-314.
 - 22. Zippel DB, Papa MZ. The use of MR imaging guided focused ultrasound in breast cancer patients; a preliminary phase one study and review. *Breast Cancer* 2005;12(1):32-38.
 - 23. Mougenot C, Quesson B, de Senneville BD, de Oliveira PL, Sprinkhuizen S, Palussiere J, Grenier N, Moonen CT. Three-dimensional spatial and temporal temperature control with MR thermometry-guided focused ultrasound (MRgHIFU). *Magn Reson Med* 2009;61(3):603-614.
 - 24. Sapareto SA, Dewey WC. Thermal dose determination in cancer therapy. *Int J Radiat Oncol Biol Phys* 1984;10(6):787-800.
 - 25. de Zwart JA, Vimeux FC, Palussiere J, Salomir R, Quesson B, Delalande C, Moonen CT. On-line correction and visualization of motion during MRI-controlled hyperthermia. *Magn Reson Med* 2001;45(1):128-137.



THE PREVIOUS CHAPTER HAS SHOWN THAT THE TEMPERATURE DEPENDENCE OF THE MAGNETIC SUSCEPTIBILITY OF TISSUE LEADS TO SIGNIFICANT TEMPERATURE ERRORS IN PRFS-BASED MRT AND THAT THIS INFLUENCE IS NOT ELIMINATED WHEN FAT SUPPRESSION TECHNIQUES ARE EMPLOYED. IT WAS POINTED OUT THAT FOR ACCURATE MR THERMOMETRY MEASUREMENTS, THE INFLUENCE OF SUSCEPTIBILITY CHANGES MAY NOT BE NEGLECTED.

RATHER, A MORE THOROUGH UNDERSTANDING OF THE RELATION BETWEEN TEMPERATURE AND MAGNETIC SUSCEPTIBILITY IS REQUIRED. ESPECIALLY THE TEMPERATURE DEPENDENCE OF THE SUSCEPTIBILITY OF FAT TISSUE IS OF INTEREST, SINCE IT WAS REPORTED TO BE IN THE SAME ORDER OF MAGNITUDE AS THE TEMPERATURE DEPENDENCE OF THE PROTON ELECTRON SCREENING CONSTANT OF WATER.

HOWEVER, NO VALUES WERE REPORTED IN LITERATURE ON THE TEMPERATURE DEPENDENCE OF THE SUSCEPTIBILITY OF HUMAN FAT TISSUE. THEREFORE, A STUDY WAS CONDUCTED IN WHICH THIS WAS MEASURED FOR HUMAN BREAST FAT TISSUE, RESULTS OF WHICH ARE DESCRIBED IN THE NEXT CHAPTER



5

TEMPERATURE DEPENDENCE OF THE MAGNETIC VOLUME SUSCEPTIBILITY OF HUMAN BREAST FAT TISSUE: AN NMR STUDY

INTRODUCTION

The increasing interest in MRI-guided thermal ablation therapy for breast tumors has heightened the need for reliable MR thermometry (MRT) techniques in tissues with high fat content. The currently most widely used MRT technique is proton resonance frequency shift (PRFS)-based MRT, which exploits the temperature dependence of the electron screening constant of water ($d\sigma_{\text{water}}/dT = 0.01 \text{ ppm}/^\circ\text{C}$ (1)). The electron screening constant of fat is near independent of temperature (2) and fat suppression techniques are therefore employed for PRFS-based MRT in fat containing tissues. The contribution of changes in the magnetic volume susceptibility χ (which will hereinafter be referred to as ‘susceptibility’) to the water proton resonance frequency (PRF) is commonly ignored in PRFS-based MRT. This disregards the fact that the susceptibility of fat, χ_{fat} , is temperature dependent (2,3). Heating-induced changes in the susceptibility distribution lead to non-local magnetic field changes. This, in turn, affects the PRF and, hence, the measured temperature of all water protons that experience this magnetic field change. Heating-induced susceptibility changes may therefore lead to errors in PRFS-based MR thermometry measurements during thermal therapy in tissues with high fat content, even when fat suppression techniques are employed. This has previously been shown for breast tumor ablation using High Intensity Focused Ultrasound (HIFU) (chapter 4 of this thesis).

In order to be able to estimate the impact of heating-induced susceptibility changes of

CHAPTER 5

fat on PRFS-based MRT during thermal therapy in the human breast, accurate measurements of the temperature dependence of the susceptibility, $d\chi/dT$, of human breast fat tissue are a prerequisite. However, values of the temperature dependence of the susceptibility of fat found in the literature were based on *in vitro* experiments in porcine fat samples, one of which was pre-cooked fat (2,3). In two *in vivo* studies, cooling of human calf tissue did not reveal temperature dependence of the susceptibility of fat, but these studies were performed at 1 T and 1.5 T and covered only small temperature ranges (4,5).

In this work we aimed to measure $d\chi/dT$ of human breast fat tissue. Since we are interested in susceptibility effects during thermal ablation therapy of breast tumors, the measurements were performed over a large temperature range. A technique from the field of NMR was applied, the double-reference method (6), which was developed to measure susceptibility while being invariant to the temperature dependence of the proton electron screening constant. This approach allows for susceptibility measurements within a single spectrum and therefore allows for $d\chi/dT$ measurements within one heating-cooling cycle. The experiments were performed on a 14.1 T NMR spectrometer for increased accuracy and precision.

METHODS

NMR spectroscopy

High resolution NMR spectra were acquired on a Bruker Avance Ultrashield spectrometer (Bruker Biospin GmbH, Rheinstetten, Germany) operating at a ^1H frequency of 600 MHz, and equipped with a triple resonance 5 mm TXI probe. A standard Bruker BVT-1000 variable temperature unit (VTU) was used to regulate the temperature of the air stream directed into the NMR probe. Temperature calibration was performed prior to the experiments to eliminate differences between the temperature as indicated on the spectrometer T_{spectro} (which is that of the thermocouple mounted near the sample), and the true sample temperature, T_{sample} . This was done by measuring the proton chemical shift difference Δ (in ppm) between the CH_2 and OH resonances of a dedicated temperature calibration sample (Bruker, 80% glycol DMSO-d 6) for a range of T_{spectro} temperatures, starting at $T_{\text{spectro}} = 24.85^\circ\text{C}$ (298 K) up to $T_{\text{spectro}} = 54.85^\circ\text{C}$ (328 K), in steps of 1 $^\circ\text{C}$. To ensure sufficient time for homogeneous temperature distribution within the sample, a temperature equilibration period of 20 minutes was allowed after the sample temperature had reached each step in the temperature sequence. Per spectrum, 4 scans were accumulated. The acquisition time was 0.85 sec, the spectral width was 16 ppm and the inter scan delay was set to 5 seconds to ensure complete recovery of equilibrium magnetization. Per spectrum, the actual temperature of the calibration sample was calculated using the empirically derived relationship (Bruker VTU manual):

$$T_{\text{sample}}(\text{ }^\circ\text{C}) = \frac{4.218 - \Delta}{0.009132} - 273.15 \quad [1]$$

For all fat susceptibility measurement experiments, the same heating protocol was ap-

TEMPERATURE DEPENDENCE OF MAGNETIC VOLUME SUSCEPTIBILITY OF HUMAN BREAST FAT

plied, and the temperature as indicated on the spectrometer was converted to the true sample temperature using the outcome of this temperature calibration experiment.

Fat tissue samples

Breast fat tissue samples were collected from six subjects directly post-mortem (all voluntary whole body donation, age subject I: 75, II: 50, III: 80, IV: 69, V: 93, VI: 78 years). The tissue samples were transferred into a 5 mm NMR sample tube. Air bubbles are detrimental for accurate susceptibility measurements and were removed as much as possible in the final NMR samples. Since our aim was to measure susceptibility changes of the tissue, no reference solvent or conservatives (e.g. formaldehyde) were added to the samples.

Measurement of $d\chi/dT$

To measure the temperature dependence of the susceptibility of fat tissue, without being hampered by changes of its proton electron screening constant σ , NMR experiments were performed using a double-reference method (6). This method employs a capillary-sphere (ω)-tube, filled with a reference solvent, which is placed inside an NMR sample tube containing the fat tissue (figure 1, Wilmad (Buena, NJ, USA; catalog item 529-A)).

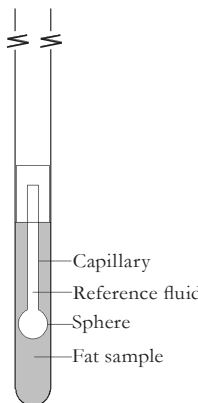


FIGURE 1 The experimental setup, consisting of a capillary-sphere (ω)-tube, filled with reference fluid, which is placed inside a 5-mm NMR sample tube. The sphere of the ω -tube is located in the center of the receiving coils sensitivity.

The magnetic field experienced by the nuclei of the reference solvent, B_{nuc} , is related to the location of the nuclei within the ω -tube. This is shown by Eq. 2 and 3, which describe the magnetic field at the nucleus inside a perfect cylinder, parallel to the main magnetic field, and sphere:

CHAPTER 5

$$B_{nuc, \text{capillary}} = B_0(1 - \sigma_{ref} + \frac{\chi_{ref}}{3}) \quad [2]$$

$$B_{nuc, \text{sphere}} = B_0(1 - \sigma_{ref} + \frac{\chi_{sample}}{3}) \quad [3]$$

with B_0 the main magnetic field, σ_{ref} the proton electron screening constant of the reference solvent, χ_{ref} the susceptibility of the reference solvent and χ_{sample} the susceptibility of the sample. In the spectrum of the ω -setup, two separate reference solvent peaks appear. The chemical shift difference in the positions $\delta_{ref, \text{capillary}}$ and $\delta_{ref, \text{sphere}}$ of the two reference solvent peaks is related to the difference in susceptibility between the reference solvent and the fat sample surrounding the reference solvent:

$$\delta_{ref, \text{capillary}} [\text{ppm}] - \delta_{ref, \text{sphere}} [\text{ppm}] = (g_{\text{capillary}} - g_{\text{sphere}})(\chi_{ref} - \chi_{sample}) \quad [4]$$

in which $(g_{\text{capillary}} - g_{\text{sphere}})$ is a factor related to the geometry of the set-up, which will be referred to in more detail below. Subsequently, χ_{sample} can be calculated using Eq. 5:

$$\chi_{sample}(T) = \chi_{ref}(T) - \frac{\delta_{\text{capillary}} - \delta_{\text{sphere}}}{G} \quad [5]$$

Theoretically, the geometric factor $G = (g_{\text{capillary}} - g_{\text{sphere}}) = 1/3$ for a set-up with a separate, perfect sphere and parallel cylinder. The shape of the ω -tube, however, is not a perfect cylinder and sphere, as shown in Fig. 1. G therefore needs to be predetermined by a calibration experiment, using a reference fluid and sample fluid with known susceptibilities:

$$G = \frac{\delta_{ref, \text{capillary}} [\text{ppm}] - \delta_{ref, \text{sphere}} [\text{ppm}]}{(\chi_{ref} - \chi_{sample, Gcal})} \quad [6]$$

The susceptibility of the sample fluid used for the G -calibration experiment is referred to as $\chi_{sample, Gcal}$ to avoid confusion with the susceptibility of the sample of interest.

In our application, the reference fluid in the ω -tube had to fulfill three requirements. First, its resonance peaks needed to lie well outside the fat tissue spectra covering 0.5 - 6 ppm. Furthermore, its signal intensity had to be sufficiently high to accurately determine the chemical shift difference of the two separate solvent peaks in the ω -tube. And last, its susceptibility had to have a known temperature dependence. Chloroform (CHCl_3) was chosen for our application. Although the temperature dependence of the susceptibility of CHCl_3 has not been reported in literature, it has been reported for the deuterated variant (CDCl_3). As is stated by Hoffman et al. (7), the temperature dependence of the susceptibility of CHCl_3 equals that of CDCl_3 , since it is reasonable to assume that isotopic substitution does not significantly affect the density variation

TEMPERATURE DEPENDENCE OF MAGNETIC VOLUME SUSCEPTIBILITY OF HUMAN BREAST FAT

with temperature and that the molar susceptibility is temperature independent. We thus used the following equation for the temperature dependence of CHCl_3 (based on Eq. 8 from (7)):

$$\chi_{\text{CHCl}_3} (\text{ppm}) = 4\pi(1.18 \cdot 10^{-11} T^4 + 8.8 \cdot 10^{-10} T^3 + 2.57 \cdot 10^{-7} T^2 + 9.1) \quad [7]$$

where T is the temperature in $^\circ\text{C}$.

The calibration of the geometric factor G was performed with CHCl_3 in the ω -tube and deuterated dimethyl sulfoxide (DMSO-d^6) as the sample solvent in the NMR tube. The temperature dependence of the susceptibility of DMSO-d^6 was reported by Hoffman et al. (based on Eq. 9 from (7)):

$$\chi_{\text{DMSO-d}^6} (\text{ppm}) = 4\pi(3.30 \cdot 10^{-7} T^2 + 5.13 \cdot 10^{-4} T - 0.6245) \quad [8]$$

where T is the temperature in $^\circ\text{C}$. To determine the geometrical factor G for our ω -sphere setup, eight 1D spectra were acquired at temperatures between $T = 23.5 \text{ } ^\circ\text{C}$ and $T = 65.4 \text{ } ^\circ\text{C}$. For the recording of the geometric calibration spectra a similar heating procedure was followed as for the fat tissue samples, with long equilibration times (15 minutes) between successive temperature points. Per spectrum, 4 scans were accumulated. The inter scan delay was set to 5 seconds, the acquisition time was 0.85 seconds and the spectral width was 16 ppm.

The CHCl_3 -filled ω -tube, which was used for the geometric calibration experiment, was cleaned with ethanol and transferred into the fat tissue sample tube. The ω -tube was positioned in the NMR tube such that the spherical part was located in the center of the receiving coil. Series of 1D proton spectra of the ω -setup were acquired covering a temperature interval between $T = 23.5 \text{ } ^\circ\text{C}$ and $T = 65.4 \text{ } ^\circ\text{C}$. Both the upward and downward temperature profiles (31 temperature points each) were acquired to investigate possible hysteresis effects due to temperature-induced changes in the fat tissue sample. To ensure a homogeneous temperature distribution within the sample, a temperature equilibration period of 20 minutes was used at every temperature point. Typically, 16 scans were accumulated per spectrum. The acquisition time was 0.85, the spectral width was 16 ppm and the inter scan delay was set to 5 seconds to ensure complete recovery of equilibrium magnetization. Prior to and after the complete heating-cooling cycle, the sample was visually inspected to detect possible changes in the fat tissue.

NMR spectra were collected in the absence of a deuterated solvent in the fat tissue or the ω -tube and thus without the possibility of field lock. The short-term and long-term field drift of the ultrashielded magnet in unlocked mode amounts to less than 2 Hz per day and therefore the magnetic field stability was considered sufficiently good to repeatedly extract the absolute chemical shift changes over time during the temperature series of the fat samples. Proton chemical shifts were given with reference to tetramethylsilane (TMS) which was dissolved in the chloroform of the ω -tube. The most upfield shifted line of TMS arising from the capillary part was used as the 0 ppm reference.

Data analysis

All spectra were acquired with Bruker Topspin 2.1 software and analyzed using MestRe-C 4.9.9.6 [Mestrelab Research, Santiago de Compostela, Spain]. The acquired FID's were apodized with a 10-Hz exponential filter prior to the Fourier transform. Zeroth and first order phase correction was manually applied per spectrum to achieve a flat baseline over the entire spectral range. The peak positions $\delta_{\text{capillary}}$ and δ_{sphere} of the reference solvent were then determined by the peak picking algorithm as implemented in MestRe-C. The susceptibility of the fat tissue was calculated per spectrum (i.e. per temperature step) using Eq. 5 and Eq. 7, and was plotted against temperature. A linear fit was performed to determine $d\chi_{\text{fat}}/dT$ for each sample.

RESULTS

Two 1D spectra of human breast fat, acquired at two different temperatures ($T = 23.52^\circ\text{C}$ and at $T = 65.43^\circ\text{C}$) are shown in figure 2. A part of the spectrum zoomed at the location of the CHCl_3 reference peaks ($\delta_{\text{ref,capillary}}$, right peak and $\delta_{\text{ref,sphere}}$, left peak) is shown.

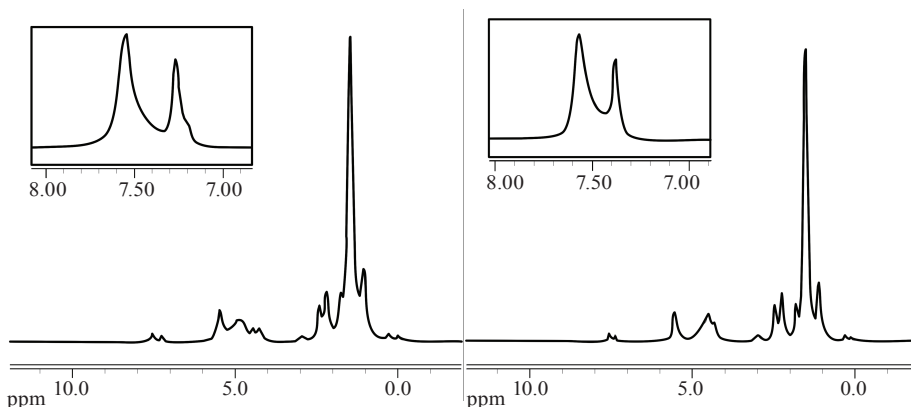


FIGURE 2 Two spectra of breast fat tissue, at $T = 23.5^\circ\text{C}$ (left) and at $T = 65.4^\circ\text{C}$ (right). On the far left, the two CHCl_3 reference peaks are visible. A zoomed version of both spectra at the location of the two reference peaks (capillary peak (left) and sphere peak (right)) is shown in the inset.

TEMPERATURE DEPENDENCE OF MAGNETIC VOLUME SUSCEPTIBILITY OF HUMAN BREAST FAT

The measured susceptibility of breast fat over temperature for all six samples is shown in figure 3. The measurements of the whole heating-cooling cycle are plotted, the start of which is indicated with the larger dot. For all samples, a temperature dependence of the magnetic volume susceptibility is observed. The dependence is overall linear and the results of a linear fit through the data are presented in Table I.

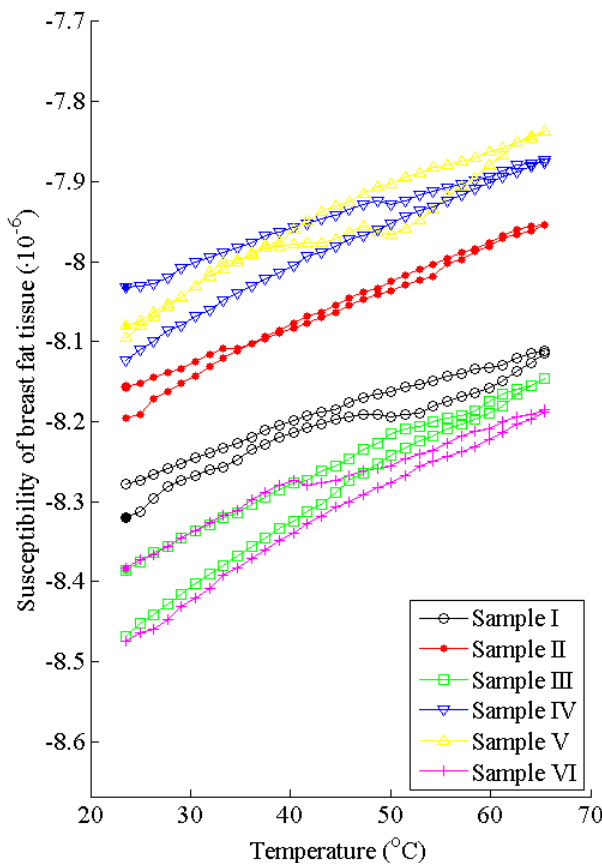


FIGURE 3 The temperature dependence of the magnetic susceptibility of six human breast fat samples.

CHAPTER 5

TABLE I Temperature dependence of the susceptibility of six breast fat samples. The bottom two rows show the mean and standard deviation of $d\chi_{fat}/dT$ over all samples during temperature rise and fall, respectively.

Sample		$d\chi_{fat}/dT$ (ppm/ $^{\circ}$ C)
I	rise	0.0041
	fall	0.0040
II	rise	0.0049
	fall	0.0058
III	rise	0.0057
	fall	0.0076
IV	rise	0.0038
	fall	0.0058
V	rise	0.0051
	fall	0.0060
VI	rise	0.0044
	fall	0.0068
rise		0.0046 \pm 0.0008
fall		0.0060 \pm 0.0012

The average $d\chi_{fat}/dT$ and its standard deviation over all samples was 0.0046 ± 0.0008 ppm/ $^{\circ}$ C during slow temperature rise and 0.0060 ± 0.0012 ppm/ $^{\circ}$ C during the slow temperature fall. There is a spread in the absolute χ values of the samples. The values are, however, in agreement with the reported susceptibility value of animal fat ($-7.79 \cdot 10^{-6}$) (8).

All fat tissue samples were opaque prior to the measurement of $d\chi_{fat}/dT$. After the experiments, four out of six fat tissue samples were partially translucent. The composition of these samples was altered during the heating, and an oily substance was present, likely due to melting of the sample. However, in two cases, the samples were still opaque after the heating-cooling cycle.

DISCUSSION AND CONCLUSIONS

In this work, the temperature dependence of the magnetic susceptibility of human breast fat was measured. The experiment was performed for six breast fat samples, all of which exhibited a linear temperature dependence of the susceptibility.

The measured $d\chi_{\text{fat}}/dT$ values ranged from 0.0038 up to 0.0076 ppm/ $^{\circ}\text{C}$ between the samples. This spread in $d\chi_{\text{fat}}/dT$ may be explained by intersubject variation. The fat tissue samples were kept untreated to exclude pollution and verify that the original lipid components were preserved. For the same reason, we did not homogenize the samples prior to the measurements. However, the samples were surgically removed directly post-mortem, which lead to the presence of blood traces in the fat. Even though the amount of blood was minimal, it varied over the samples and may have contributed to the range of found $d\chi_{\text{fat}}/dT$ values. In addition, redistribution of the lipid material after ‘melting’ the fatty matrix at elevated temperatures is a possible source of errors. Phase transition from gel phase to liquid phase was observed in four samples. Lower molecular weight phospholipids with chain lengths C14 and C16 have lower chain-melting phase-transition temperatures compared to e.g. C18 lipids (9), resulting in a liquid fraction at the top of the sample that floats on the more solid fat tissue. This may have added to the hysteresis effects observed for the susceptibility in the downward temperature curves.

In this work, the temperature dependence of the magnetic susceptibility of fat tissue samples was measured using a technique that was previously developed for susceptibility measurements at constant temperatures. The application of this technique over a large range of temperatures introduced an extra procedure which involved the determination of the set-up related geometric factor G over the same temperature range. This geometric factor was found to be temperature dependent, and a second order nonlinear fit was used to interpolate the outcome of the G -calibration data to all temperature values within the heating-cooling cycle.

A spread in the χ values at starting temperature was also observed, which may be explained by the experimental set-up. The experimental set-up employed a capillary-sphere plug-in. This specific shape complicates shimming of the sample. It was observed that the shim settings influenced the peak position of the sphere, $\delta_{\text{ref},\text{sphere}}$, more than it influenced the capillary peak. A change the peak position difference will influence the outcome for χ_{fat} (Eq. 5). The shimming process was therefore optimized per sample by minimizing the peak widths of $\delta_{\text{ref},\text{sphere}}$ and $\delta_{\text{ref},\text{capillary}}$. However, this effect still may have contributed to the observed spread in absolute χ_{fat} values.

The average $d\chi_{\text{fat}}/dT$ values during temperature rise and temperature fall were 0.0046 ± 0.0008 ppm/ $^{\circ}\text{C}$ and 0.0060 ± 0.0012 ppm/ $^{\circ}\text{C}$, respectively. These values are somewhat smaller, but in the same order of magnitude as the reported temperature dependence of χ_{fat} in porcine precooked fat (0.00804 ± 0.00145 ppm/ $^{\circ}\text{C}$ (2)). In previous work, heating experiments were conducted which showed that a temperature dependence of the susceptibility of ~ 0.005 ppm/ $^{\circ}\text{C}$ leads to errors in MR temperature measurements (chapter 4 of this thesis). The current work shows that human breast fat experiences heating-induced susceptibility changes. It is concluded that the impact of heat-induced susceptibility changes during thermal therapy of fatty tissues may not be neglected.

REFERENCES

1. Hindman JC. Proton Resonance Shift of Water in the Gas and Liquid States. *Journal of Chemical Physics* 1966;44:4582-4592.
2. Stollberger R, Ascher PW, Huber D, Renhart W, Radner H, Ebner F. Temperature monitoring of interstitial thermal tissue coagulation using MR phase images 2. *J Magn Reson Imaging* 1998;8(1):188-196.
3. De Poorter J. Noninvasive MRI thermometry with the proton resonance frequency method: study of susceptibility effects. *Magn Reson Med* 1995;34(3):359-367.
4. Young IR, Hajnal JV, Roberts IG, Ling JX, Hill-Cottingham RJ, Oatridge A, Wilson JA. An evaluation of the effects of susceptibility changes on the water chemical shift method of temperature measurement in human peripheral muscle. *Magn Reson Med* 1996;36(3):366-374.
5. Young IR, Bell JD, Hajnal JV, Jenkinson G, Ling J. Evaluation of the stability of the proton chemical shifts of some metabolites other than water during thermal cycling of normal human muscle tissue. *J Magn Reson Imaging* 1998;8(5):1114-1118.
6. Frei K, Bernstein HJ. Method for Determining Magnetic Susceptibilities by NMR. *Journal of Chemical Physics* 1962;37:1891-1892.
7. Hoffman RE, Becker ED. Temperature dependence of the ^1H chemical shift of tetramethylsilane in chloroform, methanol, and dimethylsulfoxide. *J Magn Reson* 2005;176(1):87-98.
8. Hopkins JA, Wehrli FW. Magnetic susceptibility measurement of insoluble solids by NMR: magnetic susceptibility of bone. *Magn Reson Med* 1997;37(4):494-500.
9. Cevc G. How membrane chain-melting phase-transition temperature is affected by the lipid chain asymmetry and degree of unsaturation: an effective chain-length model. *Biochemistry* 1991;30(29):7186-7193.

TEMPERATURE DEPENDENCE OF MAGNETIC VOLUME SUSCEPTIBILITY OF HUMAN BREAST FAT

← IN THE PREVIOUS CHAPTERS, VARIOUS SOURCES OF ERRORS IN PRFS-BASED MR THERMOMETRY HAVE BEEN EXPLORED. BESIDES RESPIRATION (CHAPTER 3), THE HEATING OF FAT TISSUE WAS INDICATED AS A POTENTIAL SOURCE OF ERRORS (CHAPTER 4 AND 5). THE INFLUENCE OF THE SUSCEPTIBILITY CHANGES OF FAT HAS BEEN STUDIED IN DETAIL. AS POINTED OUT IN CHAPTER 2, BESIDES THE FACT THAT FAT SIGNIFICANTLY HAMPERS PRFS-BASED MRT THROUGH ITS TEMPERATURE DEPENDENT SUSCEPTIBILITY, THE PRESENCE OF FAT IS UNDESIRED IN PRFS-BASED MRT BECAUSE THE PROTON ELECTRON SCREENING CONSTANT OF FAT IS NEAR INDEPENDENT OF TEMPERATURE.

NEVERTHELESS, THE LATTER MAY BE USED TO OUR BENEFIT. FAT MAY BE USED AS A REFERENCE WHICH WOULD ALLOW FOR ABSOLUTE RATHER THAN RELATIVE MR TEMPERATURE MEASUREMENTS. MULTIPLE RESONANCES CAN BE SEPARATELY DETECTED IN SPECTROSCOPIC DATA, WHICH CAN BE ACQUIRED AT HIGH TEMPORAL AND SPATIAL RESOLUTION USING A MULTI GRADIENT-ECHO (MGE) SEQUENCE. VARIOUS ACQUISITION AND POST-PROCESSING METHODS HAVE BEEN PROPOSED FOR MGE-BASED MR THERMOMETRY. WE HAVE AIMED TO FURTHER EXPLORE THE POSSIBILITIES OF MGE-BASED MR THERMOMETRY →

6

ABSOLUTE MR THERMOMETRY USING TIME DOMAIN ANALYSIS OF MULTI GRADIENT-ECHO MAGNITUDE IMAGES

INTRODUCTION

MRI offers, besides excellent soft tissue contrast, the possibility for non-invasive temperature measurements, which has great potential for image-guided thermal therapy. Currently, proton resonance frequency shift (PRFS)-based MR thermometry (MRT) is the method of choice for acquiring temperature maps with MRI (1). The PRFS technique exploits the temperature dependence of the proton resonance frequency (PRF) of water. A temperature change ΔT is known to give rise to a change in the electron screening constant σ of water protons ($d\sigma_{\text{water}}/dT = 0.01 \text{ ppm}/^{\circ}\text{C}$ (2)) and thus to a shift of the PRF. Such frequency shifts can be determined by measuring the corresponding phase changes $\Delta\varphi$ between gradient-echo scans. Per voxel, $\Delta\varphi$ is proportional to the local temperature change between the time points of the acquisition of the phase images.

PRFS-based MRT has several limitations. First, no information on absolute temperatures can be given without a known absolute temperature distribution at the start of the measurement. Absolute temperature data is required when thermal dose calculations are employed, for example for the monitoring of tissue response during thermal ablation therapy (3). Second, subsequent temperature measurements need to be performed at the exact same location. No motion is therefore allowed. Third, the temperature change is found by subtraction of phase images. Therefore, temporal phase fluctuations other than those related to the temperature effect, e.g. due to field drift or respiration induced field fluctuations (4), will lead to erroneous temperature measurements. And fourth, the presence of fat hampers the applicability of the PRFS-based MRT method. This is due to the fact that the temperature dependence of the proton electron screen-

CHAPTER 6

ing constant of fat is very small compared to that of water ($d\sigma_{\text{fat}}/dT = 0.00018 \text{ ppm}/^{\circ}\text{C}$ (5)). In fat, the PRFS method can therefore not be applied. In voxels containing both water and fat, the phase change of the sum signal does not represent the temperature change correctly. For accurate MR thermometry in regions of the body containing fat, fat suppression techniques are therefore required. Techniques have been developed to solve these issues, for example referenceless MR thermometry, which brings a solution to the problems regarding motion and field changes (6,7). This technique, however, does not allow for absolute temperature measurements, nor does it solve the problems related to fat.

An MR technique that can be used for thermometry and which is not affected by the limitations mentioned above, is MR spectroscopy (MRS). The PRFS, and hence temperature changes, can be determined from the shift of the water peak in subsequent spectra (8). Furthermore, it allows for absolute temperature measurements by exploiting the frequency difference $\Delta f(T)$ between a temperature sensitive PRF and the PRF of a temperature insensitive reference component (9). Temperature insensitive references that have been suggested are, for example, the before mentioned fat resonance, and the NAA peak in brain tissue (10). The reference-based approach also has the benefit of being insensitive to local field disturbances $\Delta B(\vec{r})$ and temporal field fluctuations $\Delta B(t)$ (e.g. field drift). This is due to the fact that the PRF of both resonances will be equally affected by such field disturbances up to a very high level of precision, which leaves $\Delta f(T)$ unaffected. A major drawback of MRS and particularly MR Spectroscopic Imaging (MRSI) is their low spatial and temporal resolution, making these techniques unsuitable for the real-time guidance of thermal therapy.

However, it is possible to acquire spectroscopic data at high temporal and spatial resolution by using a multi gradient-echo (mGE) sequence (11). In this image-based technique, multiple (n) gradient-echo images are acquired at echo times $TE_i = TE_1 + (i-1)\Delta TE$ for $i = 1, 2, \dots, n$, with TE_1 the echo time at which the first gradient-echo image is acquired and ΔTE the echo spacing. A spectrum can be obtained per voxel, of which the spectral bandwidth (SBW) is determined by the echo spacing. Several studies on the applicability of mGE techniques for MR thermometry have been undertaken and various approaches for both acquisition and post-processing have been explored (12-16). While promising, the development towards an mGE-based technique for the real-time guidance of thermal therapy has thus far been hampered by system limitations and post-processing constraints.

In the present study, we aimed to further develop the mGE-based absolute MRT technique. Current hardware capabilities were optimally exploited, using faster gradient switching rates and stronger gradients, resulting in sufficiently small echo spacings to avoid the use of interleaved scanning. With such a fast and powerful gradient system, read-out can be performed exclusively at positive polarity of the read-out gradients, using rewinder-gradients. This eliminates the extra post-processing steps that were formerly required after symmetric acquisition for time reversal of the negative polarity read-out data (16). Furthermore, we investigated the possibility of post-processing the mGE data into absolute temperature maps using the magnitude of the mGE signals in the time domain. For the specific application we have in mind, which is absolute MR thermometry based on two resonances, retrieving the frequency difference between

these two resonances is the sole requirement. The most straightforward approach would be to stay with the measured data in the time domain, which reduces the number of post-processing steps. In addition, we have chosen to use the magnitude images to eliminate phase effects. A model describing the magnitude signal behaviour in time is fitted to the acquired magnitude signal over all echoes. A similar method has previously been successfully applied for the T_2^* -analysis of the interferogram-like relaxation curves of bone marrow (17). In the current paper we will show that this approach is also applicable for absolute MR thermometry. In this case, instead of the relaxation parameters, the frequency difference $\Delta f(T)$ is the parameter of interest. In our approach, $\Delta f(T)$ is obtained directly in a single post-processing step, in contrast to methods which indirectly compute $\Delta f(T)$ after fitting the separate frequencies in the frequency domain (12-14). We will also show that the time domain analysis of the magnitude signals is insensitive to both field drift and local field disturbances.

To validate the proposed techniques and to show the insensitivity of the time domain-based post-processing to field drift and local field disturbances, *in vitro* experiments were performed, using ethylene glycol (EG) as a test fluid. The spectra of EG contain two spectral resonances. The temperature dependence of $\Delta f(T)$ for these resonances is very well described (18), making it an ideal test fluid for absolute temperature measurements. To show the applicability of the time domain-based mGE MRT technique in biological tissue containing water and fat, *ex vivo* experiments were performed on bone marrow of an ovine hind limb. Absolute temperature maps were acquired of the same sample, before and after heating of the tissue. The fat resonance was employed as a reference component.

METHODS

Theory

The magnitude signal of a voxel containing two spectral resonances 1 and 2 at time t is given by:

$$S(t) = \sqrt{A_1^2 e^{-2R_{2,1}^* t} + A_2^2 e^{-2R_{2,2}^* t} + 2A_1 A_2 e^{-(R_{2,1}^* + R_{2,2}^*)t} \cos(2\pi\Delta f_{12}t + \Delta\phi_{12})} \quad [1]$$

with A_1 and A_2 the effective spin densities, including effects of the longitudinal relaxation time T_1 , $R_{2,1}^*$ and $R_{2,2}^*$ the effective transverse relaxation rates, Δf_{12} the resonance frequency difference in Hertz and $\Delta\phi_{12}$ the phase offset difference between the two resonances in radians. The frequency difference Δf_{12} is the parameter of interest for absolute MR thermometry.

Experiments

All experiments were performed on a clinical 3-T whole body MRI scanner (Achieva, Philips Healthcare, Best, The Netherlands). In figure 1, the pulse sequence diagram of the multi gradient-echo pulse sequence is shown schematically. In all scans, 32 echoes were acquired at positive polarity of the read-out gradients. All scans were non-inter-

CHAPTER 6

leaved. The relevant scan parameters are given below. For all experiments, the temperature was verified by fiber optic temperature measurements (Luxtron, Santa Clara, CA, USA) at a sample rate of 1 s^{-1} .

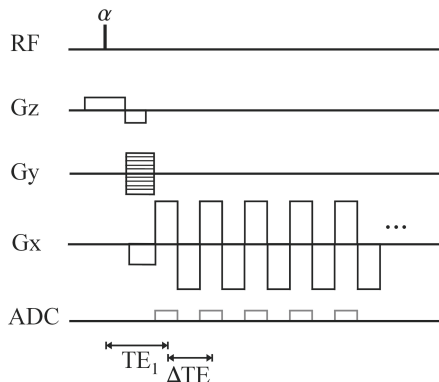


FIGURE 1 The multi gradient-echo sequence. In the present study, read-out is performed exclusively at positive polarity of the read-out gradients. The first five gradient-echoes are shown. In total, 32 acquired echoes were acquired in all scans.

In vitro experiments

Four *in vitro* experiments were conducted, each of them designed to study a specific aspect of the performance of the time domain-based mGE MRT technique. Ethylene glycol (Alfa Aesar, Karlsruhe, Germany) was used as a phantom fluid for all *in vitro* scans. The relation between the temperature of EG and the resonance frequency difference $Δf_{hm}$ between the hydroxyl (h) and methylene (m) group in EG is given by (18):

$$T[^\circ\text{C}] = 193.35 - 1.02 \cdot 10^8 \cdot Δf_{hm}[\text{Hz}] / γB_0 \quad [2]$$

The phantom consisted of a Perspex cylinder filled with EG fluid (total length 24 cm; length of part filled with EG 18 cm; inner radius 1.5 cm) which was placed inside isolation material, to prevent temperature fluctuations during scanning (figure 2). The phantom was placed in the scanner with its long axis parallel to the main magnetic field.

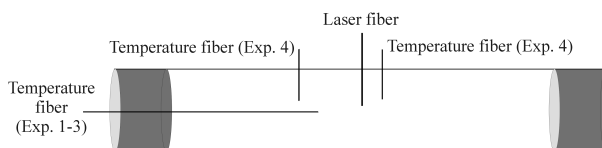


FIGURE 2 Schematic drawing of the cylindrical phantom used for the *in vitro* experiments. The location of the optical temperature fibers and laser fiber are indicated.

For all scans, a coronal 2D single slice was acquired, using the following scan param-

ABSOLUTE MRT USING TIME DOMAIN ANALYSIS OF mGE MAGNITUDE IMAGES

eters: FOV 100x200 mm²; slice thickness 10 mm; flip angle $\alpha = 30^\circ$; number of signal averages = 1; read-out gradient strength $G_R = 28$ mT/m. The echo time of the first echo was $TE_1 = 1.8$ msec and the echo spacing was $\Delta TE = 1.8$ msec, corresponding to a SBW of 555 Hz. This ΔTE led to the acquisition of a non-aliased signal (at $B_0 = 3$ T: $\Delta f_{\text{hm}}(T = 20^\circ\text{C}) = 217.2$ Hz and $\Delta f_{\text{hm}}(T = 50^\circ\text{C}) = 179.6$ Hz). The repetition time TR and acquired matrix are given below per experiment.

1. Absolute temperature mapping

In this experiment we studied the ability of the time domain-based mGE MRT technique to yield absolute temperature maps. Three scans of the EG-filled cylinder were acquired. During the first scan, the EG was at constant room temperature. Prior to the second and third scan, the temperature of the EG fluid was increased by placing the cylinder in a warm water bath with a constant temperature of 35 °C and 50 °C, respectively. Sufficient time (> 5 hours) was allowed for temperature stabilization. Acquired matrix 64x128; repetition time TR = 60 msec; scan duration = 4 sec.

2. Influence of temporal field fluctuations $\Delta B(t)$: field drift

To study the influence of field drift on the time domain-based mGE MRT outcome, 60 mGE scans were acquired with the EG fluid kept at constant room temperature. To quantify the field drift, Fourier spectra of the zero-filled complex signal within a region of interest (ROI) were computed for the first and last scan. Subsequently, the peak position of the methylene peak was determined for the spectra from the first and last scan using a Gaussian fit. The field drift was quantified by subtraction of the found peak positions, and expressed in expressed in parts-per-million (ppm). Acquired matrix 64x128; TR = 100 msec; scan duration 6.4 sec. Total time for 60 scans was 6 minutes and 25 seconds.

3. Influence of local field disturbances $\Delta B(\vec{r})$

To study the influence of local field disturbances on the absolute temperature maps, two scans were acquired of the cylinder. For both scans, the EG fluid was kept at the same, constant temperature. In the set-up of the second scan, a fluid-filled bottle was placed in the proximity of the EG cylinder to disturb the homogeneity of the magnetic field, i.e. to create local field disturbances. Acquired matrix 64x128; TR = 60 msec; scan duration = 4 sec.

4. Heating experiment

This experiment was designed to assess the feasibility of using the time domain-based mGE MRT technique as a tool for the guidance of a thermal intervention. In this set-up, the cylinder was filled with EG gel. The EG gel was prepared by adding 3% Agarose (Lonza, Rockland, ME, USA) to the EG fluid. Verification with MR Spectroscopy showed that the peak positions in the Fourier spectra acquired of the EG gel were the same as those for the EG fluid. A laser fiber for local heating (core diameter 400 µm, active zone 25 mm, KLS Martin, Umkirch, Germany) was inserted into this gel through a hole in the cylinder (figure 2). A total of 45 mGE scans were acquired. During scan-

CHAPTER 6

ning, the EG gel was locally heated by a laser (TT YAG 80 laser, $\lambda = 1064$ nm, Trumpf, Ditzingen, Germany) using constant power of 7 Watt for 90 seconds. Acquired matrix 45x128; $TR = 100$ msec; scan duration = 4.5 sec. Total scan time was 3 minutes and 23 seconds.

For experiments 1-3, an optical temperature fiber was inserted through a hole in the top end of the cylinder, parallel to the cylinder's longitudinal axis (figure 2). For the laser heating experiment, both the laser fiber and two optical temperature fibers were inserted perpendicular to the cylinder's longitudinal axis (figure 2).

Ex vivo experiments

To study the feasibility of mGE-based absolute temperature mapping in biological tissue containing water and fat resonances, *ex vivo* experiments were performed in the bone marrow inside an ovine hind limb. The relation between absolute temperature and the resonance frequency difference Δf_{wf} between water (w) and fat (f) in tissue can be described by the following equation:

$$T[^{\circ}C] = \frac{1}{\alpha[ppm]} \left(CS[ppm] - \frac{\Delta f_{wf}[Hz]}{\gamma B_0 10^{-6}} \right) + T_{ref} \quad [3]$$

in which α is the electron screening constant thermal coefficient of water and CS is the chemical shift between water and fat at the reference temperature T_{ref} . In the current study, the following values were used for the calculation of temperature from Δf_{wf} : $\alpha = 0.01$ ppm/ $^{\circ}C$ (2) and $CS = 3.35$ ppm at $T_{ref} = 37$ $^{\circ}C$.

5. Ex vivo bone marrow heating experiment

Two scans were performed. During the first scan, the temperature of the ovine hind limb was constant and at room temperature. Prior to the second scan, the temperature of the bone marrow was increased by placing the *ex vivo* material in a warm water bath (45 $^{\circ}C$) for over 6 hours. Both scans were acquired at coronal orientation. The following scan parameters were used: FOV 196 x 220 mm²; acquired matrix 72 x 111; slice thickness 4.5 mm; flip angle $\alpha = 30^{\circ}$; number of signal averages = 1; read-out gradient strength $G_R = 39$ mT/m. The echo time of the first echo was $TE_1 = 1$ msec and the echo spacing was $\Delta TE = 1.2$ msec, corresponding to a SBW of 833 Hz. The ΔTE chosen led to the acquisition of aliased signals (at $B_0 = 3$ T: $\Delta f_{wf}(T = 20$ $^{\circ}C) = 450$ Hz and $\Delta f_{wf}(T = 40$ $^{\circ}C) = 424$ Hz). $TR = 500$ msec; scan duration was 57 seconds. In the *ex vivo* experiment, the optical temperature fiber was inserted into the hind limb to where it touched the bone.

Post-processing – mGE magnitude signal fitting in time domain

For all experiments, Δf_{12} was found by fitting the signal model as given in Eq. [1] to the discrete samples of the magnitude signal acquired at subsequent echo times per pixel using a nonlinear least squares trust region fit procedure (Mathworks, Natick, MA,

USA). All acquired echoes were used in the fitting process (a total of 32). The following six fit parameters were used: Δf_{12} , A_1 , A_2 , $R^*_{2,1}$, $R^*_{2,2}$ and $\Delta\varphi_{12}$. Since Δf_{12} is the parameter of interest, the fitted value for this parameter needs to be as independent as possible of its starting value. The starting values of A_1 , A_2 , $R^*_{2,1}$, $R^*_{2,2}$ and $\Delta\varphi_{12}$ were chosen in such a way that reliable and stable output values were computed for Δf_{12} within a large range of Δf_{12} starting values. They were set to the following values for both the *in vitro* and the *ex vivo* post-processing: $A_{1,start} = 0.6 \cdot A_{max}$ and $A_{2,start} = 0.4 \cdot A_{max}$, in which A_{max} is the maximum magnitude signal amplitude in the voxel of interest, $R^*_{2,1,start} = 10 \text{ sec}^{-1}$, $R^*_{2,2,start} = 10 \text{ sec}^{-1}$, $\Delta\varphi_{12,start} = 0$. The starting value for Δf_{12} was set to the frequency difference which corresponds to an absolute temperature of 21 °C, resulting in $\Delta f_{hm,start} = 215.9 \text{ Hz}$ for the experiments with ethylene glycol, and $\Delta f_{wf,start} = 448.6 \text{ Hz}$ for the experiments in bone marrow. Note that the value of $\Delta f_{12,start}$ does not necessarily match the actual temperature of the phantom or sample. After the fitting procedure, the resulting values for Δf_{12} were converted for each pixel into absolute temperature using Eq. [2] (for ethylene glycol experiments) or Eq. [3] (for experiments in bone marrow).

In the field of mGE-based absolute MR thermometry, emphasis has been on post-processing in the frequency domain. For the *in vitro* scans of experiment 3 and the *ex vivo* bone marrow scans, the performance of the post-processing in the time domain was therefore related to a repeatedly used post-processing technique in the frequency domain. The frequency domain post-processing technique which was implemented has previously been described and applied in the breast (14, 15). Fourier transformation of the complex MR signal was performed after zero-filling to 128. The spectra were analyzed by nonlinear fits of the two peaks in the spectra to Gaussian functions, using the Levenberg-Marquardt algorithm. The two peaks were the methylene and hydroxyl peak for the *in vitro* scans, and the water and fat peak for the *ex vivo* scans. For the *in vitro* scans, peak fitting was performed in a +/- 17 Hz region around the maximum of the peaks (corresponding to a total of 9 data points). For the *ex vivo* scans, this range was set to +/- 33 Hz (corresponding to a total of 11 data points), since the peaks in the bone marrow spectra were broader than those in the *in vitro* spectra.

RESULTS

1. Absolute temperature mapping

Three absolute temperature maps of the EG-filled cylinder at three different constant temperatures are shown in figure 3. For each scan, the average absolute mGE-based temperature (T) and the standard deviation were calculated within a square ROI of 7x7 pixels, placed at the location of the optical temperature fiber. This ROI is depicted as the black square in all temperature maps in figure 3. The temperatures measured with fiber optical temperature sensor (T_f) were averaged over the scan duration. The results per scan were: (1) $T = 22.8 \pm 0.04 \text{ }^\circ\text{C}$ and $T_f = 22.8 \text{ }^\circ\text{C}$; (2) $T = 34.6 \pm 0.05 \text{ }^\circ\text{C}$ and $T_f = 34.7 \text{ }^\circ\text{C}$; (3) $T = 49.3 \pm 0.06 \text{ }^\circ\text{C}$ and $T_f = 49.2 \text{ }^\circ\text{C}$. Comparing the optical fiber measurements with the temperature data as calculated using the time domain-based mGE MRT method shows a very good correspondence.

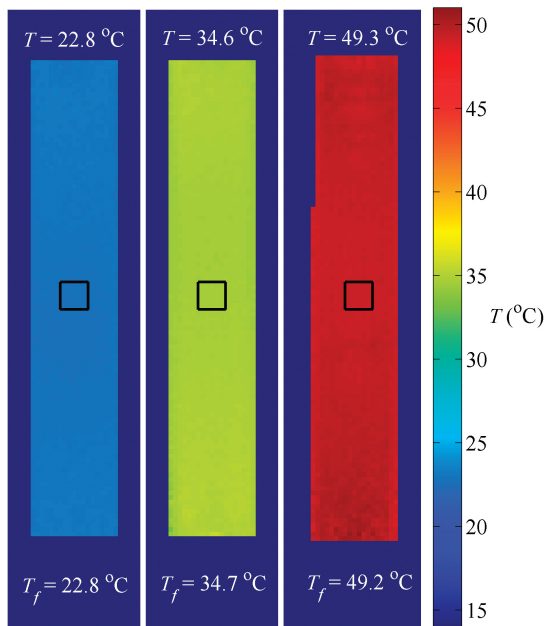


FIGURE 3 Three absolute temperature maps of ethylene glycol at different temperatures. The average absolute temperature T , calculated by averaging the temperature within an ROI (indicated by the black square), is displayed above each map. The optical temperature measurements T_f are displayed at the bottom of each temperature map.

2. Influence of temporal field fluctuations $\Delta B(t)$: field drift

Figure 4a shows two absolute temperature maps of the EG-filled cylinder at room temperature. The left temperature map corresponds to the first scan (number 1) and the temperature map on the right to the last scan (number 60, acquired at $t = 6$ minutes and 19 seconds). The average temperature and standard deviation within a square ROI of 7x7 pixels, depicted as the black square in figure 4a, are: $T = 20.1 \pm 0.04 \text{ } ^\circ\text{C}$ for the first scan and $T = 20.1 \pm 0.05 \text{ } ^\circ\text{C}$ for the last scan. The optical fiber measurements showed no heating of the EG during this scan. Figure 4b shows the frequency spectra of the zero-filled complex mGE signal taken from the same two ROI's. These spectra, being sensitive to field disturbances, have clearly shifted over time, indicating the presence of magnetic field drift. This field drift was 0.70 ppm over the duration of the experiments (6 minutes and 25 seconds), which could erroneously be interpreted as a temperature change of about 70 $^\circ\text{C}$ in PRFS-based MRT without drift correction. The time domain-based mGE MR temperature maps are, however, clearly unaffected by this drift.

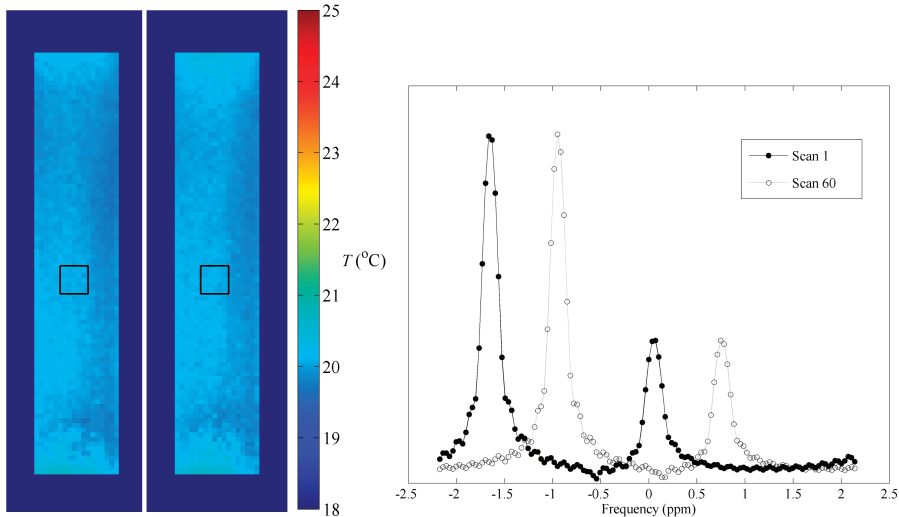


FIGURE 4 On the left, two absolute temperature maps of ethylene glycol are shown, corresponding to the first (left) and last (right) scan from a series of 60 scans. The ROI's in which the average absolute temperature is calculated are shown as a black square. On the right, two spectra of the zero-filled Fourier transformed complex signal from the ROI's of scan 1 (drawn line, black dots) and scan 60 (dashed line, open circles) are shown. Clearly visible is the shift in the spectrum (0.70 ppm) due to field drift.

3. Influence of local field disturbances $\Delta B(\vec{r})$

In this experiment, absolute temperature maps were computed using both the time domain-based and the frequency domain-based technique. The results are shown in figure 5a and b, respectively. The absolute temperature maps of the scans without and with a field disturbing object placed near the EG-filled cylinder are depicted. In the corresponding phase images (acquired at $TE = 12.6$ msec), shown in figure 5c, the induced field disturbance has led to a phase wrap in the right phase image. This indicates that the PRFS-based MRT technique would yield temperature difference maps which would be severely disturbed. The mGE MRT techniques however, yielded overall homogeneous absolute temperature maps for both scans.

In order to quantitatively compare the time domain-based temperature (T) with the frequency domain-based temperature (T_{freq}), the average temperature and standard deviation were computed over the whole cylinder and within an ROI of 7x7 pixels which was placed at the location of the field disturbance. The results for the whole cylinder were: $T = 21.1 \pm 0.10$ °C versus $T_{\text{freq}} = 21.0 \pm 0.13$ °C (scan 1) and $T = 21.1 \pm 0.27$ °C versus $T_{\text{freq}} = 20.7 \pm 0.63$ °C (scan 2). And within the ROI: $T = 21.1 \pm 0.05$ °C versus $T_{\text{freq}} = 20.9 \pm 0.05$ °C (scan 1) and $T = 20.8 \pm 0.14$ °C versus $T_{\text{freq}} = 19.8 \pm 0.20$ °C (scan 2).

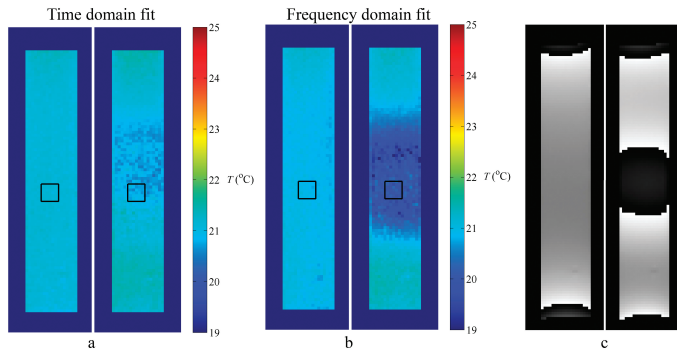


FIGURE 5 (a) Two time domain-based absolute temperature maps of ethylene glycol without (left) and with (right) field disturbances. (b) Two frequency domain-based absolute temperature maps of ethylene glycol without (left) and with (right) field disturbances. The ROI's in which the average absolute temperature is calculated are shown as a black square. (c) Two phase images of the EG fluid acquired at TE = 12.6 msec. The left phase image is homogeneous. The right phase image shows a phase wrap in the center of the phantom, indicating the presence of a field disturbance, caused by a bottle with phantom fluid which was placed nearby.

These results show a small temperature offset of the frequency-based method versus the time domain-based method in case of a field disturbance. Both methods experience an increase of noise in the mGE-based temperature outcome. To give more insight in this, the magnitude signal in time and the zero-filled Fourier spectra from a single pixel are shown in figure 6. Also, the outcome of the time domain-based fitting and the fitting in frequency domain is shown. In the time domain, the influence of the field disturbances is clearly visible by the enlarged signal decay due to the increased R_2^* values. In the frequency domain, the field disturbances cause spectral shifting, as well as peak splitting.

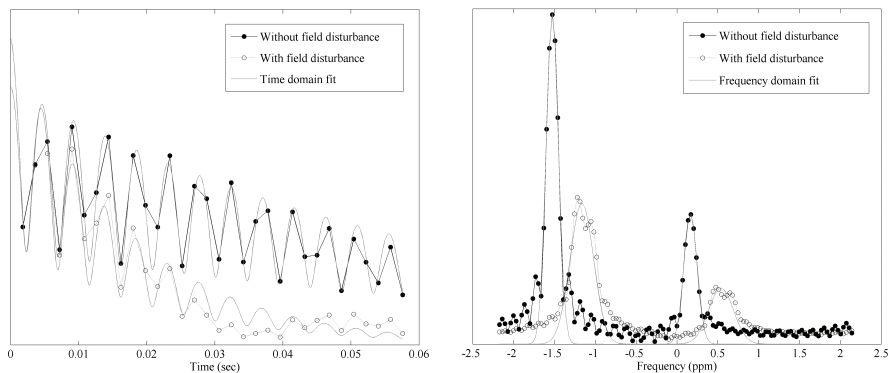


FIGURE 6 Magnitude signal in time (left) and spectrum (right) of a single pixel in the center of the EG cylinder, without (solid line, black dots) and with (dashed line, open circles) the presence of field disturbances. The outcome of the fitting procedures is shown for both the time domain-based and the frequency domain method (grey lines).

4. Heating experiment

Figure 7a shows five absolute temperature maps of the heating experiment, acquired at time points $t = 0$ sec (scan 1), $t = 40.5$ sec (scan 10), $t = 85.5$ sec (scan 20), $t = 130.5$ sec (scan 30) and $t = 175.5$ sec (scan 40). The location at which the laser fiber heats the gel is clearly visible. At the locations of the laser fiber and the two optical fibers, the average temperature over time as computed with the time domain-based mGE technique was calculated within an ROI of 7x7 pixels and plotted in figure 7b. Due to interference with the laser, no optical temperature measurements could be acquired during heating. During the last scan, the average optical fiber temperature data was $T_f = 24.6$ °C at location 1 and $T_f = 22.0$ °C at location 2. The temperature from the mGE based maps of the last scan gave $T = 24.1 \pm 0.11$ °C and $T = 22.0 \pm 0.02$ °C at the same locations.

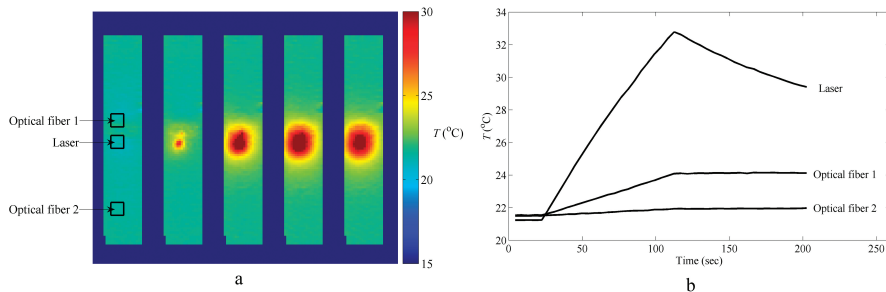


FIGURE 7 (a) Five absolute temperature maps acquired at time points $t = 0$ sec, $t = 40.5$ sec, $t = 85.5$ sec, $t = 130.5$ and $t = 175.5$ sec. In this experiment, the EG gel was locally heated with a laser fiber. In the left temperature map, the locations of the laser fiber as well as the two ROI's at the locations of the optical fibers are indicated with black squares. The average temperature over time at these locations is calculated and plotted in figure 7b. This graph shows the average absolute mGE based temperature over time at three locations in the temperature maps during the laser heating experiment. At the location of ROI 1 and 2, optical fibers were located. The average optical fiber temperature data after heating at these two locations was $T_f = 24.6$ °C at location 1 and $T_f = 22.0$ °C at location 2.

5. Ex vivo bone marrow heating experiment

In figure 8, two time domain-based (top row) and two frequency domain-based (bottom row) absolute temperature maps of the ovine bone marrow are shown, overlaid on top of the magnitude images which were acquired at $TE = 1$ msec. The left temperature maps were acquired when the bone marrow was at room temperature, and the right maps show the bone marrow-temperature after heating. The time domain-based temperature maps were acquired with starting value $\Delta f_{wf,start} = 448.6$ Hz (corresponding to 21 °C) for both the cold and warm scan. The results show that this starting can be chosen far out of range of the true temperature.

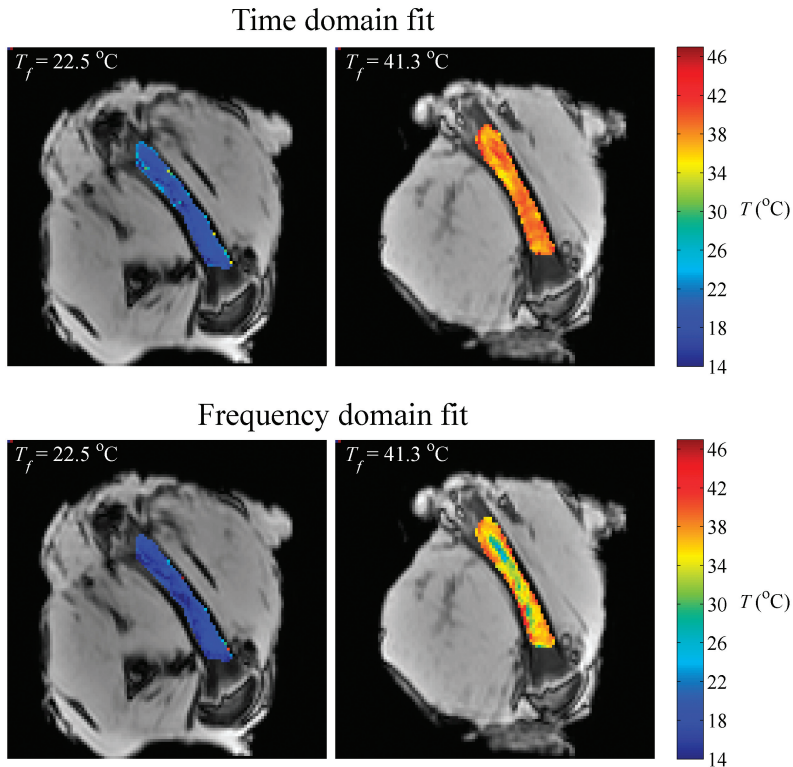


FIGURE 8 Time domain-based (top row) and frequency domain-based (bottom row) absolute temperature maps of ex vivo bone marrow, overlaid on the magnitude images acquired at TE = 1 msec. The left maps were acquired when the bone marrow was at room temperature. The right maps show the bone marrow at increased temperature.

In figure 9, the histograms of all temperature maps are depicted. The black dotted lines indicate the average optical temperature during the two scans ($T_{f,\text{scan}1} = 22.5 \text{ } ^\circ\text{C}$; $T_{f,\text{scan}2} = 41.3 \text{ } ^\circ\text{C}$). Both the time domain-based temperature and the frequency domain-based temperature were overall lower than the temperature measured with the optical fiber. At room temperature, a slightly lower temperature was found by the frequency domain fit compared to the time domain method.

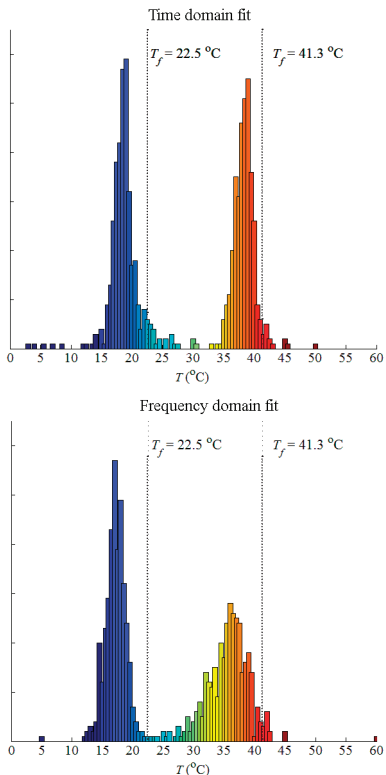


FIGURE 9 Histograms of the absolute temperature maps of the cold and warm bone marrow as shown in figure 8. The top row corresponds to the time domain-based temperature maps, the bottom row to the frequency-based maps. The dotted black lines indicate the temperature T_f as was measured with the optical fiber.

A larger spread in temperature values is seen in the frequency-based temperature map of the warm bone marrow, compared to the time domain temperature map. For better understanding of this larger spread in temperature, the signal of a single pixel taken from the warm bone marrow scan is depicted in time and frequency domain in figure 10. The output of the fitting procedures is shown by the green line. The time domain fit and frequency domain fit both detect a frequency difference. The corresponding temperature is $T = 39.31$ °C for the time domain fit and $T_{\text{freq}} = 31.96$ °C for the frequency domain fit. The oscillation frequency in the magnitude time signal is clearly visible, and can be detected by the magnitude fitting method. In the frequency domain, the water peak is somewhat indistinct, making it difficult to accurately determine its location in the spectrum.

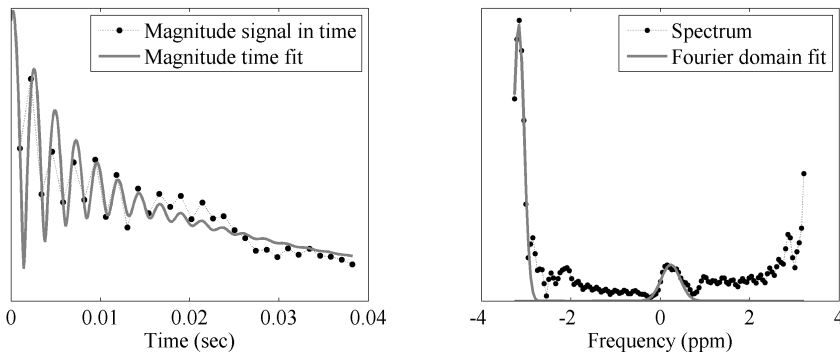


FIGURE 10 Magnitude signal in time (left) and the spectrum (right) of a single pixel's signal in warm bone marrow. The output of the fitting procedure is shown both in the time and frequency domain (grey lines).

DISCUSSION AND CONCLUSIONS

The results presented in this paper show that the multi gradient-echo sequence and subsequent time domain analysis of the resulting magnitude images allows for accurate absolute temperature mapping at high spatial as well as high temporal resolution. Absolute temperature maps of ethylene glycol at a constant temperature were acquired. In this case, the PRFS-based MRT technique would have yielded zero temperature change maps. The standard deviation found in the absolute temperature maps in the *in vitro* experiments was small and ranged between 0.04 and 0.06 °C. The mGE-based absolute temperature maps were insensitive to field drift and in the presence of local field disturbances, an overall homogeneous absolute temperature map was still obtained. In such a situation PRFS-based MRT would yield severely hampered temperature maps containing systematic errors. At the location of the field disturbance, an increase in the standard deviation was observed, but it was still relatively small: 0.14 °C. The presented mGE-based MRT technique was shown to be capable of absolute temperature mapping of a laser heating procedure in a phantom set-up.

The *ex vivo* experiments in biological tissue presented in this paper show that the magnitude-based mGE MRT technique is able to detect the resonance frequency difference Δf_{wf} between water and fat in all voxels in *ex vivo* bone marrow, at two different, constant temperatures.

We have related the performance of our method to a frequency domain technique that has repeatedly been applied in the field of mGE based MRT, which is Gaussian fitting of the magnitude spectra. Overall, our method had the same level of performance, and, moreover, showed very good results in the presence of field disturbances. In this case, the frequency-based method slightly underestimated the temperature and showed an increased standard deviation when compared to the time domain-based technique. Theoretically, all information contained in the complex time domain signal is also present in the complex frequency domain, since the Fourier transform is a linear operator. However, extracting the parameters of interest in either domain is a field of

research on its own. Furthermore, the way in which disturbances manifest themselves is very much dependent on the domain. In the *in vitro* experiment with field disturbances, peak splitting occurred in the magnitude spectra which hampered the Gaussian fitting procedure. This peak splitting, which is in all probability caused by nonlinear field gradients, can be represented by a summation of a spectrum and the same, but slightly shifted, spectrum. Through the Fourier formalism, this frequency shift manifests itself as an extra oscillating term in the time domain. The oscillation frequency of this term equals the frequency shift between the splitted peaks, and is in the order of 15 Hz, in our case. The temperature-related oscillation frequency is significantly higher, in the order of 215 Hz. In the MRT application at hand, we aim to retrieve the temperature related, high oscillating frequency component. The magnitude fit in the time domain retrieved this high oscillating frequency and appeared to be less affected by the presence of this extra low-frequency component with regard to the parameter of interest. In the *ex vivo* experiment of bone marrow at room temperature, a slightly lower temperature was found by the frequency domain fit compared to the time domain method. Furthermore, for the warm bone marrow scan, a larger spread in temperatures was observed for the frequency-based method, in comparison with the time domain method. This spread may be explained by the increased difficulty in the fitting of the water peak. The height of the water peak decreases with increasing temperature due to the temperature dependence of the longitudinal relaxation time T_1 of water. Fitting of the magnitude signal in the time domain is more successful in this situation, since it is based on retrieving the oscillation frequency of the signal, which is still clearly present in the signal from the warm bone marrow.

Techniques to reduce distortions could be developed for the frequency domain. An in depth comparison of all available post-processing techniques was, however, beyond the scope of this work. Therefore, based on the applied methods and results, it is not in place to claim general superiority of time domain analysis over frequency domain methods. We want to conclude that both techniques have advantages and drawbacks, and may be used complementarily.

In the *ex vivo* experiment, the time domain-based and the frequency domain-based method both underestimated the temperature as measured with optical fibers. A possible explanation for this effect is the fact that Eq. [3] may not be the correct model for the relation between Δf_{wf} and temperature in (bone marrow) tissue, and that the values used for α and CS may not apply exactly for this specific tissue. Temperature might not be the only factor influencing Δf_{wf} in tissue. As already mentioned by Kuroda (9), there are other parameters on which the water PRF is dependent, such as pH, magnetic ion concentration and the BOLD-effect. McDannold et al. (13) observed a large distribution of Δf between water and fat in the breast (with a standard deviation of ± 14 °C) which could not be explained by temperature variations. The reason for this effect remains unclear. Also, susceptibility effects may play a role in this. In the development of the mGE-based MRT technique for *in vivo* applications, the relation between temperature and the proton resonance frequencies of water and fat has to be examined more extensively.

The scan techniques used in this study allowed for a non-interleaved acquisition of 32 echoes, but still ensured an echo spacing which yields a broad spectral bandwidth and

CHAPTER 6

adequate spectral resolution. In this approach, strong read-out gradients were used. Using high read-out bandwidths leads to an increase of noise in the images. However, in our opinion, using strong read-out gradients is of great importance in mGE-based MRT, due to the fact that they result in small chemical shift artifacts. This is essential since the absolute temperature is derived per voxel, based on the frequency difference between two resonances present within that same voxel. Furthermore, the use of high read-out bandwidths will reduce geometric distortions due to susceptibility effects.

An elegant feature of fitting the magnitude signal in the time domain is the fact that just a single post-processing step is needed, from which $\Delta f(T)$ is a direct output parameter. No extra post-processing steps such as windowing were taken prior to the fitting. The fitting procedure was extremely tolerant regarding the starting values chosen for Δf , as was seen in the *in vitro* and *ex vivo* experiments, where all temperature maps were acquired using a value for Δf_{start} which corresponded to 21 °C. This is an important beneficial property, since, during a thermal intervention, the fitting procedure has to yield the correct temperature without detailed prior knowledge on the current temperature distribution.

All post-processing in this work was performed off-line. Currently, the computation time needed for the fitting procedure is the limiting factor for real-time mGE-based MRT. When comparing the computation time of the time domain-based fitting procedure to that of the frequency domain technique, a very small difference is seen in case of the *in vitro* experiments, where the average computation time per pixel was 0.10 seconds for the time domain fit versus 0.09 seconds for the frequency domain fit. In the *ex vivo* maps, this difference was larger: the average computation time per pixel was 0.31 seconds for the time domain fit versus 0.10 seconds for the frequency domain fit. The increased complexity of the signal is most likely the cause of this. The fitting software used in this work was not optimized for this specific application; computation time can be significantly decreased by development of a dedicated fitting tool. Decreasing the number of fit parameters may also allow for a faster procedure.

The echo times used in PRFS-based MRT are relatively long. Values in the order of the T_2^* of the tissue ($TE \geq 20$ msec) are chosen, to maximize the signal-to-noise ratio (SNR) of the temperature maps (19). The mGE technique with its short echo spacing and multiple echo acquisition can be regarded as a technique which extends the PRFS-based method. Theoretically, it can measure absolute temperature T in voxels containing both temperature independent and temperature dependent spectral resonances, as well as temperature changes ΔT in all voxels containing merely temperature dependent resonances. In such combined temperature measurement technique, local absolute temperature information may be used to calibrate nearby relative temperature measurements.

ABSOLUTE MRT USING TIME DOMAIN ANALYSIS OF mGE MAGNITUDE IMAGES

REFERENCES

1. Wlodarczyk W, Hentschel M, Wust P, Noeske R, Hosten N, Rinneberg H, Felix R. Comparison of four magnetic resonance methods for mapping small temperature changes. *PhysMedBiol* 1999;44(2):607-624.
2. Hindman JC. Proton Resonance Shift of Water in the Gas and Liquid States. *Journal of Chemical Physics* 1966;44(12):4582-4592.
3. Sapareto SA, Dewey WC. Thermal dose determination in cancer therapy. *Int J Radiat Oncol Biol Phys* 1984;10(6):787-800.
4. Peters NH, Bartels LW, Sprinkhuizen SM, Vincken KL, Bakker CJ. Do respiration and cardiac motion induce magnetic field fluctuations in the breast and are there implications for MR thermometry? *J Magn Reson Imaging* 2009;29(3):731-735.
5. Stollberger R, Ascher PW, Huber D, Renhart W, Radner H, Ebner F. Temperature monitoring of interstitial thermal tissue coagulation using MR phase images 2. *JMagn ResonImaging* 1998;8(1):188-196.
6. Kuroda K, Kokuryo D, Kumamoto E, Suzuki K, Matsuoka Y, Keserci B. Optimization of self-reference thermometry using complex field estimation. *Magn Reson Med* 2006;56(4):835-843.
7. Rieke V, Vigen KK, Sommer G, Daniel BL, Pauly JM, Butts K. Referenceless PRF shift thermometry. *Magn ResonMed* 2004;51(6):1223-1231.
8. Kuroda K, Suzuki Y, Ishihara Y, Okamoto K. Temperature mapping using water proton chemical shift obtained with 3D-MRSI: feasibility in vivo. *Magn ResonMed* 1996;35(1):20-29.
9. Kuroda K. Non-invasive MR thermography using the water proton chemical shift 1. *IntJHyperthermia* 2005;21(6):547-560.
10. Kuroda K, Takei N, Mulkern RV, Oshio K, Nakai T, Okada T, Matsumura A, Yanaka K, Hynynen K, Jolesz FA. Feasibility of internally referenced brain temperature imaging with a metabolite signal. *Magn Reson Med Sci* 2003;2(1):17-22.
11. Mansfield P. Spatial mapping of the chemical shift in NMR. *Magn Reson Med* 1984;1(3):370-386.
12. Kuroda K, Mulkern RV, Oshio K, Panych LP, Nakai T, Moriya T, Okuda S, Hynynen K, Jolesz FA. Temperature mapping using the water proton chemical shift: self-referenced method with echo-planar spectroscopic imaging. *Magn ResonMed* 2000;43(2):220-225.
13. McDannold N, Barnes AS, Rybicki FJ, Oshio K, Chen NK, Hynynen K, Mulkern RV. Temperature mapping considerations in the breast with line scan echo planar spectroscopic imaging. *Magn Reson Med* 2007;58(6):1117-1123.
14. McDannold N, Hynynen K, Oshio K, Mulkern RV. Temperature monitoring with line scan echo planar spectroscopic imaging 39. *MedPhys* 2001;28(3):346-355.
15. Mulkern RV, Panych LP, McDannold NJ, Jolesz FA, Hynynen K. Tissue temperature monitoring with multiple gradient-echo imaging sequences. *J Magn Reson Imaging* 1998;8(2):493-502.
16. Taylor BA, Hwang KP, Elliott AM, Shetty A, Hazle JD, Stafford RJ. Dynamic chemical shift imaging for image-guided thermal therapy: analysis of feasibility

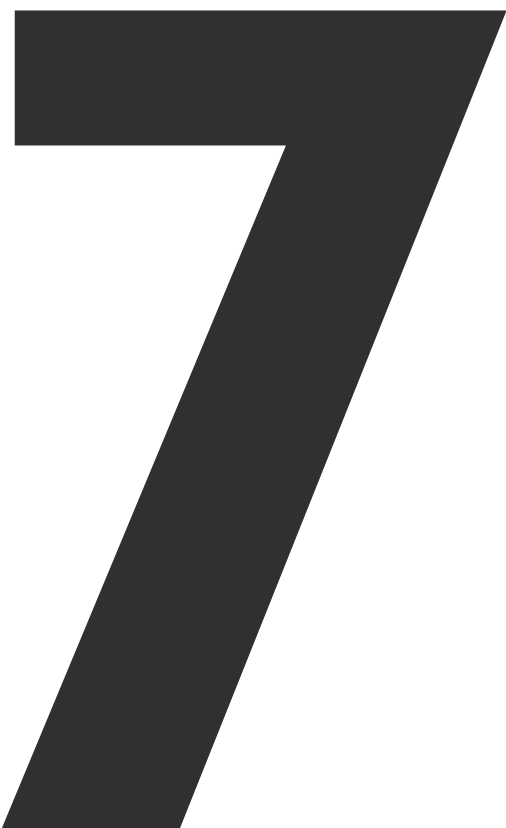
ABSOLUTE MRT USING TIME DOMAIN ANALYSIS OF mGE MAGNITUDE IMAGES

- and potential. *Med Phys* 2008;35(2):793-803.
- 17.** Wehrli FW, Ford JC, Attie M, Kressel HY, Kaplan FS. Trabecular structure: preliminary application of MR interferometry. *Radiology* 1991;179(3):615-621.
 - 18.** Amman C, Meier P, Merbach A. A simple multinuclear NMR thermometer. *J Magn Reson* 1982;46(2):319–321.
 - 19.** de Zwart JA, van Gelderen P, Kelly DJ, Moonen CT. Fast magnetic-resonance temperature imaging. *J Magn Reson B* 1996;112(1):86-90.



THE MAIN FOCUS OF THE PREVIOUS CHAPTER WAS ON THE POST-PROCESSING OF ACQUIRED MR SIGNALS INTO TEMPERATURE INFORMATION. POST-PROCESSING PROCEDURES ARE BASED ON CERTAIN ASSUMPTIONS WITH REGARD TO THE ACQUIRED SIGNAL. WHEN THE UNDERLYING ASSUMPTIONS ARE INCORRECT, THE POST-PROCESSING WILL LEAD TO ERRONEOUS RESULTS. THE NEXT CHAPTER IS CONCERNED WITH A SPECIFIC SITUATION IN WHICH THE ASSUMED PROPERTIES OF THE ACQUIRED SIGNAL ARE INCORRECT. IT WILL BE SHOWN THAT STATIC BACKGROUND FIELD GRADIENTS ALTER THE EFFECTIVE ECHO TIME IN GRADIENT-ECHO ACQUISITIONS, WHICH INDUCES TEMPERATURE ERRORS IN PRFS-BASED AND MGE-BASED MR THERMOMETRY





STATIC FIELD INHOMOGENEITY AS A SOURCE OF ERRORS IN PRFS-BASED AND MGE-BASED MR THERMOMETRY

INTRODUCTION

MR thermometry (MRT) techniques can be used for guidance of thermal therapy. The temperature dependence of the proton resonance frequency (PRF) of water is commonly exploited for this purpose, because of its linear dependence on temperature (1) and its tissue type independence (2). Different MR techniques have been developed to extract temperature information from the PRF changes. The currently most employed method for monitoring PRF changes, and hence temperature changes, is proton resonance frequency shift (PRFS)-based MRT. It is based on the subtraction of gradient-echo phase images to eliminate static field inhomogeneities. Another MRT technique has been proposed which is insensitive to temporal field disturbances and allows for absolute thermometry (3-8). It is based on a multi gradient-echo (mGE) sequence (9). The mGE-based MRT technique exploits the frequency difference Δf between a temperature sensitive PRF (e.g. of water) and a temperature insensitive reference PRF (e.g. of fat). Theoretically, it is insensitive to static field inhomogeneities due to the fact that the PRF of both resonances will be equally affected by such field disturbances but their Δf will remain unaffected up to a very high level of precision.

MRT techniques that are based on the temperature dependence of the PRF are thus generally considered to be insensitive to static field inhomogeneities, because they either employ subtraction of successive phase images (PRFS-based MRT) or use an internal temperature-independent reference component (mGE-based MRT). There is reason to doubt whether the assumed immunity of the PRFS-based and mGE-based MRT technique for static field inhomogeneities is correct. Both techniques employ gradient-echo sequences, which are known to be sensitive to static field inhomogeneities (10).

In this work we will show that MR thermometry measurements are most certainly affected by the presence of static background field gradients and in particular by background gradients that are aligned with the read-out gradient. First, a theoretical analysis of the influence of static field inhomogeneities on gradient-echo sequences in general, and on MR thermometry techniques in particular, will be presented. Furthermore, it

will be shown by phantom experiments that background gradients alter the effective echo time which induces temperature errors in PRFS-based and mGE-based MR thermometry. The impact of static background gradients on MRT *in vivo* was assessed by static field gradient mapping in the breasts of a volunteer.

THEORY

Static field inhomogeneities can be modeled in terms of a local background gradient G' (which is the linearization over a voxel of the component of the background gradient along a certain direction) plus a local field offset ΔB . Gradient-echo sequences are sensitive to the presence of background gradients G' (10). Background gradients lead to shifts of the sampled data in k-space. The specific influence the background gradients have on the resulting image depends on their alignment and relative strength with respect to the imaging gradients. When G' has a component along the slice selection direction, it leads to section distortions and dephasing of the spins. In the phase encoding direction, G' causes dephasing of the spins, which leads to signal losses. When G' has a component along the read-out direction, two distinct effects take place: it leads to image distortions since it alters the effective frequency encoding gradient. In addition, temporal echo shifts occur because the effective dephasing and rephasing lobes of the read-out gradient are decreased or increased, depending on the sign of G' with respect G_R (Fig. 1).

The reduction of image distortions and signal dephasing (especially in case of G' in the slice selection direction) has been the major focus of studies regarding the influence of background gradients (11-13). In the current work, we focus more specifically on background gradient-related effects that may be of influence in MR thermometry sequences. We investigated the influence of background gradients which have a component along the read-out direction on the performance of PRFS-based and mGE-based MR thermometry.

Image distortions

In the presence of a local background gradient in the read-out direction, image distortions occur because the effective frequency encoding gradient is altered. For a local background gradient G'_R (which is the linearization over a voxel of the component of G' along the read-out direction) and a local field offset ΔB , the spins at position x in a small interval $x_1 < x < x_2$ will be observed at a position x' parallel to the read direction, according to:

$$x' = x + (x - x_0) \frac{G'_R}{G_R} + \frac{\Delta B}{G_R} \quad [1]$$

where $x_0 = (x_1 + x_2)/2$. The local gradient $G'_R(x_0)$ leads to a locally compressed or expanded version of the true spin density, whereas the field offset $\Delta B(x_0)$ leads to a shift of the spin density.

Temporal echo shift

In either direction, the coverage errors in k-space due to the presence of G' can be referred to as echo shifts. In the current work, we investigated a specific echo shift, the temporal echo shift, which occurs only when the background gradient is aligned with the read-out gradient. Temporal echo shifting occurs because the effective dephasing and rephasing lobes of the read-out gradient are decreased or increased, depending on the sign of G'_R with respect to G_R (Fig. 1).

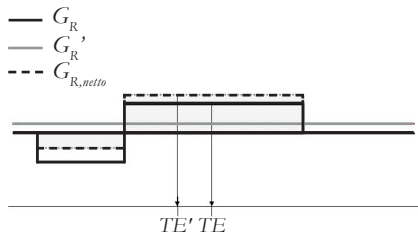


FIGURE 1 The influence of G' (red line) on the read-out gradient lobe is shown. In this case, the echo time TE is shifted to an earlier time point TE' due to the presence of a background gradient with the same polarity as the read-out gradient.

The echo occurs at an earlier or later time point than the echo time as set by the user. The shifted echo time TE' depends on the chosen echo time TE , and the strength and sign of $G'_R(x)$ at a certain location and of the rephasing read-out gradient lobe G_R (local field offsets ΔB do not affect the echo time):

$$TE'(x) = \frac{TE}{\frac{G'_R(x)}{G_R} + 1} \quad [2]$$

Note the asymmetry around $G'_R = 0$, indicating the influence of the polarity of G'_R with respect to G_R on the actual TE' .

Influence of G'_R on MR thermometry

As can be seen in Eq. 1 and 2, the relative strength and polarity of G'_R versus G_R determine the magnitude of the image distortions and temporal echo shifts. The influence of a given G'_R thus depends on the imaging parameters and differs for PRFS-based and mGE-based MRT techniques.

PRFS-based MRT

The ideal echo time for PRFS-based MRT equals the T_2^* of the tissue (14). This favors to relatively long echo times (~ 20 msec) which allow for the use of weak read-out gradients for increased SNR. However, as can be seen in Eq. 1 and 2, sequences which employ weak read-out gradients are more susceptible to distortions and temporal echo

CHAPTER 7

shifting due to static field inhomogeneities.

In PRFS-based MRT, the temperature change ΔT in between two scans is calculated from the phase change $\Delta\varphi$ between the scans using:

$$\Delta T = \frac{\Delta\varphi}{\alpha \gamma B_0 TE} \quad [3]$$

with α the temperature dependence of the electron screening constant of water ($d\sigma_{\text{water}}/dT = 0.01 \text{ ppm}/^\circ\text{C}$), γ the gyromagnetic ratio, B_0 the main magnetic field and TE the echo time.

On top of acquisition-related (due to the finite and discrete sampling in MRI) and image distortion-related phase errors in $\Delta\varphi$, temporal echo shifting leads to problems in PRFS-based MR thermometry, since it violates the assumption that the signal is centered with respect to TE . However, the echo time will be shifted in the presence of G' , and therefore, in the computation of temperature from phase information, an temperature error $\varepsilon_{\Delta T}$ is introduced in ΔT :

$$\varepsilon_{\Delta T} = \Delta T - \Delta T_{\text{act}} = \frac{\Delta\varphi}{\alpha \gamma B_0 TE} \left(1 - \frac{TE}{TE'} \right) = \Delta T \left(1 - \frac{TE}{TE'} \right) \quad [4]$$

where ΔT_{act} is the temperature change which is computed from $\Delta\varphi$ using the actual, shifted, echo time TE' . The temperature error $\varepsilon_{\Delta T}$ is echo time independent.

mGE-based MRT

In mGE MRT, multiple (n) gradient-echo images are acquired at echo times $TE_i = TE_1 + (i-1) \cdot \Delta TE$ for $i = 1, 2, \dots, n$, with TE_1 the echo time of the first gradient-echo image and ΔTE the echo spacing. This yields a discretely sampled time signal containing spectral information of the substances involved, from which information on the proton resonance frequency can be extracted (3-8). It allows for absolute thermometry by relating the frequency difference Δf between a temperature sensitive PRF (e.g. of water) and a temperature insensitive reference PRF (e.g. of fat) in a voxel to temperature.

Strong readout gradients ($> 20 \text{ mT/m}$) are employed in mGE-based MRT, to acquire the signal at sufficiently short echo spacing. Sequences which employ strong gradients are less sensitive to background gradients (Eq. 1 and 2). The contributions of image distortions in mGE-based MRT will be negligible for background gradients of the order 0.1 mT/m . The temporal echo shifts are small for mGE sequences, but may, nevertheless, affect the outcome of this technique. The analysis of the acquired signals is based on the assumption that the signal is acquired at certain echo times. In case of temporal echo shifting, this assumption is not valid.

To illustrate the influence of temporal echo shifting on mGE-based MRT, the MR signal of a water and fat containing voxel is shown for both the acquired (shifted) echo times TE'_i and the assumed (preset) echo times TE_i , in time and frequency domain in figure 2 ($B_0 = 1.5 \text{ T}$, $\Delta f_{\text{water-fat}} = 3.4 \text{ ppm}$). The altered temporal and spectral character-

STATIC FIELD INHOMOGENEITY AS A SOURCE OF ERRORS IN MRT

istics can be appreciated as an increase in the oscillation frequency in the time domain, and as a shift of the fat resonance peak in the frequency domain.

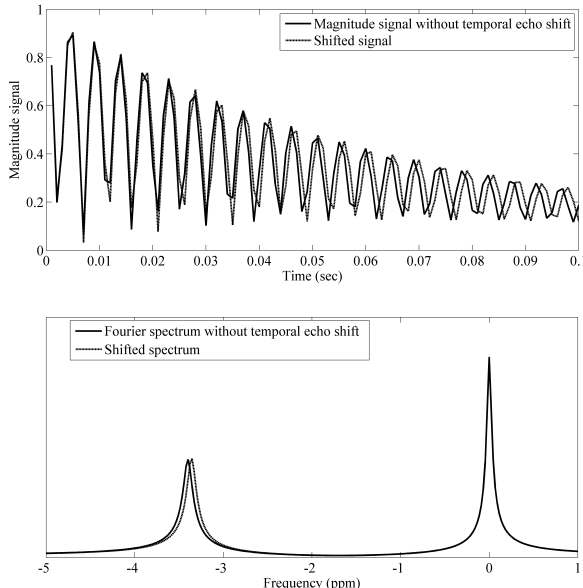


FIGURE 2 The theoretical signal (solid line) and the shifted signal (dashed line) are shown both in time (top) and frequency (bottom) domain. In this calculation, $G_R = 12 \text{ mT/m}$, $G' = 0.15 \text{ mT/m}$ (ratio = 0.0125). The altered spectral characteristics can be appreciated as an increase of the oscillation frequency in the time domain, and as a shift of the fat resonance peak in the frequency domain (indicated by the arrows). The error in Δf is $\varepsilon_{\Delta f} = -0.042 \text{ ppm}$, corresponding to a temperature overestimation of $+4.20^\circ \text{C}$.

The influence of temporal echo shifts can also be shown by substitution of TE_i by TE'_i in the modulus signal equation of a voxel containing two spectral components 1 and 2:

$$S(TE'_i) = \sqrt{A_1^2 e^{-2R_{2,1}^* TE'_i} + A_2^2 e^{-2R_{2,2}^* TE'_i} + 2A_1 A_2 e^{-(R_{2,1}^* + R_{2,2}^*) TE'_i} \cos(2\pi\Delta f_{12} TE'_i + \Delta\phi_{12})} \quad [5]$$

where A_1 and A_2 the effective spin densities (including effects of the longitudinal relaxation rate T_1), $R_{2,1}^*$ and $R_{2,2}^*$ the effective transverse relaxation rates, and $\Delta\phi_{12}$ the phase offset difference between the two components in radians. The error in the perceived frequency difference Δf_{12} becomes apparent from this equation. The observed frequency difference Δf_{12} is not equal to the actual frequency difference Δf_{act} ; $\Delta f_{12} = \Delta f_{act} \cdot TE'/TE$. The error in the frequency difference is given by $\varepsilon_{\Delta f} = \Delta f_{12} - \Delta f_{act}$ and scales with TE'/TE :

$$\varepsilon_{\Delta f} = \Delta f_{act} \left(\frac{TE'}{TE} - 1 \right) \quad [6]$$

METHODS

Influence of G_R' on PRFS-based MRT

Heating experiments were conducted to study the influence of G_R' on PRFS-based MR temperature measurements. A gel phantom (2% agar, 1% silica) was used. The gel was shaped as a flat cylinder (height 5 cm, radius 6 cm). The phantom was placed with its longitudinal axis perpendicular to the main magnetic field. The shape and orientation were chosen because it causes a considerable G_R' in the phantom and leads to a range of G_R' values within the phantom. The temperature change was achieved inside the phantom by locally heating it using a 256 elements phased-array High Intensity Focused Ultrasound (HIFU) transducer, embedded in a 1.5 T clinical whole body MR scanner (Sonaleve, Philips Healthcare, Helsinki, Finland). A continuous ultrasound pulse of 30 Watt was applied for 60 seconds.

As shown by Eq. 1 and 2, the ratio G_R'/G_R influences the magnitude of the temperature errors. Therefore, two MRT sequences were thus applied, each with a different value for the read-out gradient strength, to vary the G_R'/G_R ratio. The first scan employed a strong G_R ($G_R = 12.8 \text{ mT/m}$), and the second scan used a much weaker G_R ($G_R = 0.5 \text{ mT/m}$). The image distortions and temporal echo shifts both manifest in the read-out direction, which was set to Feet-Head (FH). For both PRFS-based MRT sequences, controlled heating was applied at three different locations in the gel along the FH-axis (in order to vary the influence of G_R') leading to a total of six heating experiments. Other scan parameters were: $TR = 80 \text{ msec}$, $\alpha = 25^\circ$; $TE = 15 \text{ msec}$; $FOV = 160 \times 160 \text{ mm}^2$; voxel size = $2 \times 2 \times 6 \text{ mm}^3$; number of dynamics = 60. Temperature maps were computed using Eq. 3.

The next step was the computation of the expected temperature errors at the same three heating locations due to image distortions and temporal echo shifting, based on the theory. This requires the background gradient strength at the three heating locations in the gel. A field gradient map of the phantom was therefore computed. It was based on phase images (calculated from reconstructed real and imaginary images) which were acquired at two echo times ($TE_1 = 10 \text{ msec}$, $TE_2 = 15 \text{ msec}$). The read-out gradient was maximized to minimize the influence of the static field background gradients in the phase images ($G_R = 19.6 \text{ mT/m}$). A derivative map of each phase image was taken in the FH direction. To eliminate B1 inhomogeneities, the field gradient map was computed by subtraction of the two derivative maps. This gradient field map was used to determine the local G_R' at the three heating locations. The G_R' values were used to compute the expected temperature errors at the same locations due to image distortions and temporal echo shifting. For this computation, a 1D uniform spin density distribution was modeled. The static magnetic field inhomogeneities experienced by water protons at location x of the 1D spin distribution are determined by the local macroscopic field and the local temperature dependent chemical shift and is given by:

$$\delta B(x) = G' \cdot x + B_0 \alpha \Delta T_{\max} e^{-(x-x_0)^2/s^2} \quad [7]$$

where the first term represents the local field gradient and the second term describes the field changes due to a gaussian temperature profile with a maximum temperature change of ΔT_{\max} . Local field offsets ΔB were set to zero and it is assumed that the temperature distribution itself does not affect the macroscopic field. The 1D discrete, distorted phase change profile $\Delta\varphi$ was computed by taking the inverse Fourier transform of the k-space representation of the complex spin density. Finally, $\Delta\varphi$ was translated into temperature change profiles for all experimentally found G_R' values, using Eq. 3.

Influence of G_R' on mGE-based MRT

In vitro mGE-based MRT scans were performed on a 3-T whole body system (Achieva, Philips, Best, The Netherlands). G_R' was deliberately maximized by the shape of the phantom which was a flat cylinder (length 4 cm, radius 4.5 cm), placed with its longitudinal axis perpendicular to the main magnetic field. In contrast to PRFS-based MRT, no temperature changes are required for temperature errors to occur due to temporal echo shifting in mGE-based MRT. The cylinder was filled with ethylene glycol (EG) at constant temperature and with a homogeneous temperature distribution. Ethylene glycol was used as a test fluid for all scans, since the temperature dependence of the frequency difference Δf_{hm} between the hydroxyl (h) and methylene (m) group in EG is well known (15):

$$T_{EG} [^{\circ}\text{C}] = 193.35 - 102 \cdot 10^6 \cdot \Delta f_{hm} [\text{Hz}] / \gamma B_0 \quad [8]$$

with B_0 the main magnetic field strength. The EG temperature T_{EG} was measured during all scans using fiber-optic temperature probes (Luxtron, Santa Clara, CA) which were placed in the EG through the top of the cylinder.

As shown in Eq. 2, the amount of temporal echo-shift depends on the echo time, on the alignment of G_R with respect to G_R' , and on their relative strengths. In our set-up, the strength and direction of G_R' were determined by the phantom's shape and material and orientation with respect to B_0 . The strength of the read-out gradient was kept constant for all scans: $G_R = 27.1 \text{ mT/m}$. The direction of G_R (dir) was changed per scan. In this way, the impact of changes in the ratio G_R'/G_R on the mGE temperature maps could be visualized. Four mGE scans were acquired: 1. dir = Feet-Head (FH) 2. dir = Head-Feet (HF) 3. dir = Right-Left (RL) 4. dir = Left-Right (LR).

In our setup, with $B_0 = 3\text{T}$ and T_{EG} at room temperature ($\sim 21 \text{ }^{\circ}\text{C}$), the resonance frequency difference $\Delta f_{hm} \approx 215 \text{ Hz}$. To satisfy Nyquist, the echo times were therefore chosen to be: $TE_1 = 1.8 \text{ msec}$, $\Delta TE = 1.8 \text{ msec}$, which corresponds to a spectral bandwidth $SBW \approx 555 \text{ Hz}$. A total of 32 echoes was acquired and asymmetric read-out was performed using rewinder gradients. The other MR parameters were: $TR = 60 \text{ msec}$; $\alpha = 30^\circ$; $FOV = 128 \times 128 \text{ mm}^2$; acquired matrix 84×84 ; acquired voxel size $1.52 \times 1.52 \times 10 \text{ mm}^3$; reconstructed matrix 96×96 . For all four scans, Δf_{hm} was found by fitting the magnitude signal in the time domain to the signal model in Eq. 6 using the echo times without shift (7). Subsequently, absolute temperature maps were computed using Eq. 8.

Furthermore, to assess what temperature errors could be expected based on the theory of temporal echo shift, absolute temperature maps were computed based on the back-

ground gradient maps, Eq. 2 and:

$$T_{EG} = 193.35 - 102 \cdot 10^6 \Delta f_{act} \left(\frac{TE'}{TE} \right) / \gamma B_0 \quad [9]$$

with $\Delta f_{act} = 215$ Hz.

Background gradient quantification in the human breast

The spatial characteristics of static field inhomogeneities in the human breast were studied. A healthy volunteer (age 25) was placed in prone position in a 3-T whole body system (Achieva, Philips, Best, The Netherlands). To eliminate time varying, respiration-induced field disturbances (16), all scans were acquired during breath-hold. Single slice gradient-echo scans were acquired in the transverse, sagittal and coronal plane. Prior to data collection, the clinical protocol with regard to shimming at 3-T was performed: first order shimming was applied to a volume covering either both breasts (for the transverse and coronal acquisition) or a single breast (for the sagittal acquisition). It was assured that the heart was excluded from the shimming volume. Six echoes were acquired with an interval of 2.3 msec and the first echo time was $TE = 2.3$ msec. The echo times were set to a multiple of 2.3 msec to yield in-phase water and fat signals. The read-out gradient was maximized to minimize the influence of the static field background gradients ($G_R = 27$ mT/m). The other scan parameters were: $TR = 50$ msec, acquired voxel size = $2 \times 2 \times 8$ mm³, field-of-view (FOV) = 144×144 mm², number of averages = 2, total scan duration = 14.7 sec.

The spatial distribution of the field gradients in the breast was obtained from the acquired phase images which were calculated from the reconstructed real and imaginary images. Prior to the analysis, the phase images were unwrapped manually by in-house developed software. A field map was calculated for each echo using: $\Delta B = \varphi / \gamma TE$. Subsequently, two in-plane field gradient images were obtained for each of the field maps by application of the forward difference operator along both image axes. To eliminate B_1 inhomogeneity influences in the final field gradient map, the field gradient maps of the first and fourth echo were subtracted. Subsequently, gaussian blurring was applied (sigma = 1 voxel). To facilitate comparison between the background field gradients and the read-out gradients, the in-plane background gradient maps were expressed in mT/m. To evaluate the spatial variations of the background gradients within the breast, histograms were calculated per scan orientation for both gradient directions after manual segmentation of the breast based on the magnitude images.

RESULTS

Influence of G_R on PRFS-based MRT

Figure 3 shows the PRFS-based MR temperature maps of the HIFU heating experiments, overlaid on top of the magnitude image acquired at the first echo time. The top row shows the temperature maps which were acquired with $G_R = 12.85$ mT/m, and the low SNR due to the strong G_R can be seen. The temperature maps in the bottom row were acquired with $G_R = 0.51$ mT/m. The higher SNR and image distortions due to the weak read-out gradient are visible. Temperature profiles over time, shown in the right two graphs, were computed by averaging the temperature within a region of interest (ROI) of 2x2 voxels, located in the center of the thermal spot. The experiments which used $G_R = 0.51$ mT/m show a strong location-dependent difference in the measured temperature change for the same heating duration and power. When a stronger read-out gradient is used, the measured temperature difference over time does not differ as much between the three locations.

It was assessed whether the position-dependence of the measured temperature in the $G_R = 0.51$ mT/m experiment could be expected based on the presence of a background gradient.

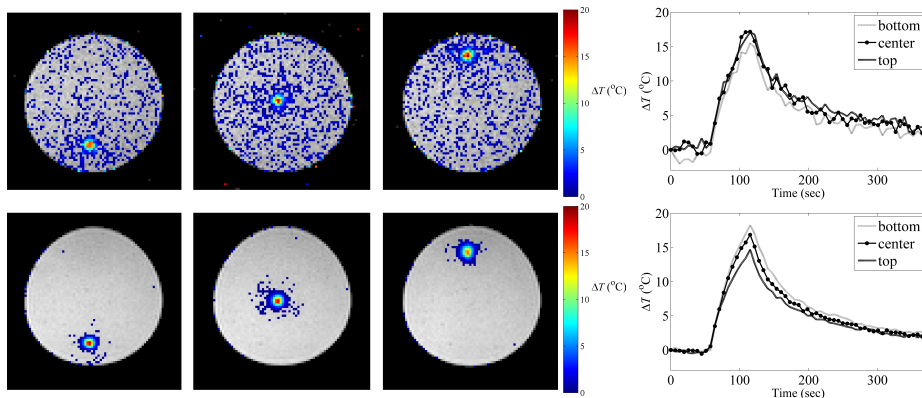


FIGURE 3 Temperature change maps overlaid on magnitude image of a phantom during HIFU heating. Top row: acquired with $G_R = 12.85$ mT/m Bottom row: acquired with $G_R = 0.51$ mT/m. The temporal temperature behaviour for three thermal spots are shown on the right for both read-out gradient strengths.

The background gradient strength at the three heating locations was determined from the field gradient map of the phantom (Fig. 4): +0.08 mT/m at the ‘top’ (positive z-direction), 0 mT/m in the center and -0.08 mT/m at the ‘bottom’ of the phantom (negative z-direction). Since the central heating position did not suffer from field gradient errors, the measured temperature change from a single pixel at that location was taken as the actual temperature change ($\Delta T_{act} = 18$ °C).

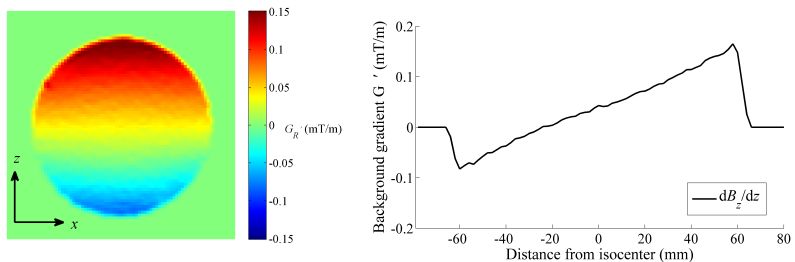


FIGURE 4 Background field gradient map (left) and profile over the FH-axis (right) of the phantom set-up used in the PRFS-based MRT experiment (fig. 3).

The theoretical temperature profiles for the other two heating locations were determined and compared to the experimental temperature profiles, as shown in Figure 5. In the graphs, the red lines depict the temperature errors in relation to the ‘unaffected’ temperature profile of the central heating location. The theoretical temperature profiles quite accurately match the measured temperature profiles, supporting the hypothesis that background gradients affect the outcome of PRFS-based MRT.

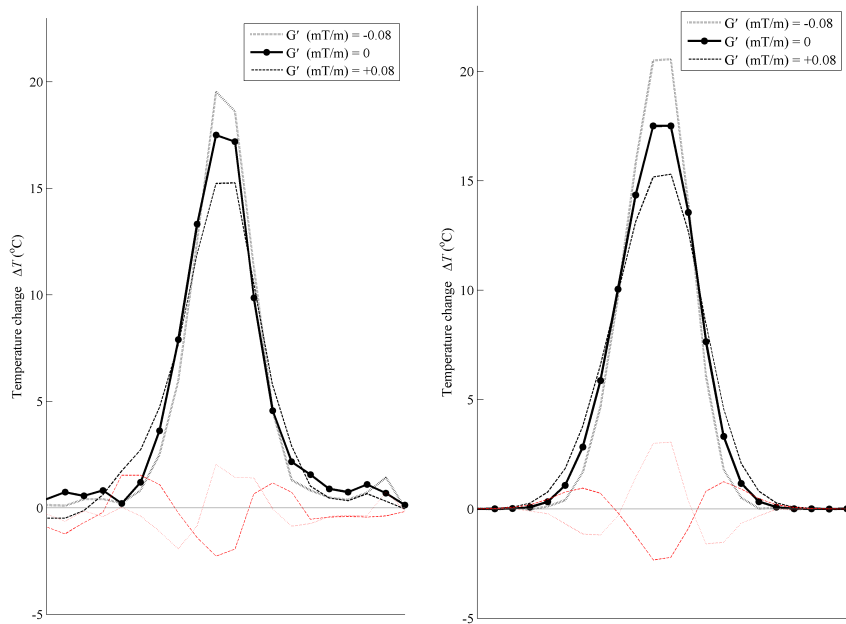


FIGURE 5 Experimental (left) and simulated (right) temperature profiles (in HF-direction) of sonifications at three different locations (e.g. for three different G' strengths) in the phantom. The temperature errors with respect to the ‘unaffected’ temperature profile ($G' = 0$) are shown in red.

Influence of G_R' on mGE-based MRT

Four absolute temperature maps of EG at four different readout directions are shown in Fig. 6. The direction of G_R is indicated by the arrow. An apparent temperature gradient in the direction of G_R is visible.

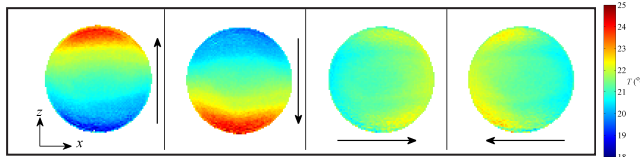


FIGURE 6 Absolute temperature maps of EG fluid at constant, homogeneous temperature ($T_{EG} = 21.18 \pm 0.15^\circ\text{C}$, optical fiber). The temperature maps all show an apparent temperature gradient in the direction of G_R (which is indicated by the black arrow).

The temperature range and average temperature T_{av} per scan is: **1.** 17.9-24.5 °C ($T_{av} = 21.3^\circ\text{C}$) **2.** 19.2-24.8 °C ($T_{av} = 21.5^\circ\text{C}$) **3.** 20.1-22.6 °C ($T_{av} = 21.4^\circ\text{C}$) **4.** 19.9-23.2 °C ($T_{av} = 21.4^\circ\text{C}$). The optical temperature measurements gave $T_{EG} = 21.2 \pm 0.15^\circ\text{C}$ during all scans.

Figure 7 shows two background gradient maps of the phantom, in the FH and LR direction. From the maps, the difference in G_R' in the FH and LR direction can be appreciated: there is a stronger background gradient present in the FH direction, resulting in the larger temperature errors in the mGE-based temperature maps with the read-out gradient aligned with the FH axis.

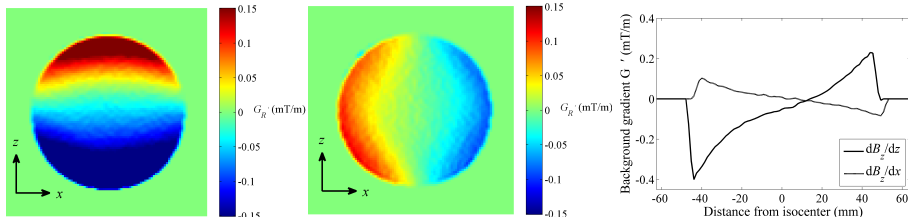


FIGURE 7 Two background field gradient maps of the phantom used in the mGE-based experiments, one in FH (left map, solid line in graph) and one in LR (right map, dotted line in graph) direction. G_R' is nonlinear and has maximum strength in the FH direction.

It was assessed whether the temperature errors in the mGE-based MRT maps can be explained by temporal echo shifting. Theoretically expected temperature maps were computed using Eq. 9 and the background gradient maps, and are shown in figure 8.

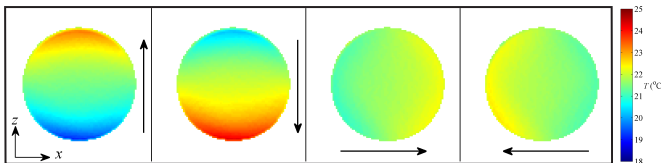


FIGURE 8 Theoretical absolute temperature maps, based on the background gradient maps shown in Fig. 7 and Eq. 9.

The theoretical temperature maps predict somewhat smaller temperature errors at the edges of the phantom, especially for the maps with the read-out in the FH direction (left two maps). At those locations, the experimental temperature maps suffer from low SNR, leading to slight differences between expected and measured temperatures. In addition, the in-plane gradient may have varied over the slice, which was relatively thick. Overall, the patterns of the experimental and theoretical temperature maps are similar, indicating that the errors can be largely explained by temporal echo shifting effects.

Background gradient quantification in the human breast

Figure 9 shows static background field gradient maps in the human breast for three orthogonal imaging directions over both in-plane axes. The magnitude of the background gradients varies spatially in the breast and were found to range between -0.10 and +0.10 mT/m at 3 Tesla. In the center of the breasts, the overall values for the background field gradients were ranging between -0.04 and 0.04 mT/m, except for the sagittal field map gradient in the z-direction, where higher values for G' were found in a large part of the center of the breast.

The influence of such background gradients depends on their relation with the imaging gradients. Per scan orientation, differences between the two in-plane gradient directions are observed in the field gradients maps. This implies that the choice of the read-out gradient direction is of importance during MR thermometry in the breast. For example, in the sagittal plane, the read-out gradient should preferably set to be Head-Feet (or Feet-Head) instead of Anterior-Posterior (AP) to minimize the influence of the background gradients.

DISCUSSION AND CONCLUSIONS

In this work we have shown that static field gradients may lead to errors in MR thermometry. The influence of G_R' on PRFS-based MRT was shown in heating experiments. A relation between the presence of G_R' and the measured temperature change was observed. Through simulations, it was shown that G_R' accounted for this effect through image distortions and temporal echo shifting.

In mGE-based MRT, errors of over 3 °C in the absolute temperature maps of ethylene glycol were observed with the ethylene glycol being at constant temperature. This was largely explained by the presence of G_R' ; but indications remained that other background gradient effects may be involved as well.

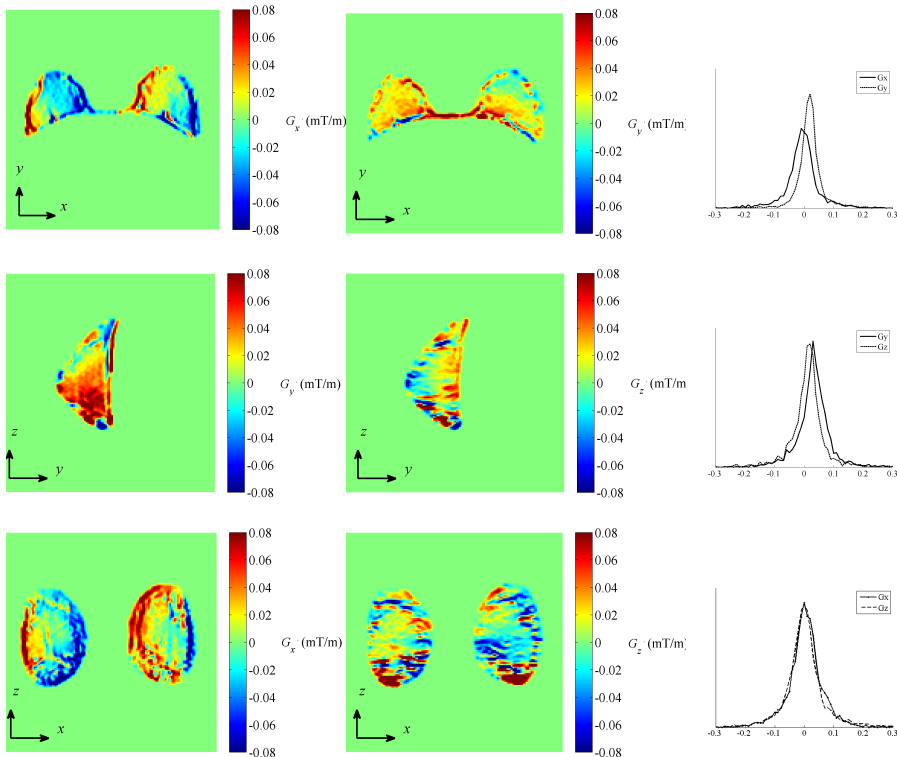


FIGURE 9 Background gradients G'_R (mT/m) in the human breast in the transverse plane (top), sagittal plane (center) and coronal plane (bottom). For all imaging directions, the background gradients are shown for both in-plane directions. The influence of G'_R may change with the chosen direction of G_R , since the patterns and range of the background gradients vary strongly depending on the direction, which is also illustrated by the histograms on the right.

Static field gradients are present *in vivo*, especially in the proximity of air-tissue boundaries (e.g. near the lungs or nasal cavities). To get a feel for the impact *in vivo*, the background gradients in the human breast were quantified at 3T. In the center of the breasts, the overall values for the background field gradients were ranging between -0.04 and 0.04 mT/m, except for the sagittal field map gradient in the z-direction, where higher values for G' were found in a large part of the center of the breast. It was shown that the influence of such background gradient strengths on errors in the temperature maps depends on the strength and direction of the imaging gradients used.

The field gradient maps in the human breast were acquired using a shimming protocol normally used for clinical diagnostic breast imaging. In case of shimming errors, larger background gradients can be expected. Besides, the magnitude of static field gradients increases with increasing external magnetic field, and therefore the background gradients problem for MRT is expected to be worse at higher field strengths.

During laser ablation, temperature gradients of 4 °C per millimeter have been observed

CHAPTER 7

(17), which correspond to gradients in the field observed by the hydrogen nuclei of 0.12 mT/m at 3T. This implies that in the absence of background gradients prior to heating, temperature errors may be introduced due to the heating pattern itself.

The reduction of the image distortions and signal dephasing (especially in case of through-plane G') has been the major focus of studies regarding the influence of background gradients. To the best of our knowledge, the influence of G_R' has been given no attention in the field of MR thermometry. The temporal echo shifting not only influences MR temperature mapping techniques. It affects the spectral properties of all MR signals acquired using a multi gradient-echo sequence. It will therefore have implications in the field of T_2^* relaxometry as well.

The influence of background gradients depends on their strength and orientation with respect to the imaging gradients. For very strong imaging gradients, less influence of G_R' is seen. However, in case of mGE-based MRT, which employs very strong G_R (> 20 mT/m) errors do still occur. For static situations without time-varying field disturbances, the magnitude of G_R' can be assessed prior to scanning. In that case, accurate field gradient mapping would facilitate better choices with regard to the direction and strength of the read-out gradient employed, to avoid errors due to background gradients *in vivo*. Furthermore, the temporal echo shift may be derived from background field gradient maps, which could then be used in the post-processing procedure for improved temperature mapping.

REFERENCES

1. Hindman JC. Proton Resonance Shift of Water in the Gas and Liquid States. *Journal of Chemical Physics* 1966;44:4582-4592.
2. Peters RD, Hinks RS, Henkelman RM. Ex vivo tissue-type independence in proton-resonance frequency shift MR thermometry. *Magn Reson Med* 1998;40(3):454-459.
3. Kuroda K, Mulkern RV, Oshio K, Panych LP, Nakai T, Moriya T, Okuda S, Hyynnen K, Jolesz FA. Temperature mapping using the water proton chemical shift: self-referenced method with echo-planar spectroscopic imaging. *Magn Reson Med* 2000;43(2):220-225.
4. McDannold N, Barnes AS, Rybicki FJ, Oshio K, Chen NK, Hyynnen K, Mulkern RV. Temperature mapping considerations in the breast with line scan echo planar spectroscopic imaging. *Magn Reson Med* 2007;58(6):1117-1123.
5. McDannold N, Hyynnen K, Oshio K, Mulkern RV. Temperature monitoring with line scan echo planar spectroscopic imaging 39. *MedPhys* 2001;28(3):346-355.
6. Mulkern RV, Panych LP, McDannold NJ, Jolesz FA, Hyynnen K. Tissue temperature monitoring with multiple gradient-echo imaging sequences. *J Magn Reson Imaging* 1998;8(2):493-502.
7. Sprinkhuizen SM, Bakker CJ, Bartels LW. Absolute MR thermometry using time domain analysis of multi gradient-echo magnitude images. *Magn Reson Med* 2010;in press.
8. Taylor BA, Hwang KP, Elliott AM, Shetty A, Hazle JD, Stafford RJ. Dynamic chemical shift imaging for image-guided thermal therapy: analysis of feasibility and potential. *Med Phys* 2008;35(2):793-803.
9. Mansfield P. Spatial mapping of the chemical shift in NMR. *Magn Reson Med* 1984;1(3):370-386.
10. Reichenbach JR, Venkatesan R, Yablonskiy DA, Thompson MR, Lai S, Haacke EM. Theory and application of static field inhomogeneity effects in gradient-echo imaging. *J Magn Reson Imaging* 1997;7(2):266-279.
11. Fernandez-Seara MA, Wehrli FW. Postprocessing technique to correct for background gradients in image-based $R^*(2)$ measurements. *Magn Reson Med* 2000;44(3):358-366.
12. Meng Y, Lei H. A single-scan T_2^* mapping method based on two gradient-echo images with compensation for macroscopic field inhomogeneity. *Magn Reson Med* 2008;60(6):1388-1395.
13. Truong TK, Chakeres DW, Scharre DW, Beversdorf DQ, Schmalbrock P. Blipped multi gradient-echo slice excitation profile imaging (bmGESEPI) for fast T_2^* measurements with macroscopic B_0 inhomogeneity compensation. *Magn Reson Med* 2006;55(6):1390-1395.
14. de Zwart JA, van Gelderen P, Kelly DJ, Moonen CT. Fast magnetic-resonance temperature imaging. *J Magn Reson B* 1996;112(1):86-90.
15. Amman C, Meier P, Merbach AE. A simple multinuclear NMR thermometer. *J Magn Reson* 1982;46:319-321.

CHAPTER 7

16. Peters NH, Bartels LW, Sprinkhuizen SM, Vincken KL, Bakker CJ. Do respiration and cardiac motion induce magnetic field fluctuations in the breast and are there implications for MR thermometry? *J Magn Reson Imaging* 2009;29(3):731-735.
17. Germain D, Chevallier P, Laurent A, Savart M, Wassef M, Saint-Jalmes H. MR monitoring of laser-induced lesions of the liver *in vivo* in a low-field open magnet: temperature mapping and lesion size prediction. *J Magn Reson Imaging* 2001;13(1):42-49.

STATIC FIELD INHOMOGENEITY AS A SOURCE OF ERRORS IN MRT

← IN CHAPTER 6, IT WAS SHOWN THAT MGE-BASED MR THERMOMETRY ALLOWS FOR ABSOLUTE TEMPERATURE MAPPING USING THE RESONANCE FREQUENCY DIFFERENCE BETWEEN THE HYDROXYL AND METHYLENE GROUP IN ETHYLENE GLYCOL

WITH THE EARLIER EXPERIENCE OF MGE-BASED MRT WE HYPOTHEZIZED THAT THE PEG OF THESE PEG LABELED LIPIDS MAY PROVIDE A TEMPERATURE INSENSITIVE PROTON RESONANCE FREQUENCY COMPONENT THAN CAN SERVE AS A REFERENCE FOR ABSOLUTE MR TEMPERATURE MEASUREMENTS

IN THE FOLLOWING CHAPTER, A NEW APPLICATION OF THIS WORK WILL BE PROPOSED. IN THE FIELD OF LIPOSOMAL DRUG DELIVERY, PEGYLATED LIPOSOMES ARE EMPLOYED, WHICH CONSIST OF BILAYER-FORMING LIPIDS AND POLYETHYLENE GLYCOL (PEG) LABELED LIPIDS INCORPORATED IN THE BILAYER TO INCREASE CIRCULATION HALF-LIVES IN VIVO AND TO REDUCE INTERACTIONS OF THE LIPOSOMES WITH PLASMA PROTEINS.

THE FEASIBILITY OF PERFORMING DYNAMIC ABSOLUTE MR THERMOMETRY USING A MULTI GRADIENT ECHO SEQUENCE IN COMBINATION WITH PEGYLATED LIPOSOMES WAS EVALUATED, RESULTS OF WHICH ARE DESCRIBED IN THE NEXT CHAPTER 

8

POLYETHYLENE GLYCOL LABELED LIPOSOMAL DRUG DELIVERY SYSTEMS AS A SOURCE FOR DYNAMIC ABSOLUTE MR THERMOMETRY

INTRODUCTION

Liposomes are widely used to increase the therapeutic index of a broad range of chemotherapeutic agents by increasing the circulation time and providing sustained release of the chemotherapeutic agent. Drugs loaded in long circulating liposomes benefit from tumor-specific accumulation due to the enhanced permeability and retention (EPR) effect. Although encapsulation of cytotoxic drugs in long circulating liposomes showed reduced systematic toxicity and increased levels of intratumoral drug accumulation, the therapeutic efficacy was not improved (1,2). These findings were attributed to the slow and passive drug release from these liposomes which did not significantly elevate the local bio-availability of the drug.

In 1978, Yatvin et al. introduced the idea of temperature sensitive liposomes for fast temperature mediated release of the drug and thereby augmenting the local bio-availability (3). It has been observed that temperature-sensitive release exposes cells to a higher drug concentration (4). Temperature sensitive liposomal drug delivery systems achieve complete release of their contents within 20 seconds when exposed to mild hyperthermia (40–42 °C), thereby reducing systemic toxicity and improving therapeutic efficacy. When performing drug delivery using temperature sensitive liposomes, it is important to verify that the heating is correctly localized with regard to the targeted volume and that the temperature is sufficiently high to release the contents, but simultaneously low enough to prevent tissue damage. Therefore, a precise and accurate measurement and control of temperature is necessary.

MR is capable of measuring temperature non-invasively *in vivo*. The method of choice is based on the temperature dependence of the proton electron screening constant of water (5). Temperature increase results in an increased electron shielding constant of the protons. As a result, the proton resonance frequency (PRF) of the water proton becomes lower at higher temperatures. In proton resonance frequency shift (PRFS)-based MR thermometry (MRT), changes of the proton resonance frequency are translated into temperature changes. This method does not allow for absolute temperature

CHAPTER 8

measurements without a known absolute temperature distribution at the start of the measurement.

In the application of temperature sensitive liposomal drug delivery, the temperature monitoring requirements are to measure absolute temperature without the need of a reference temperature. An absolute MR thermometry technique which has been developed for this type of therapy is liposomal thermometry (6,7). This method employs the release of (paramagnetic) contrast agent from the liposomes which occurs when the liposomal phase transition temperature (T_m) has been reached. Signal enhancement on T_1 -weighted MR magnitude images is observed when the absolute temperature rises above T_m . Drawback of this technique is the fact that paramagnetic thermosensitive liposomes only indicate if T_m is reached and thus cannot be used for continuous MR temperature mapping.

Absolute temperature measurements can also be performed by exploiting the frequency difference $\Delta f(T)$ between a temperature sensitive resonance and the resonance of a temperature insensitive reference component (8,9). This reference-based thermometry requires an MR technique which maps the two resonance frequencies of interest. An MR technique that can be used for this purpose is MR spectroscopy (MRS). A drawback of MRS and particularly MR Spectroscopic Imaging (MRSI) is their low spatial and temporal resolution. Measurements of multiple resonances can also be performed at high temporal and spatial resolution using a multi-gradient echo (mGE) sequence (10). This technique allows for dynamic temperature measurements (9). The temperature dependent resonance, water, is sufficiently present in tissue. The temperature independent resonance which is required may be delivered by fat tissue, which does not have a temperature dependent electron screening constant (11,12). However, fat may not always be present at the location of interest, and furthermore, the exact relation between the frequency difference between water and fat, Δf_{wf} , and absolute temperature is complicated since temperature might not be the only factor influencing Δf_{wf} in tissue (8,13).

We hypothesize that the reference resonance may be delivered by the liposomes themselves. Liposomes consist of bilayer-forming lipids and often polyethylene glycol (PEG) labeled lipids are incorporated in the bilayer to increase circulation half-lives *in vivo* and to reduce interactions of the liposomes with plasma proteins (14). The PEG may provide a temperature insensitive proton resonance frequency (PRF) component which can serve as reference for performing dynamic absolute MR thermometry.

In this study we aimed to determine whether absolute temperatures can be measured with mGE-based MR techniques using the resonance of PEG labeled to liposomes. For that reason, first, the temperature dependence of the frequency difference Δf_{ch} between the ethylene oxide group in PEG (f_e) and the PRF of the hydroxyl group in water (f_w) was determined. For this purpose, high field NMR experiments were conducted. Furthermore, we evaluated the feasibility of performing dynamic absolute mGE-based MR thermometry on a clinical MR system using PEG labeled liposomes. *In vitro* absolute temperature measurements were performed at different temperatures using the mGE sequence. Finally, the applicability of this MR thermometry technique in *in vivo* applications was assessed. To that end, temperature mapping of a dilution series of the pegylated liposome solution was performed to determine the lower detection limit of the PEG resonance frequency.

METHODS

Liposomes preparation and characterization

Liposomes were prepared by the conventional thin-film hydration technique and consisted of DPPC, DSPE-PEG5000 and cholesterol in a molar ratio of 1.85:0.15:1. The phospholipid content was determined with a phosphate assay in order to determine the total lipid content after extrusion. The average size of the liposomes were determined by dynamic light scattering. The prepared liposomes had a mean size of 120 nm and a phospholipid concentration of 81 mM in phosphate buffered saline (PBS).

Determining $\Delta f_{ch}(T)$

The high-field NMR experiments were performed on a Bruker Ultrashield 600 MHz spectrometer. Prior to the liposome experiments, temperature calibration was performed to measure and correct for differences between the temperature as indicated on the spectrometer and the true sample temperature. A dedicated temperature calibration sample (Bruker, 80% glycol DMSO-d⁶) was measured for a range of temperatures. For each spectrum, the actual temperature of the calibration sample was calculated using the empirically found relationship (from the Bruker VTU manual):

$$T_{sample}({}^{\circ}\text{C}) = \frac{4.218 - \Delta}{0.009132} - 273.15$$

The liposome sample was in 90% (v/v) PBS solution and 10% D₂O for field locking. DSS (2 mM) was added as internal chemical shift reference. The sample was transferred to a 5 mm NMR sample tube. One-dimensional ¹H-NMR spectra were recorded at eleven different temperatures ranging between 16.5 °C and 63.3 °C. Typically, 64 scans were accumulated per spectrum. The acquisition time was 0.85 sec, the spectral width was 16.02 ppm and the inter scan delay was set to 3 seconds to ensure complete recovery of equilibrium magnetization. To ensure sufficient time for homogeneous temperature distribution within the sample, a temperature equilibration period of 15 minutes was allowed after the sample temperature had reached each step in the temperature sequence.

All spectra were acquired with Bruker Topspin 2.1 software and analyzed using MestRe-C 4.9.9.6 [Mestrelab Research, Santiago de Compostela, Spain]. Per temperature, the proton resonance frequency of the ethylene oxide group in PEG (f_{ch}) and the PRF of the hydroxyl group in water (f_h) was determined from the acquired spectrum by the peak picking algorithm as implemented in MestRe-C. The frequency difference Δf_{ch} was found by subtraction and was plotted against temperature. Subsequently, from this data, the temperature dependence of the frequency difference $\Delta f_{ch}(T)$ of the liposome sample was determined by a linear fit.

Absolute temperature measurements

All MR imaging experiments were performed on a clinical 3-T whole body MR scanner (Achieva, Philips Healthcare, Best, The Netherlands). A phantom consisting of a 25 ml boiling flask filled with liposome solution suspended in a 2000 ml beaker filled

CHAPTER 8

with manganese doped water was used. An mGE-based MRT scan was acquired of the phantom at five different temperatures ($30.5\text{ }^{\circ}\text{C}$, $36.3\text{ }^{\circ}\text{C}$, $40.1\text{ }^{\circ}\text{C}$, $41.0\text{ }^{\circ}\text{C}$ and $45.3\text{ }^{\circ}\text{C}$), which were verified with a calibrated optical thermometer (Luxtron, Santa Clara, CA, USA). Scan parameters were: $TR=500\text{ ms}$, first echo time $TE_1 = 3.5\text{ msec}$, echo spacing $\Delta TE = 3.5\text{ msec}$, 32 echoes, $\alpha=60^\circ$, acquisition voxel size $2\times 2\times 8\text{ mm}^3$, number of signal averages = 1, dynamic scan duration = 65.5 s. The signal from the PEG is expected to be very small compared to the water signal in the liposome solution. Water suppression is therefore required during mGE-based MRT of pegylated liposomes, to ensure the detection of both resonances. However, some water signal is required to ensure detection of Δf_{ch} . Therefore, incomplete SPAIR water suppression was employed for all scans. The incomplete suppression was performed by choosing the inversion delay time, such that maximum oscillations were observed in the acquired magnitude signal in the time domain. A shimming box was manually placed such that it covered the boiling flask completely. For all experiments, the frequency difference Δf_{ch} between the PRF of the ethylene oxide group in PEG (f_{e}) and the PRF of the hydroxyl group in water (f_{h}) was found by fitting the magnitude signal in the time domain per voxel, which yields Δf_{ch} as a direct output parameter in a single post-processing step (9). The absolute temperature was computed per voxel using the relation between Δf_{ch} and temperature derived from the NMR experiments. Subsequently, the mean and standard deviation of the temperature maps were computed after removal of outliers ($<20\text{ }^{\circ}\text{C}$ and $>50\text{ }^{\circ}\text{C}$) and compared to the optically measured temperature.

Dilution series

In *in vivo* applications, local liposomal concentrations in tumor tissue are lower than the concentration of the undiluted solution. To determine the lower detection limit of the PEG resonance in mGE-based absolute MR temperature mapping, a dilution series was performed. Eleven mGE-based MRT scans were acquired of the phantom at different concentrations ranging between 81 mM and 3.1 mM. The liposome solution was diluted by adding PBS. All experiments were performed with the temperature of the liposome solution around body temperature ($\approx 37\text{ }^{\circ}\text{C}$), which was verified with an optical fiber temperature measurement. Scan parameters were: $TR = 500\text{ ms}$, $TE_1 = 3.5\text{ msec}$, $\Delta TE = 3.5\text{ msec}$, 32 echoes, $\alpha = 60^\circ$, acquisition voxel size $2\times 2\times 8\text{ mm}^3$, number of signal averages = 1, dynamic scan duration= 65.5 s. Absolute temperature maps were processed per voxel by summation of the magnitude signal in a region of 3x3 voxels around and including the voxel of interest. Outliers were removed in the final temperature maps: voxels with a temperature below $20\text{ }^{\circ}\text{C}$ and above $50\text{ }^{\circ}\text{C}$ were set to zero.

RESULTS

Determining $\Delta f_{eh}(T)$

In Fig. 1, all high field NMR spectra of the liposome solution at eleven different temperatures are shown. The PRF of ethylene oxide in PEG is temperature independent, though the PRF of water shifts with temperature.

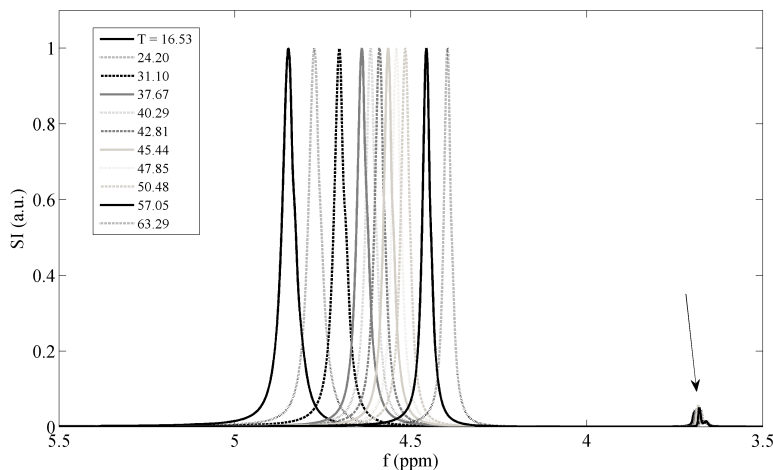


FIGURE 1 NMR Spectra of pegylated liposome solution for different temperatures. The water resonance peak shifts with temperature. The PEG peak, indicated by the arrow, does not have a temperature dependent shift.

At a temperature of 37.7 °C, the PRF of the ethylene oxide group in PEG and the PRF of the hydroxyl group in water are found (with respect to DSS) at 3.68 ppm and 4.64 ppm respectively. In Fig. 2, the relation between Δf_{eh} and absolute temperature is plotted, from which dependence of Δf_{eh} (in ppm) was found to be:

$$\Delta f_{eh}(T) = -0.0093 \cdot (T - T_{ref}) + 0.953 \quad [1]$$

with $T_{ref} = 37.7$ °C. The absolute temperature of the pegylated liposome solution can thus be found from Δf_{eh} using:

$$T = \frac{1}{-0.0093} \Delta f_{eh} + 140.11 \quad [2]$$

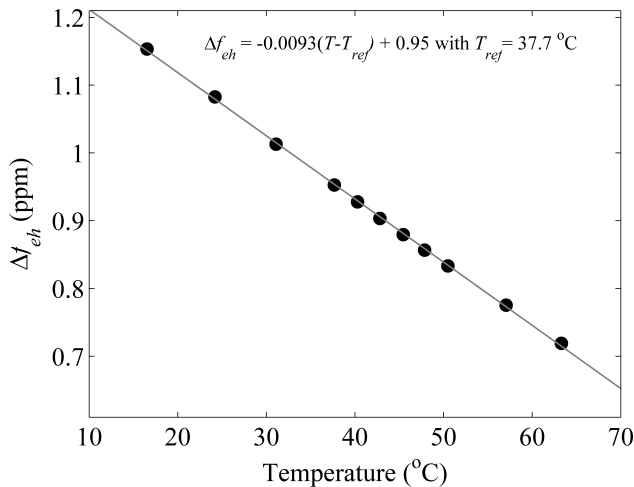


FIGURE 2 The resonance frequency difference between water and PEG, derived from the NMR spectra, is plotted against temperature. The temperature behaviour of the frequency difference between water and PEG was determined from the data points by a linear fit, result of which is shown in the inset.

Absolute temperature measurements

An example of a partly water suppressed magnitude mGE image of the phantom is shown in Fig. 3a. In the center of the phantom, the liposome solution can be seen. The partial water suppression ensured a ratio between the water and PEG signal which allowed for detection of Δf_{eh} in this solution. An example of the magnitude signal in the time domain and the fit to the data is shown in Fig. 3b.

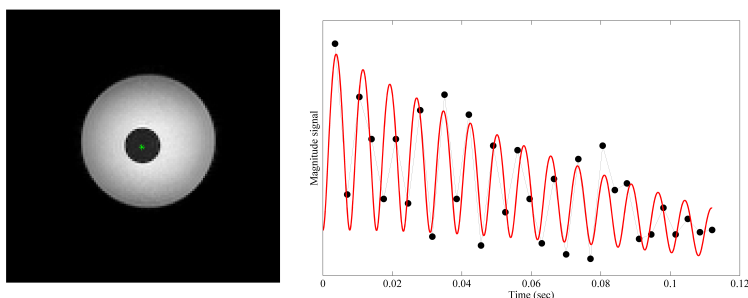


FIGURE 3 A magnitude image of the phantom containing a boiling flask filled with the pegylated liposome solution surrounded by water (a). The signal in time of a single voxel in the liposome solution (green asterisk in a) is plotted together with the result of the magnitude signal in time fitting procedure (red line) (b). The temperature measured with fiber optics for this scan was 30.45 °C. The absolute temperature found by the fitting procedure was 31.11 °C.

PEG LABELED LIPOSOMAL DRUG DELIVERY SYSTEMS FOR DYNAMIC ABSOLUTE MRT

Five absolute temperature maps of the liposome solution are shown in Fig. 4. The absolute temperature was determined per voxel. The temperature measured with fiber optics was compared to the mGE-based MRT outcome, showing a very good correlation (Fig. 5).

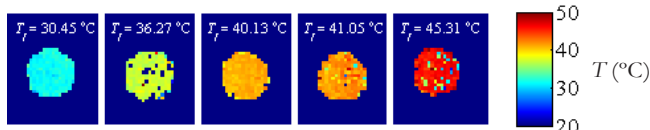


FIGURE 4 Absolute temperature maps of the liposomal solution at five different temperatures.

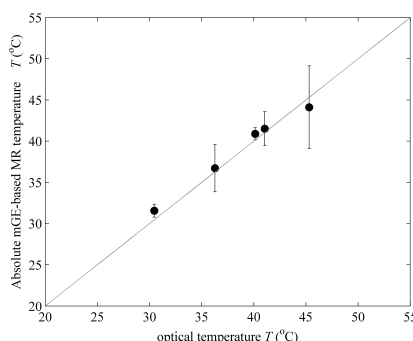


FIGURE 5 The mean temperature of the liposome solution as found with magnitude signal fitting is plotted against the optically measured temperature. The standard deviation is indicated by error bars.

Dilution series

The absolute temperature maps of the dilution series are shown in Fig. 6. In these temperature maps, the voxels which gave temperatures below 20 $^{\circ}\text{C}$ and above 50 $^{\circ}\text{C}$ were set to zero.

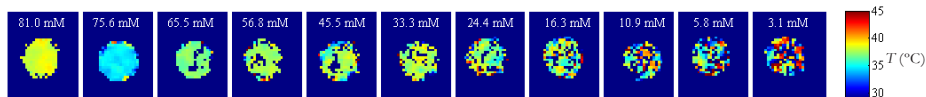


FIGURE 6 Absolute temperature maps of the liposomal solution at different concentrations. The post-processing was performed per voxel, for which the summed signal of 3x3 around and including the voxel of interest was used.

In figure 7, the absolute temperature of all voxels is plotted for three different concentrations (81 mM, 33 mM and the lowest concentration; 3.1 mM). This plot clearly shows the increase in standard deviation from the true temperature ($\approx 37\text{ }^{\circ}\text{C}$) with decreasing concentration.

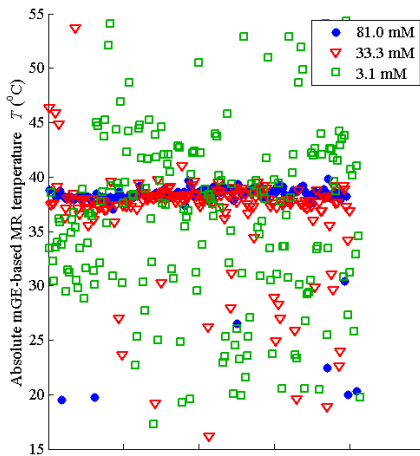


FIGURE 7 Plot of the temperature values of all voxels in the temperature map of three different concentrations of the liposomal fluid.

In Fig. 8, both the mean and standard deviation of the mGE-based MR temperature (ranging between 20 °C and 50 °C) as well as the optical temperature is shown for various concentrations of the liposome solution. Although there is a large increase in the spread of mGE-based temperature, the mean absolute temperature correlates well with the optical temperature measurements down to the lowest concentration.

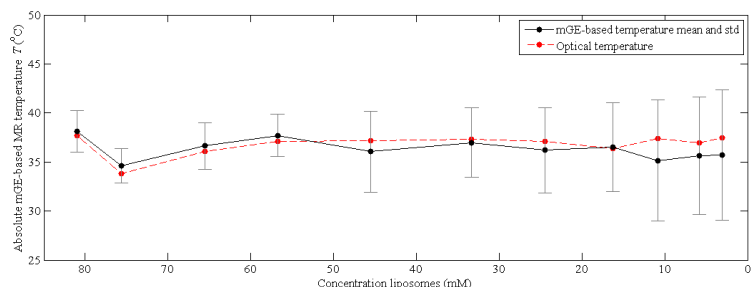


FIGURE 8 mGE-based MR temperature versus optical temperature for various concentrations of the liposome solution. Both the mean and standard deviation of all voxels in the temperature map ranging between 20-50 °C are shown.

DISCUSSION AND CONCLUSION

The results in this work show that absolute dynamic temperature mapping using the temperature dependent resonance frequency of water and temperature independent resonance frequency of PEG labeled to liposomes is feasible. The NMR spectroscopy study showed that the PRF of ethylene oxide in PEG is temperature independent and may serve as reference for determining the frequency shift of the temperature sensitive PRF of hydroxyl in water. A linear behaviour between temperature and the frequency difference Δf_{ch} was observed. Furthermore, we showed that both frequency components are detectable in a PEG labeled liposome solution with a partly water suppressed mGE imaging sequence. The absolute temperature of the liposomal formulation can be retrieved from the magnitude signal in the time domain.

From the dilution series we can conclude that with decreasing concentration of liposomes, the standard deviation of the temperature measurement increased. The mean temperature over the temperature map still showed a good correlation with the temperature measured with optic fibers. In our dilution experiment, the lowest concentration of phospholipids was 3.1 mM, corresponding to 3.1 $\mu\text{mol}/\text{cm}^3$ solution. The liposomal tumor accumulation during therapy *in vivo* in mice has been reported to exceed 2.5 $\mu\text{mol}/\text{gram tumor}$, which roughly corresponds to 2.5 $\mu\text{mol}/\text{cm}^3$ tumor tissue (15). The lowest concentration in our experiments is thus close to the reported concentration of liposomes *in vivo*. However, it was shown by the dilution experiment that the liposomal formulation and MR imaging parameters used in this study do not allow for precise absolute mGE-based MR temperature measurements with the PEG resonance as reference, due to insufficient signal to noise ratio. For translation to *in vivo* applications of this PEG-referenced MR thermometry technique, increased signal from the PEG resonance is thus required. Active targeting may increase local liposome concentrations in the targeted tissue and thereby increase the local PEG signal (16). In addition, the liposomes may be further improved for this specific thermometry application. Chemical adjustments may allow for an increase of the PEG-load per liposome.

REFERENCES

1. Safra T, Muggia F, Jeffers S, Tsao-Wei DD, Groshen S, Lyass O, Henderson R, Berry G, Gabizon A. Pegylated liposomal doxorubicin (doxil): reduced clinical cardiotoxicity in patients reaching or exceeding cumulative doses of 500 mg/m². *Ann Oncol* 2000;11(8):1029-1033.
2. Waterhouse DN, Tardi PG, Mayer LD, Bally MB. A comparison of liposomal formulations of doxorubicin with drug administered in free form: changing toxicity profiles. *Drug Saf* 2001;24(12):903-920.
3. Yatvin MB, Weinstein JN, Dennis WH, Blumenthal R. Design of liposomes for enhanced local release of drugs by hyperthermia. *Science* 1978;202(4374):1290-1293.
4. Hettinga JV, Konings AW, Kampinga HH. Reduction of cellular cisplatin resistance by hyperthermia--a review. *Int J Hyperthermia* 1997;13(5):439-457.
5. Hindman JC. Proton Resonance Shift of Water in the Gas and Liquid States. *Journal of Chemical Physics* 1966;44(12):4582-4592.
6. McDannold N, Fossehim SL, Rasmussen H, Martin H, Vykhotseva N, Hynynen K. Heat-activated liposomal MR contrast agent: initial in vivo results in rabbit liver and kidney. *Radiology* 2004;230(3):743-752.
7. Fossehim SL, Il'yasov KA, Hennig J, Bjornerud A. Thermosensitive paramagnetic liposomes for temperature control during MR imaging-guided hyperthermia: in vitro feasibility studies. *Acad Radiol* 2000;7(12):1107-1115.
8. Kuroda K. Non-invasive MR thermography using the water proton chemical shift. *Int J Hyperthermia* 2005;21(6):547-560.
9. Sprinkhuizen SM, Bakker CJ, Bartels LW. Absolute MR thermometry using time domain analysis of multi gradient-echo magnitude images. *Magn Reson Med* 2010;in press.
10. Mansfield P. Spatial mapping of the chemical shift in NMR. *Magn Reson Med* 1984;1(3):370-386.
11. De Poorter J. Noninvasive MRI thermometry with the proton resonance frequency method: study of susceptibility effects. *Magn Reson Med* 1995;34(3):359-367.
12. Stollberger R, Ascher PW, Huber D, Renhart W, Radner H, Ebner F. Temperature monitoring of interstitial thermal tissue coagulation using MR phase images 2. *J Magn Reson Imaging* 1998;8(1):188-196.
13. McDannold N, Barnes AS, Rybicki FJ, Oshio K, Chen NK, Hynynen K, Mulkern RV. Temperature mapping considerations in the breast with line scan echo planar spectroscopic imaging. *Magn Reson Med* 2007;58(6):1117-1123.
14. Drummond DC, Meyer O, Hong K, Kirpotin DB, Papahadjopoulos D. Optimizing liposomes for delivery of chemotherapeutic agents to solid tumors. *Pharmacol Rev* 1999;51(4):691-743.
15. Parr MJ, Masin D, Cullis PR, Bally MB. Accumulation of liposomal lipid and encapsulated doxorubicin in murine Lewis lung carcinoma: the lack of beneficial effects by coating liposomes with poly(ethylene glycol). *J Pharmacol Exp Ther* 1997;280(3):1319-1327.
16. Marcucci F, Lefoulon F. Active targeting with particulate drug carriers in tumor therapy: fundamentals and recent progress. *Drug Discov Today* 2004;9(5):219-228.

PEG LABELED LIPOSOMAL DRUG DELIVERY SYSTEMS FOR DYNAMIC ABSOLUTE MRT

9

GENERAL DISCUSSION

Within the context of minimally invasive treatment options, there is growing interest in thermal therapy. The outcome of thermal treatments is difficult to predict, since it depends on specific tissue properties like heat absorption and blood perfusion which are highly variable among people. For example, large variations of lesion diameters have been observed after thermal treatments which used identical heating protocols for tissue ablation using high intensity focused ultrasound (HIFU) (1-3). To prevent undertreatment of a lesion and to preserve the surrounding tissues from thermal damage, accurate and reliable temperature monitoring techniques are essential during thermal therapy.

Temperature can be measured non-invasively by MRI using a technique known as MR thermometry (MRT). MRT can be used for temperature mapping during thermal therapy *in vivo*. Since MR-based temperature information is of importance for predicting and determining treatment success, it is essential to have knowledge of the factors affecting the precision and the accuracy of MR thermometry.

In the research described in this thesis, the physical mechanisms behind MR thermometry have been studied in detail for improved understanding of the capabilities and problems related to this technique. The processes that lead from a specific temperature dependent physical quantity to actual temperature data have been explored at two different levels: 1. the temperature dependent parameter itself, and 2. the acquisition of the MR signal and the translation of the measured signals into temperature maps.

1. Temperature dependent parameters

The temperature dependence of several physical and physiological quantities translates to a number of temperature dependent MR parameters, an overview of which was given in chapter 2. It was pointed out that the temperature dependent proton electron screening constant of water is the parameter of choice for MRT. Changes in the proton electron screening lead to changes of the proton resonance frequency (PRF). These changes can be measured with MR and translated into temperature maps by using a technique known as proton resonance frequency shift (PRFS)-based MRT. However,

CHAPTER 9

the proton electron screening constant is not the only factor influencing the PRF of water protons. Other temperature dependent as well as temperature independent parameters are also involved.

An example of an effect that influences PRFS-based MRT is the presence of time varying magnetic field inhomogeneities. In the human body, such field variations are for example caused by respiratory motion. Especially in organs close to the lungs, like the human breast, these field effects may be expected to lead to problems with respect to MRT. Respiration-induced field inhomogeneities in the human breast were therefore quantified, to assess their impact on PRFS-based MRT (chapter 3). It was shown that respiration may induce errors in the temperature measurements up to 20 °C in the human breast. Thermal ablation procedures generally take too long to be performed within a breath-hold. For accurate MR thermometry in the breast during free breathing, dynamic field inhomogeneities due to respiratory motion should be corrected for.

The PRF of water protons is also influenced by the temperature dependence of the magnetic volume susceptibility, which is commonly neglected in current applications of MRT. In this thesis the influence of temperature dependent changes in the magnetic susceptibility of tissue on the PRF was investigated (chapter 4). It was shown both theoretically and experimentally that temperature-induced susceptibility changes can lead to changes in the magnetic field, which introduces significant temperature errors in PRFS-based MR thermometry. This effect is most pronounced in tissues containing fat, like the human breast and liver. Simulations showed that for the specific clinical case of MR-guided High Intensity Focused Ultrasound (HIFU) in the breast, an ellipsoidal HIFU thermal spot of diameter 8 mm and length 20 mm and a maximum temperature increase of $\Delta T = 30$ °C led to temperature errors in the glandular tissue ranging between -8.6 °C and +6.2 °C, depending orientation of the focal spot. It was concluded that for accurate MR thermometry measurements in fatty tissues, the influence of susceptibility changes may not be neglected. Susceptibility-related temperature errors are not only related to the shape and orientation of the heating pattern but also depend on the distribution of water and fat inside the heated area. The compensation of such errors is not straightforward and therefore requires patient specific analysis.

As already mentioned above, the temperature dependence of the susceptibility of fat tissue is of particular interest, since it was reported to be in the same order of magnitude as the temperature dependence of the proton electron screening constant of water. Furthermore, the results of chapter 4 imply that the influence of susceptibility changes in fat is not eliminated when fat suppression techniques are employed. To be able to assess the severity of this effect for thermal ablation of tumors in the breast, we performed a study to assess the temperature dependence of the susceptibility of human fat tissue (chapter 5). The results showed that average values of the temperature dependence of the susceptibility of human fat tissue during temperature rise and temperature fall were found to be somewhat smaller, but in the same order of magnitude as the reported temperature dependence for porcine precooked fat (4). These findings supported the conclusion from chapter 4 that the impact of heat-induced susceptibility changes during thermal therapy in fatty tissues like the human breast may not be neglected.

As was pointed out in chapter 2, PRFS-based MR thermometry is based on the measurement of PRF changes relative to a certain baseline situation, and can therefore only

yield information on temperature changes. The temperature-related PRF shift of water protons can be translated to absolute temperature if it can be calibrated with respect to a temperature independent parameter. The electron screening constant of protons in fat is near independent of temperature. In chapter 6, a method was proposed in which the fat resonance was used as a reference resonance for absolute temperature measurements. A multi gradient-echo (mGE) sequence is employed for detection of multiple resonances at high temporal and spatial resolution (5). First, the feasibility of the mGE-based MRT method was shown in a phantom set-up with two well calibrated resonances. Next, it was shown that in *ex vivo* bone marrow, the frequency difference between water and fat changes with temperature. However, it was concluded that the relation between this frequency difference and absolute temperature has to be examined more extensively because temperature dependent electron screening might not be the only factor influencing the frequency difference between water and fat in tissue.

In chapter 8, a potential future application of the technique proposed in chapter 6 was proposed. It was shown that absolute dynamic temperature mapping using the temperature dependent resonance frequency of water and a temperature independent resonance frequency provided by polyethyleneglycol (PEG) from pegylated liposomes is feasible. However, it was concluded that at clinically relevant concentrations of the currently used liposomal formulation, the absolute temperature cannot be measured with reasonable precision due to insufficient signal-to-noise ratio. For translation to *in vivo* applications of this PEG-referenced MR thermometry technique, increased signal from the PEG resonance is thus required. Active targeting may increase local liposome concentrations in the targeted tissue and thereby increase the local PEG signal (6). In addition, the liposomes can possibly be further improved for use with this specific thermometry technique. Chemical adjustments may allow for an increase of the PEG-load per liposome.

2. MR signal acquisition and translation into temperature

Since the post-processing of MR signals into temperature data is based on certain assumptions with regard to the acquired signal, errors will be introduced when these assumptions are incorrect. MR thermometry techniques that are based on the temperature dependence of the water proton resonance frequency are generally considered to be insensitive to static field inhomogeneities, because they either employ subtraction of successive phase images (PRFS-based MRT) or use an internal temperature-independent reference component (mGE-based MRT). In chapter 7 it was shown that MR thermometry measurements are most certainly affected by the presence of static background field gradients, and in particular by background gradients that are aligned with the read-out gradient. Such background field gradients may alter the effective echo time in gradient-echo acquisitions. It was shown that the temporal echo shift induces temperature errors in PRFS-based and mGE-based MR thermometry. To assess the impact of static background gradients for the specific application of MRT in the human breast, we performed static field gradient mapping in the breasts of a volunteer. It was concluded that accurate field gradient mapping may facilitate better choices with regard to the direction and strength of the read-out gradient employed.

A novel time-domain post-processing technique for mGE-based MRT was introduced in chapter 6. An elegant feature of this approach is the fact the parameter of interest, i.e. the frequency difference between a temperature dependent and temperature independent resonance, is a direct output parameter, in contrast to methods which indirectly compute the frequency difference after fitting the separate frequencies in the frequency domain (7-9). The fitting procedure was extremely tolerant regarding the starting value for the frequency difference. This is an important beneficial property, since, during a thermal intervention, the fitting procedure has to yield the correct temperature without detailed prior knowledge on the current temperature distribution. The magnitude fit in the time domain appeared to be less affected by the presence of field disturbances with regard to the parameter of interest compared to the frequency domain method. However, it was concluded that both techniques have advantages and drawbacks, and may be used complementarily in future applications of this technique.

In chapter 8, this post-processing approach was employed for a potential future application of mGE-based MRT, being temperature sensitive liposomal drug delivery using pegylated liposomes.

FUTURE PERSPECTIVES

In this thesis, experiments have been performed at field strengths of 1.5 T and 3 T. In the field of MRI, there is a tendency to move towards higher field strengths. At first sight, increasing the field strength seems beneficial for PRFS-based MR temperature measurements, since the sensitivity to temperature changes is higher at higher field because the PRF shift per degree Celsius increases. In addition, the increase of signal-to-noise ratio (SNR) at higher field strength reduces the standard deviation in the phase images and therefore increases the precision of the temperature maps. However, the transverse relaxation time T_2^* decreases at higher field strength which may counteract the benefit of increased PRF shift, since echo times in the order of the T_2^* of the tissue are ideally chosen in PRFS-based MRT, to maximize the SNR of the temperature maps (10). In addition, the magnitude of static field gradients increases with increasing external magnetic field strength, and therefore, when moving towards higher field strength, the influence of background gradients on MRT increases (chapter 7).

Throughout this thesis, several physical effects which influence the PRF of water and fat have been studied. It was shown that the magnetic volume susceptibility of breast fat tissue is temperature dependent, leading to errors in PRFS-based MR temperature measurements during thermal therapy. Susceptibility-related errors due to the heating of fat are also expected to occur in other tissues which contain fat like the liver and bone marrow. Measurement of the temperature dependence of the susceptibility for different tissue types is of interest. Susceptibility-related effects may explain the variation in values for the temperature dependence of the PRF in various tissues found in literature (11).

In addition, more insight in the influence of biological processes on the susceptibility distribution during thermal therapy is required. Tissue susceptibility may change due to changes in tissue perfusion during thermal therapy, leading to alterations in the balance

of oxygenated and deoxygenated hemoglobin and myoglobin (12). Also, changes in the tissue shape and size (e.g. caused by edema) are a source of changes in the susceptibility distribution (13).

The influence of temperature induced magnetic susceptibility changes on MRT is an important and from a physicist point of view interesting field of research. Theoretically, the susceptibility distribution can be calculated from field maps. However, for arbitrary susceptibility distributions, complex numerical methods are required (14). Knowledge on the susceptibility distribution during thermal therapy would allow for more accurate temperature measurements in water nearby heated fatty tissues. In addition, susceptibility measurements may allow for temperature mapping in fat.

REFERENCES

1. Chung AH, Jolesz FA, Hynnen K. Thermal dosimetry of a focused ultrasound beam in vivo by magnetic resonance imaging. *Med Phys* 1999;26(9):2017-2026.
2. Gianfelice D, Khiat A, Amara M, Belblidia A, Boulanger Y. MR imaging-guided focused US ablation of breast cancer: histopathologic assessment of effectiveness--initial experience. *Radiology* 2003;227(3):849-855.
3. Hindley J, Gedroyc WM, Regan L, Stewart E, Tempany C, Hynnen K, McDannold N, Inbar Y, Itzhak Y, Rabinovici J, Kim HS, Geschwind JF, Hesley G, Gostout B, Ehrenstein T, Hengst S, Sklair-Levy M, Shushan A, Jolesz F. MRI guidance of focused ultrasound therapy of uterine fibroids: early results. *AJR Am J Roentgenol* 2004;183(6):1713-1719.
4. Stollberger R, Ascher PW, Huber D, Renhart W, Radner H, Ebner F. Temperature monitoring of interstitial thermal tissue coagulation using MR phase images 2. *J Magn Reson Imaging* 1998;8(1):188-196.
5. Mansfield P. Spatial mapping of the chemical shift in NMR. *Magn Reson Med* 1984;1(3):370-386.
6. Marcucci F, Lefoulon F. Active targeting with particulate drug carriers in tumor therapy: fundamentals and recent progress. *Drug Discov Today* 2004;9(5):219-228.
7. Kuroda K, Mulkern RV, Oshio K, Panych LP, Nakai T, Moriya T, Okuda S, Hynnen K, Jolesz FA. Temperature mapping using the water proton chemical shift: self-referenced method with echo-planar spectroscopic imaging. *Magn Reson Med* 2000;43(2):220-225.
8. McDannold N, Barnes AS, Rybicki FJ, Oshio K, Chen NK, Hynnen K, Mulkern RV. Temperature mapping considerations in the breast with line scan echo planar spectroscopic imaging. *Magn Reson Med* 2007;58(6):1117-1123.
9. McDannold N, Hynnen K, Oshio K, Mulkern RV. Temperature monitoring with line scan echo planar spectroscopic imaging 39. *Med Phys* 2001;28(3):346-355.
10. de Zwart JA, van Gelderen P, Kelly DJ, Moonen CT. Fast magnetic-resonance temperature imaging. *J Magn Reson B* 1996;112(1):86-90.
11. McDannold N. Quantitative MRI-based temperature mapping based on the proton resonant frequency shift: review of validation studies. *Int J Hyperthermia* 2005;21(6):533-546.
12. Young IR, Hajnal JV, Roberts IG, Ling JX, Hill-Cottingham RJ, Oatridge A, Wilson JA. An evaluation of the effects of susceptibility changes on the water chemical shift method of temperature measurement in human peripheral muscle. *Magn Reson Med* 1996;36(3):366-374.
13. McDannold N, Hynnen K, Jolesz F. MRI monitoring of the thermal ablation of tissue: effects of long exposure times. *J Magn Reson Imaging* 2001;13(3):421-427.
14. Li L, Leigh JS. Quantifying arbitrary magnetic susceptibility distributions with MR. *Magn Reson Med* 2004;51(5):1077-1082.

10

SUMMARY & SAMENVATTING

SUMMARY

The research described in this thesis has aimed to further investigate magnetic resonance (MR) thermometry (MRT) techniques as to become a reliable guidance tool for thermal therapy. A general introduction to MR thermometry is given in **chapter 2**. The various physical processes allowing for temperature measurements based upon the MR signal are described. It is demonstrated that proton resonance frequency shift (PRFS)-based MRT, which employs the temperature dependence of the proton electron screening constant of water, is the method of choice. Potential sources of error in PRFS-based MRT are identified, in particular time varying magnetic field inhomogeneities and heat-induced changes of the magnetic susceptibility of tissue.

A source of time varying magnetic field inhomogeneities *in vivo* is respiration. A study was conducted to quantify respiration-induced field inhomogeneities in the human breast, to assess its impact on PRFS-based MRT. The results of this study are described in **chapter 3**. The average field fluctuation due to regular respiration was 0.13 ppm and due to maximum capacity respiration 0.16 ppm. These numbers can be misinterpreted as temperature changes of 13 °C and 16 °C, respectively, when PRFS based MR thermometry is used during thermal treatment of breast cancer. In conclusion, respiration causes significant field fluctuations in the breast that should be corrected for to allow accurate MR thermometry in the human breast under free breathing circumstances.

Chapter 4 is concerned with the temperature dependence of the magnetic volume susceptibility of tissue, in particular with that of fat tissue. This study assessed the influence of the temperature dependence of the susceptibility of tissue on PRFS-based MRT during thermal therapy. Heating experiments were performed in a controlled phantom set-up to show the impact of temperature-induced susceptibility changes on PRFS-based temperature maps. To study the implications for a clinical patient, simulations were performed in a 3D breast model for the specific clinical case of MR-guided High Intensity Focused Ultrasound (HIFU) in the breast. The simulations showed that an ellipsoidal HIFU thermal spot of diameter 8 mm and length 20 mm and a maximum temperature increase of $\Delta T = 30$ °C led to temperature errors in the glandular tissue ranging between -8.6 °C and +6.2 °C, depending on the orientation of the focal spot.

CHAPTER 10

It was concluded that the influence of susceptibility changes may lead to significant temperature errors in PRFS-based MRT that are not to be neglected. Rather, a more thorough understanding of the relation between temperature and magnetic susceptibility was found to be required. Especially the temperature dependence of the susceptibility of fat tissue is of interest, since it is reported to be in the same order of magnitude as the temperature dependence of the proton electron screening constant of water. However, no values have been reported in literature on the temperature dependence of the susceptibility of human fat tissue. Therefore, a study was conducted in which this temperature dependence was measured for human breast fat tissue, the results of which are described in **chapter 5**. In this work *ex vivo* measurements were performed on a 14.1 T five millimeter narrow bore NMR spectrometer. Breast fat tissue samples were collected from six subjects, directly post-mortem. The susceptibility was measured over a temperature range from 24 °C to 65 °C. A linear behaviour of the susceptibility over temperature was observed in all six samples. The resulting temperature dependence of the susceptibility of human breast fat ranged between 0.0038 and 0.0076 ppm/°C. The outcome of this study supports the findings described in chapter 4 that the impact of heat-induced susceptibility changes of fat during thermal therapy in the breast may not be neglected.

There is an additional issue regarding tissues containing fat. The electron screening constant of protons in fat is near independent of temperature which hampers PRFS-based temperature mapping in fatty tissues. However, the presence of fat may be used to our benefit by using it as a temperature independent reference signal which allows for absolute rather than relative MR temperature measurements. Multiple resonances can be separately detected in spectroscopic data. An image-based MR technique which allows for the acquisition of spectroscopic data at high temporal and spatial resolution is the multi gradient-echo (mGE) sequence. **Chapter 6** reports on a study in which the application of the mGE sequence for MR thermometry purposes was further developed. The possibility of post-processing the mGE data into absolute temperature maps using time domain analysis of the magnitude of the mGE signals was investigated. *In vitro* experiments were performed to provide proof of concept for retrieving absolute temperature maps from the time domain analysis of mGE magnitude images. It is shown that this technique is insensitive to both field drift and local field disturbances. Furthermore, *ex vivo* bone marrow experiments were performed, using the fat resonance as a reference for absolute temperature mapping. It was shown that the post-processing based on the magnitude signal in the time domain allows for the determination of the resonance frequency difference between water and fat in bone marrow. However, it was concluded that the relation between this frequency difference and absolute temperature has to be examined more extensively because temperature dependent electron screening might not be the only factor influencing the frequency difference between water and fat in tissue.

The post-processing of the MR signal to obtain temperature maps is based on certain assumptions with regard to the acquired signal. **Chapter 7** is concerned with a specific situation in which the assumed properties of the acquired signal are incorrect. MR thermometry techniques that are based on the temperature dependence of the water proton resonance frequency are generally considered to be insensitive to static field inhomoge-

neities, because they either employ subtraction of successive phase images (PRFS-based MRT) or use an internal temperature-independent reference component (mGE-based MRT). In this chapter it is shown that MR thermometry measurements are most certainly affected by the presence of static background field gradients, and in particular by background gradients that are aligned with the read-out gradient. Both theoretically and in phantom experiments it was shown that static background field gradients alter the effective echo time in gradient-echo acquisitions, which induces temperature errors in PRFS-based and mGE-based MR thermometry. The impact of static background gradients on MRT *in vivo* was assessed by static field gradient mapping in the breast of a volunteer. It was concluded that accurate field gradient mapping would facilitate better choices with regard to the direction and strength of the read-out gradient employed, to avoid errors due to background gradients *in vivo*.

In **chapter 8**, a new application of the work described in chapter 6 is explored. It is hypothesized that polyethylene glycol signals from pegylated liposomes may provide a temperature insensitive proton resonance frequency component than can serve as a reference for absolute MR temperature measurements. The feasibility of performing dynamic absolute MR thermometry using a multi-gradient echo sequence in combination with pegylated liposomes is evaluated. It was shown by a dilution experiment that at clinical relevant concentrations, the liposomal formulation and MR imaging parameters used in this study do not allow for precise absolute mGE-based MR temperature measurements with the PEG resonance as reference, due to insufficient signal-to-noise ratio. For translation to *in vivo* applications of this PEG-referenced MR thermometry technique, increased signal from the PEG resonance is thus required, which may be achieved by active targeting or by chemical adjustments to increase the PEG-load per liposome.

SAMENVATTING

Het doel van het onderzoek dat beschreven wordt in dit proefschrift is de verdere ontwikkeling van magnetic resonance (MR) thermometrie (MRT) tot een betrouwbare methode voor het geleiden van thermische therapie. Een algemeen overzicht van MR thermometrie technieken wordt gegeven in **hoofdstuk 2**. De verschillende fysische principes die het meten van temperatuur op basis van het MR signaal toestaan worden beschreven. Er wordt uitgelegd dat de techniek die gebaseerd is op de temperatuurafhankelijkheid van de proton electron screening constante, PRFS-based MRT, de voorkeur heeft. Deze techniek kent verscheidene foutenbronnen, zoals tijdsafhankelijke veranderingen in het magneetveld en warmte-geïnduceerde veranderingen in de magnetische susceptibiliteit van het weefsel.

Een bron van tijdsafhankelijke magnetische veldveranderingen *in vivo* is de ademhaling. In **hoofdstuk 3** wordt de invloed van ademhalingsafhankelijke veldinhomogeniteiten op PRFS-based MRT in de borst onderzocht. De resultaten van deze studie laten zien dat de gemiddelde veldveranderingen die gevonden werden 0.13 ppm bedroegen voor normale ademhaling en 0.16 ppm voor maximale in- en uitademhaling. Deze waarden

CHAPTER 10

kunnen foutief geïnterpreteerd worden als temperatuursveranderingen van respectievelijk 13 °C en 16 °C wanneer PRFS-based MRT gebruikt wordt tijdens thermische therapie van borsttumoren. Concluderend, de ademhaling veroorzaakt significante veldinhomogeniteiten in de borst welke gecorrigeerd moeten worden om accurate MR temperatuurmetingen in de borst te kunnen verrichten.

In **hoofdstuk 4** wordt onderzocht wat de invloed is van de temperatuurafhankelijkheid van de susceptibiliteit van weefsel op PRFS-based MRT gedurende thermische therapie. Verwarmingsexperimenten zijn uitgevoerd in een gecontroleerde fantomopstelling om de invloed van opwarming-geïnduceerde susceptibiliteitsveranderingen in PRFS-based MR temperatuurbeelden te demonstreren. Om de gevolgen voor een klinische situatie te onderzoeken zijn simulaties uitgevoerd voor de specifieke situatie van MR-geleide High Intensity Focussed Ultrasound (HIFU) in de borst. Deze simulaties toonden aan dat een elliptisch HIFU focus met een diameter van 8 mm, een lengte van 20 mm en een maximale temperatuurverandering van 30 °C, temperatuurfouten veroorzaakte in het borstklierweefsel tussen de -8.6 °C en +6.2 °C, afhankelijk van de orientatie van het thermische focus. Geconcludeerd werd dat temperatuur gerelateerde susceptibiliteitsveranderingen van het weefsel tot substantiële fouten in de PRFS-based MR temperatuurmetingen kunnen leiden welke in acht genomen dienen te worden. In het bijzonder is de temperatuurafhankelijkheid van de susceptibiliteit van vetweefsel interessant, omdat deze op basis van de literatuur van dezelfde ordegrootte is als de temperatuurafhankelijkheid van de proton electron screening constante van water. Er zijn echter geen publicaties over de temperatuurafhankelijkheid van de susceptibiliteit van menselijk vet weefsel. Om deze reden is er een studie uitgevoerd om deze temperatuurafhankelijkheid te meten, waarvan de resultaten gepresenteerd worden in **hoofdstuk 5**. De experimenten in hoofdstuk 5 werden uitgevoerd op een 14.1 T 5 mm narrow bore NMR spectrometer. Vetweefsel uit de borst werd verkregen van zes personen, direct na overlijden. De susceptibiliteit van het vetweefsel is gemeten over een temperatuurbereik van 24 °C tot 65 °C. Een lineair verband tussen de susceptibiliteit en de temperatuur werd geobserveerd in alle zes de samples. De temperatuurafhankelijkheid van de susceptibiliteit van het vetweefsel uit de borst varieerde tussen 0.0038 and 0.0076 ppm/ °C. Deze resultaten bevestigen de bevindingen uit hoofdstuk 4 waarin werd gesteld dat de temperatuurafhankelijkheid van vetweefsel in acht genomen moet worden tijdens thermische therapie in de borst.

PRFS-based MRT metingen in weefsel die vet bevatten worden tevens bemoeilijkt door het feit dat de electron screening constante van protonen in vet bijna onafhankelijk is van de temperatuur. Dit nadeel kan omgezet worden naar een voordeel: de aanwezigheid van vet kan gebruikt worden als temperatuuronafhankelijk referentiesignaal om zo absolute temperatuurmetingen te kunnen verrichten in tegenstelling tot relatieve metingen. In spectroscopische data kunnen meerdere resonanties apart gedetecteerd worden. Een MR techniek die spectroscopische informatie oplevert met hoge spatiale en temporele resolutie is de multi gradiënt echo (mGE) sequentie. In **hoofdstuk 6** worden de resultaten beschreven van een studie waarin de toepassing van de mGE sequentie voor MR themometrie verder wordt ontwikkeld. De mogelijkheid om mGE data te bewerken tot absolute temperatuurbeelden op basis van de analyse van het magnitude signaal in het tijdsdomein is onderzocht. *In vitro* experimenten toonden aan dat

absolute temperatuurbeelden gevormd kunnen worden uit de tijdsdomein-analyse van de magnitude mGE beelden, welke ongevoelig zijn voor veld drift en lokale veldverstoringen. Uit *ex vivo* beenmerg experimenten, waarbij de vet resonantie als referentie voor absolute temperatuurmetingen werd gebruikt, bleek dat de beeldbewerking op basis van het magnitude signaal in het tijdsdomein het verschil in resonantie frequentie tussen water en vet in beenmerg kan detecteren. Daarbij werd geconcludeerd dat de relatie tussen dit frequentie verschil en de absolute temperatuur van weefsel meer onderzoek vereist, aangezien de temperatuurafhankelijkheid van de electron screening constante mogelijk niet de enige invloed op het resonantie frequentie verschil tussen water en vet in weefsel is.

Het bewerken van MR signalen om informatie over de temperatuur te verkrijgen is gebaseerd op bepaalde aannames met betrekking tot het geacquireerde signaal. In **hoofdstuk 7** is een specifieke situatie onderzocht waarin deze aannames incorrect blijken te zijn. MR thermometrie technieken welke gebaseerd zijn op de temperatuurafhankelijkheid van de proton resonantie frequentie van water worden over het algemeen beschouwd als ongevoelig voor statische veldinhomogeniteiten omdat er danwel subtractie technieken toegepast worden (PRFS-based MRT), danwel gebruik wordt gemaakt van een interne temperatuuronafhankelijke referentie (mGE-based MRT). In dit hoofdstuk wordt aangetoond dat MR thermometrie technieken wel degelijk beïnvloed worden door statische veld gradiënten, in het bijzonder door gradiënten met dezelfde oriëntatie als de uitleesgradiënt. Zowel theoretisch als experimenteel werd aangetoond dat statische achtergrond gradiënten de effectieve echo tijd veranderen in gradiënt-echo acquisities, hetgeen fouten in de temperatuurmeting met PRFS-based en mGE-based MR thermometrie tot gevolg heeft. De invloed van statische achtergrond gradiënten *in vivo* is bepaald in een vrijwilligsterstudie door het meten van de achtergrond gradiënten in de borst. Conclusie is dat kennis over deze achtergrond gradiënten kan helpen bij het maken van betere keuzes met betrekking tot de sterkte en richting van de uitleesgradiënt van de thermometriesequentie om zo fouten in de temperatuurmetingen te voorkomen.

In **hoofdstuk 8** wordt een potentiële toepassing van de mGE-based MRT techniek onderzocht zoals die beschreven werd in hoofdstuk 6. De hypothese is dat polyethylene glycol signalen (PEG) van gepegyleerde liposomen als temperatuuronafhankelijke referentie kunnen dienen voor absolute MR temperatuur metingen. De mogelijkheid om dynamische absolute MR thermometrie uit te voeren met de multi gradiënt-echo sequentie in combinatie met gepegyleerde liposomen is geëvalueerd. Bij klinisch relevante concentraties bleek de huidige samenstelling van de liposomen in combinatie met de gebruikte MR parameters niet te volstaan voor precieze absolute temperatuurmetingen met mGE-based MR thermometrie. Voor translatie naar *in vivo* toepassingen van MRT met behulp van het PEG signaal zou een verhoogd PEG signaal nodig zijn, wat mogelijk met active targeting of met aanpassingen van de liposomen zodat deze meer PEG bevatten bereikt zou kunnen worden.

CHAPTER 10

DANKWOORD

"If I have seen a little further it is by standing on the shoulders of giants"
Isaac Newton, 1676

De afgelopen jaren heb ik mogen werken aan een onderzoek dat me van begin tot eind na aan het hart heeft gelegen. De ontwikkeling, verdieping en vrijheid die een promotieonderzoek met zich mee brengt is bijzonder en waardevol, en ik voel grote dankbaarheid voor deze ervaring.

Als ik met dit onderzoek al iets verder heb gekeken, dan is dat doordat ik op schouders heb mogen staan. Niet de schouders van een reus of twee, maar die van bijzonder veel mensen gezamenlijk. Van de mensen die me op de mogelijkheid tot promoveren wezen tot de mensen die hun handen uit de mouwen staken tijdens de uitvoer daarvan. Van de mensen die me inhoudelijk veel geleerd hebben tot de mensen die er waren voor de ontspanning. Van Jean Baptiste Joseph Fourier tot de engel op mijn pad tijdens een fietstocht bij Nieuwkuijk. Een grote hoeveelheid schouders, die ik bij deze allemaal heel graag wil bedanken.

Prof. dr. ir. Viergever, promotor, beste Max, in 2001 klopte ik aan bij het Image Sciences Institute voor een klein onderzoek. Meteen was ik gepakt door de combinatie ‘natuurkunde en ziekenhuis’. Dank voor de mogelijkheid om vervolgens ook mijn afstudeer- en promotieonderzoek te doen bij het ISI. Ik heb er al die jaren met veel plezier gewerkt. Dr. ir. Bartels, co-promotor, beste Wilbert, als ik een enquête over promoveren in moet vullen zal mijn ervaring wat betreft ‘betrokkenheid en tijdsinvestering van de begeleider’ de outlier worden. De maandagmiddag afspraak is altijd doorgegaan, je bent altijd

CHAPTER 10

vol aandacht en enthousiasme bij het onderzoek betrokken geweest en je hebt mij met jouw grote kennis van zaken bijzonder veel geleerd. Veel dank daarvoor! Ik vind het prachtig te zien hoe het onderzoek naar en de ontwikkeling van thermische therapie binnen het UMCU de afgelopen jaren gegroeid is. Jouw energie heeft daar enorm aan bijgedragen. Ik wens jou alle goeds.

Dr. Bakker, beste Chris, dank voor je betrokkenheid, ideeën en kennis. Je draagt artikelen aan omdat ze zo'n prachtige beschrijving van de materie bevatten en weet met een scherpe blik altijd de sfeer in en achter teksten te beschrijven. Tot in alle uithoeken van zowel het spatiële als het frequentie domein heb jij MRI benaderd, overdacht en bevraagd. Voor mij was je eeuwige ruimte voor twijfel en andere invalshoeken zeer waardevol.

Geachte leden van de leescommissie, prof. dr. Borel-Rinkes, prof. dr. Mali, prof. dr. Moonen, prof. dr. ir. Lagendijk en prof. dr. Nicolaij, dank voor het beoordelen van mijn manuscript.

Dr. Konings, beste Maurits, jij hebt een unieke kijk op de natuurkunde en haar wetten, ze lijken als muziek in je geest rond te dansen en je hebt ze paraat in elk domein. Brainstorm sessies met jou waren geweldig. Ik ben erg blij met wat onze samenwerking heeft opgeleverd. Veel dank daarvoor!

Dr. Deckers, beste Roel, in Bordeaux heb ik je leren kennen tijdens jouw promotie-onderzoek daar. Het was mooi dat je daarna kwam post-doccen bij het ISI in Utrecht. Het is goed, helder, en gezellig samenwerken met jou. Dank voor je nuchtere blik op de zaken, die hielp mij om af en toe weer even met de voeten op de grond te komen.

Prof. dr. Boelens en Dr. Ippel van de NMR Spectroscopy Research Group van het Bijvoet Center for Biomolecular Research, veel dank voor de samenwerking en de mogelijkheid om experimenten te doen in jullie mooie onderzoeksomgeving. Beste Hans, jij in het bijzonder bedankt voor je inzet, uitleg en tijd. Ik vond het mooi om naast MRI ook de wereld van de NMR beter te leren kennen.

Remmert de Roos, dank voor al je hulp bij het bereiden van alle ethyleenglycol fantomen en je grote interesse in het onderzoek.

Willem van Wolferen en Simon Plomp van de Anatomie, dank voor het verzamelen van de borstweefsel-samples en het meedenken met het onderzoek.

Henk te Biesebeek en Gerrit Wobma van de Instrumentele Dienst, dank voor het bouwen van fantomen en het meedenken bij de ontwerpen ervan. Altijd hadden jullie een creatieve oplossing paraat, ik zal de houten barkruk-zitting-opstelling nooit vergeten.

John Klaessens, dank voor het altijd mogen lenen van de laser-apparatuur.t

Graag bedank ik alle MRI laboranten voor de goede sferen bij de scanners, voor de interesse in dit onderzoek en het openstaan voor al mijn vragen. Heel graag bedank ik ook alle vrijwilligsters en vrijwilligers die aan het (voor)onderzoek van dit proefschrift hebben meegewerk.

Prof. dr. Moonen, beste Chrit, dank voor de gastvrijheid tijdens mijn bezoek aan het IMF in Bordeaux, waar ik naast een hele leuke ook een leerzame tijd heb gehad. Merci également aux gens de Bordeaux d'avoir fait de ma vitise une jolie esperience: Bruno, Mario, Grégory, Baudouin, Philippe, et en particulier merci à Charles Mougenot. Souder ensemble une piscine tandis tu m'expliquais en long en large et en traverse l'ultrason focalisé, inoubliable!

Collega's van het ISI, als je 'het stuk ISI meubilair' wordt genoemd dan is duidelijk dat er in de afgelopen jaren heel veel collega's de revue zijn gepasseerd. Sommigen zijn al lang vertrokken en anderen zijn net binnen. Ik wil jullie hierbij allemaal heel graag bedanken voor deze mooie tijd, voor het kunnen delen van de stress en de geluksmomenten, voor de koffie (en koekjes), voor de inhoudelijke discussies, de prachtige feesten, de goede samenwerking en voor de inspiratie! In het bijzonder wil ik de volgende collega's noemen: Koen, dank voor je energie, je eeuwige vrolijkheid en voor al je software hulp. Peter, dank voor de goede gesprekken, over wat dan ook, al dan niet met een drankje in de hand. Heel veel geluk voor jou! Hendrik, jij hebt altijd de deur openstaan voor een MR fysica-gerelateerde vraag of discussie, dank voor alle keren dat ik daar gebruik van mocht maken. Maartje, lieve kamergenoot, fijn dat ik met jou op de kamer de wereld van het promoveren en de wereld daarbuiten kon bespreken. Ik wens jou alle goeds. Patrik, zonder jou had ik nooit gehoord van de bizarre wereld van Saladfinger en Office space. Jouw Matlab-kennis en je bereidheid om die op elk moment van de dag te delen heeft me enorm geholpen.

Lieve Nicky Peters en Rudolf Burggraaf, lieve paranimfen, ik ben blij en trots dat jullie achter mij staan, en dat ook letterlijk gaan doen op 4 november. Nicky, de geheime Newton, dank voor je steun! Jouw luisterend oor had altijd aan een half woord genoeg en dat was voor mij erg waardevol. Ik bewonder jouw doorzettingsvermogen, je sterke wil. Naarmate ik dichter bij het einde van mijn eigen onderzoek kwam, groeide het besef van wat jij voor elkaar gekregen hebt, en ik ben trots op jou. Alle moois wens ik je toe. Rudolf, lang geleden klopte ik bij je aan om in jouw bedrijf bijles te komen geven, en je leerde me veel over lesgeven. Later stonden we samen aan het roer, en kreeg ik lessen over zaken doen. Nu op het einde van mijn promotie help je me orde uit chaos te scheppen. Ik ben erg blij dat er zo'n bijzondere vriendschap tussen ons gegroeid is.

Dit dankwoord wil ik ook graag gebruiken om te zeggen hoe blij ik ben met alle mooie mensen om mij heen, mijn familie en lieve vrienden. Het is niet te meten hoe belangrijk jullie voor me zijn.

Heel in het bijzonder wil ik hier mijn allerliefste papa en mama en twee zussen Esther en Thirza bedanken, ik ben zo blij dat jullie er zijn. Ook voel ik me gezegend dat ik via jullie zoveel lieve 'bonus' mensen om me heen heb: lieve Geertje en Rob, bonus-broers Maarten en Thomas, bonus-aanhang Stijn en Louis, en mijn allerliefste nichtje Eden! En lieve Bom, jij bedankt voor het printen van de pdf. En dank voor de ontdekking dat sommige vragen beantwoord worden door hun eigen verdwijning.

CHAPTER 10



DANKWOORD



CHAPTER 10

LIST OF PUBLICATIONS

JOURNAL ARTICLES

S.M. Sprinkhuizen, C.J.G. Bakker, L.W. Bartels

“Absolute MR thermometry using time domain analysis of the multi gradient-echo magnitude signal”

Magn Reson Med. 2010 Jul; 64(1):239–48

S.M. Sprinkhuizen, M.K. Konings, M.J. van der Bom, M.A. Viergever, C.J.G. Bakker, L.W. Bartels

“Temperature-induced Tissue Susceptibility Changes lead to Significant PRFS-based MR Temperature Errors during Thermal Interventions in the Human Breast”

Magn Reson Med. 2010 Jul 20. (Epub ahead of print)

S.M. Sprinkhuizen, C.J. Bakker, J.H. Ippel , R. Boelens, M.A. Viergever, L.W. Bartels

“Temperature Dependence of the Magnetic Susceptibility of Human Breast Tissue: an NMR Study”

Submitted for publication

S.M. Sprinkhuizen, C.J.G. Bakker, L.W. Bartels

“Static Field Inhomogeneity as a Source of Errors in PRFS-based and mGE-based MR Thermometry”

In preparation

R. Deckers, **S.M. Sprinkhuizen**, B. Crielaard, H. Ippel, R. Boelens, T. Lammers, C.J.G. Bakker, L.W. Bartels

“Polyethylene glycol (PEG) labeled liposomal drug delivery systems as a source for dynamic absolute MR thermometry”

In preparation

CHAPTER 10

N.H.G.M. Peters, L.W. Bartels, **S.M. Sprinkhuizen**, K.L. Vincken, C.J.G. Bakker
“Do respiration and cardiac motion induce magnetic field fluctuations in the breast and
are there implications for MR thermometry?”
J Magn Reson Imaging. 2009 Mar;29(3):731-5

C. Mougenot, B. Quesson, B.D. de Senneville, P.L. de Oliveira, **S.M. Sprinkhuizen**, J.
Palussière, N. Grenier, C.T. Moonen
“Three dimensional spatial and temporal temperature control with MR-thermometry
guided Focused Ultrasound”
Magn Reson Med. 2009 Mar;61(3):603-14

J. van Prehn, K.L. Vincken, **S.M. Sprinkhuizen**, M.A. Viergever, J.W. van Keulen, J.A.
van Herwaarden, F.L. Moll, L.W. Bartels
“Aortic Pulsatile Distention in Young Healthy Volunteers is Asymmetric: Analysis with
ECG-gated MRI”
Eur J Vasc Endovasc Surg. 2009 Feb;37(2):168-74

CONFERENCE PROCEEDINGS

S.M. Sprinkhuizen, C.J.G. Bakker, J.H. Ippel , R. Boelens and L.W. Bartels
“Measurement of the temperature dependence of susceptibility of human breast fat
tissue”
18th International Society Magnetic Resonance in Medicine, May 2010, Stockholm, Sweden

S.M. Sprinkhuizen, C.J.G. Bakker, and L.W. Bartels
“PRFS-based MR thermometry is hampered by susceptibility changes caused by the
heating of fat: Experimental demonstration”
18th International Society Magnetic Resonance in Medicine, May 2010, Stockholm, Sweden

R. Deckers, **S.M. Sprinkhuizen**, B. Crielaard, H. Ippel, R. Boelens, T. Lammers, C.J.G.
Bakker and L.W. Bartels
“Polyethylene glycol (PEG) labeled liposomal drug delivery systems as a source for
dynamic absolute MR thermometry”
18th International Society Magnetic Resonance in Medicine, May 2010, Stockholm, Sweden

S.M. Sprinkhuizen, C.J.G. Bakker, and L.W. Bartels
“PRFS-based MR thermometry is hampered by susceptibility changes caused by the
heating of fat”
Benelux In Vivo MR Methods Symposium, January 2010, Utrecht, the Netherlands

S.M. Sprinkhuizen, M.K. Konings, C.J.G. Bakker, and L.W. Bartels
“Temperature dependence of the susceptibility of fat leads to significant temperature
errors in PRFS based MR thermometry”
9th International Symposium on Therapeutic Ultrasound, September 2009, Aix-en-Provence, France

LIST OF PUBLICATIONS

S.M. Sprinkhuizen, H.A. Tromp, C.J.G. Bakker, J.D. Workum, H. de Leeuw, M.A. Viergever, and L.W. Bartels

“A novel application for MR Thermometry: Post Mortem Interval estimation in forensic medicine”

17th International Society Magnetic Resonance in Medicine, May 2009, Honolulu, USA

S.M. Sprinkhuizen, M.K. Konings, C.J.G. Bakker, and L.W. Bartels

“Heating of fat leads to significant temperature errors in PRFS based MR thermometry”

17th International Society Magnetic Resonance in Medicine, May 2009, Honolulu, USA

S.M. Sprinkhuizen, C.J.G. Bakker, L.W. Bartels

“The influence of background gradients in multi gradient-echo MR thermometry”

17th International Society Magnetic Resonance in Medicine, May 2009, Honolulu, USA

S.M. Sprinkhuizen, C.J.G. Bakker, L.W. Bartels

“The influence of background gradients in multi gradient-echo MR thermometry”

Benelux In Vivo MR Methods Symposium, December 2008, Antwerpen, Belgium

S.M. Sprinkhuizen, C.J.G. Bakker, L.W. Bartels

“Absolute MR thermometry using time domain analysis of the multi gradient-echo modulus signal”

16th International Society Magnetic Resonance in Medicine, May 2008, Toronto, Canada

S.M. Sprinkhuizen, C.J.G. Bakker, L.W. Bartels

“Absolute MR thermometry using time domain analysis of the multi gradient-echo modulus signal”

10th International Congress On Hyperthermic Oncology, April 2008, Munich, Germany

S.M. Sprinkhuizen, N.H.G.M. Peters, K.L. Vincken, C.J.G. Bakker, L.W. Bartels

“Development of reliable Magnetic Resonance thermometry for real-time feedback control of thermal therapy”

Benelux In Vivo MR Methods Symposium, December 2007, Nijmegen, the Netherlands

S.M. Sprinkhuizen, N.H.G.M. Peters, K.L. Vincken, C.J.G. Bakker, L.W. Bartels

“Quantification and correction of motion-induced field disturbances for accurate PRFS-based MR thermometry”

6th Interventional MRI Symposium, September 2006, Leipzig, Germany

INVITED PRESENTATIONS

“MR-guided high-intensity focused ultrasound: Tumoren te lijf met geluid”

NVMBR Congress, May 2010, Maastricht, the Netherlands

CHAPTER 10

“MR-guided high-intensity focused ultrasound”
NVMBR Congress, May 2009, Rotterdam, the Netherlands

Lectures on medical image formation
April 2006, Christelijk Gymnasium Utrecht, the Netherlands
March 2009, Gemeentelijk Gymnasium Hilversum, the Netherlands

“Absolute MR thermometry”
Werkgroep Klinische Hyperthermie, Department of Radiotherapy, AMC Amsterdam, December 2008, Amsterdam, the Netherlands

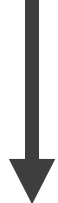
PRIZES

Young Investigator Award
10th International Congress On Hyperthermic Oncology, April 2008, Munich, Germany

LIST OF PUBLICATIONS

CHAPTER 10

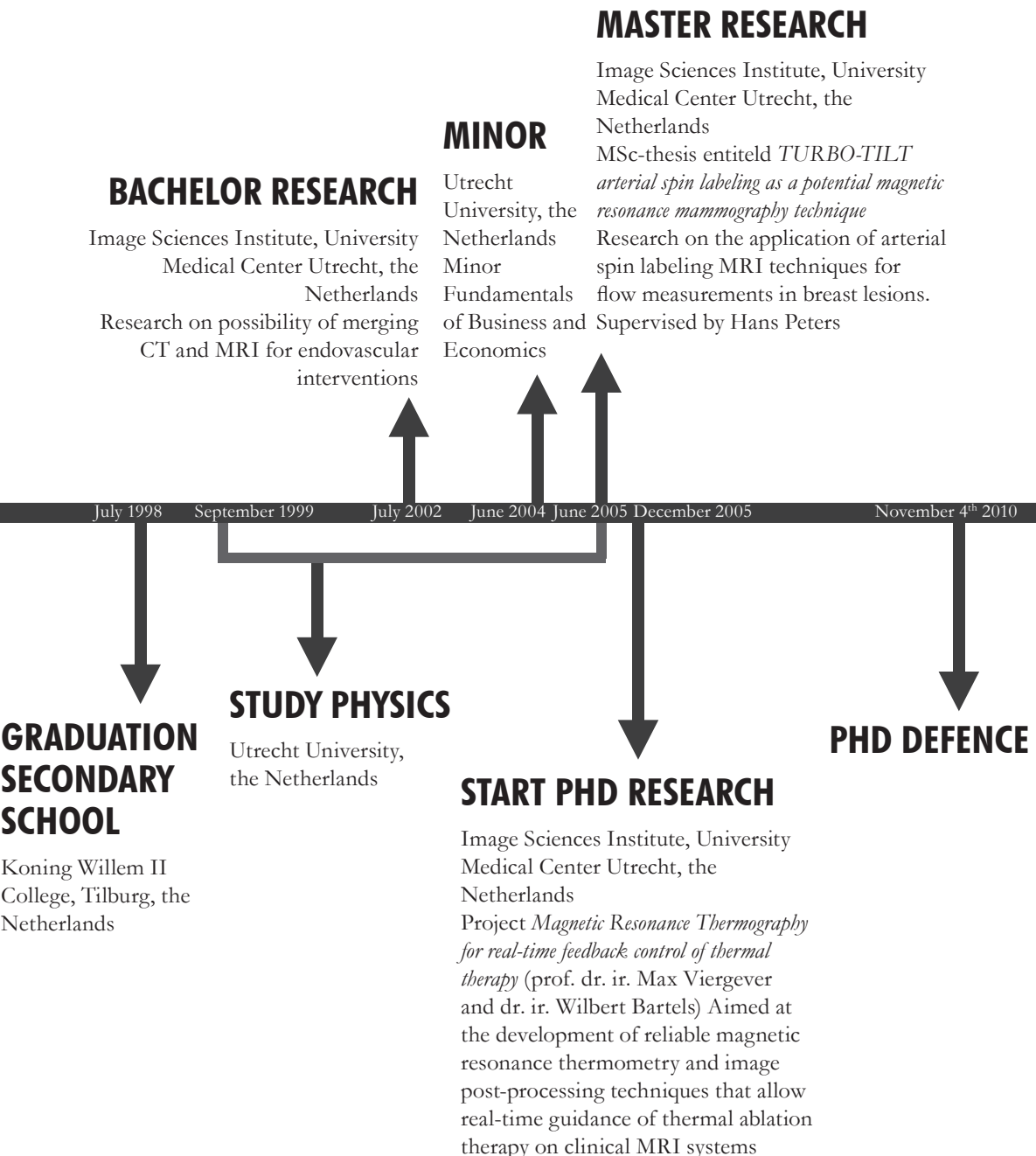
August 16th 1980



BORN

Goirle, the Netherlands

CURRICULUM VITAE



THE PURPOSE OF A FISH TRAP
IS TO CATCH FISH,
AND WHEN THE FISH ARE CAUGHT,
THE TRAP IS FORGOTTEN.

THE PURPOSE OF WORDS
IS TO CONVEY IDEAS.
WHEN THE IDEAS ARE GRASPED
THE WORDS ARE FORGOTTEN.

WHERE CAN I FIND A MAN
WHO HAS FORGOTTEN WORDS?
HE IS THE ONE
I WOULD LIKE TO TALK TO.

Chuang Tzu
From 'The Empty Boat' by Bhagwan Shree Rajneesh